

π^0 -mesons and photons measured
in Au+Au collisions
at an energy of $\sqrt{s_{\text{NN}}} = 62 \text{ GeV}$

Dissertation
zur Erlangung des Doktorgrades
der Naturwissenschaften

vorgelegt beim Fachbereich Physik
der Johan-Wolfgang-Goethe-Universität
in Frankfurt am Main

von
Alexander Albert Wetzler
aus Frankfurt am Main

Frankfurt, 2006
D 30

Vom Fachbereich Physik der Johann Wolfgang Goethe-Universität als Dissertation angenommen.

Dekan:	Prof. Dr. Wolf Aßmus
Gutachter:	Prof. Dr. Herbert Ströbele
	Prof. Dr. Dr. h.c. Reinhard Stock

Datum der Disputation:

Zusammenfassung

In dieser Arbeit wurden Photonen und π^0 -Mesonen in Gold-Gold-Kernkollisionen bei einer Schwerpunktenenergie von $\sqrt{s_{NN}} = 62 \text{ GeV}$ mit dem STAR-Experiment am RHIC gemessen.

Kapitel 1 gibt dabei eine Einleitung in die Theorie der starken Wechselwirkung, in das Verständnis von relativistischen Schwerionenkollisionen und von den dabei erzeugten Photonen: Im Standardmodell der Teilchenphysik wirkt die starke Wechselwirkung zwischen den elementaren Bauteilen der Kernmaterie, den Quarks. Die Feldquanten der Wechselwirkung heißen Gluonen. Die Quantenfeldtheorie, die diese Wechselwirkung beschreibt, ist die Quantenchromodynamik (QCD). Im Gegensatz zur Quantenelektrodynamik gibt es in der QCD drei Farbladungen statt einer einzigen elektrischen. Außerdem tragen die Wechselwirkungsteilchen Ladung und wechselwirken daher auch miteinander. Die Stärke der Kopplung variiert stark mit der Distanz und dem Impulsübertrag. Bei kleinen Distanzen und großen Impulsüberträgen ist die Kopplung schwach und die Wechselwirkung kann störungstheoretisch berechnet werden. In diesem Fall spricht man auch vom *asymptotic freedom*. Bei großen Distanzen und kleinen Impulsüberträgen ist die Kopplung stark. Da die Kraft zwischen stark wechselwirkenden Teilchen bei einer Vergrößerung der Entfernung konstant ist, steigt die Energie immer weiter an und es ist unmöglich, ein Quark oder Gluon im Vakuum zu isolieren. Sie sind daher in farbneutrale Zustände, Hadronen, eingeschlossen (*confinement*).

Die starke Kopplung bei großen Distanzen und kleinen Impulsüberträgen hat zur Folge, dass stark wechselwirkende Systeme nur unter sehr eingeschränkten Bedingungen berechnet werden können. Berechnungen mit der Gittereichtheorie deuten in einem System bei hohen Temperaturen und kleinen Baryonenzahldichten auf einen Phasenübergang von hadronischer Materie zu einem System hin, in dem Quarks und Gluonen in größeren Volumina als denen von Hadronen frei beweglich sind. Der Einschluss in Hadronen ist in einem solchen Quark-Gluon-Plasma (QGP) aufgehoben.

Im Labor ist stark wechselwirkende Materie nur in Form von Kernmaterie verfügbar. Bei Schwerionenkollisionen werden Kerne mit hohen Energieen aufeinandergeschossen. Weil dabei die Kernmaterie stark komprimiert und erhitzt wird, werden Schwerionenkollisionen genutzt, um stark wechselwirkende Materie unter diesen extremen Bedingungen zu studieren. Weil sie nur ein begrenztes Volumen haben und aufgrund des hohen Druckes explosionsartig expandieren, ist die erzeugte Materie nur sehr kurzlebig. Daher ist eine ganze Reihe von Observablen notwendig um die gesamte Entwicklung des Systems zu studieren und Schlüsse dahingehend zu ziehen, ob tatsächlich ein QGP erzeugt wurde oder aber auch nicht.

Eine dieser Observablen sind die Spektren von Photonen. Im Gegensatz zu den meisten erzeugten Teilchen in einer Schwerionenkollision sind sie nicht stark wechselwirkend und durchdringen die erzeugte Materie mit einer sehr kleinen Wechselwirkungswahr-

scheinlichkeit. Daher können ihre Spektren Informationen über den gesamten Verlauf der Kollision liefern und nicht nur über den Endzustand, in dem alle Teilchen vom System entkoppelt sind. Theoretische Modellrechnungen sagen voraus, dass sowohl in hadronischer Materie als auch in einem QGP ein Spektrum von thermischen Photonen emittiert wird, das auf die Temperatur des Systems schließen lässt.

Die Schwierigkeit der Analyse besteht darin, dass es bei Schwerionenkollisionen neben der thermischen Produktion noch eine Reihe anderer Mechanismen gibt, die Photonen produzieren. So können im frühen Stadium der Kollision Quarks und Gluonen mit hohen Impulsüberträgen streuen und dabei sehr hochenergetische, harte, Photonen von mehreren GeV erzeugen. Auch die erzeugten harten Quarks mit hohen Impulsen können beim Durchqueren des erzeugten Mediums streuen und dabei Photonen erzeugen. Theoretische Modellrechnungen sagen voraus, dass die Photonenproduktion aus harten Streuprozessen bei RHIC-Energien und Transversalimpulsen über $3 \text{ GeV}/c$ die thermische Produktion übersteigt. Diese Photonen nennt man, ebenso wie die thermischen, direkte Photonen, da sie innerhalb des Mediums erzeugt werden.

Der größte Teil der Photonen unter der Schwelle von $3 \text{ GeV}/c$ entstammt aber dem elektromagnetischen Zerfall von Hadronen im Endzustand der Schwerionenkollision. Den größten Anteil hat dabei das π^0 -, gefolgt vom η -Meson. Aufgrund ihrer kurzen Lebensdauer zerfallen diese Mesonen in unmittelbarer Nähe des Interaktionspunktes. Daher ist es mit STAR nicht möglich, direkt zu messen, ob ein Photon von einem dieser Zerfälle stammt. Der Beitrag zum Photonenspektrum lässt sich theoretisch einfach bestimmen, wenn die Spektren dieser Mutterteilchen bekannt sind und dann die daraus resultierenden Photonenspektren berechnet. Die experimentelle Schwierigkeit besteht dabei darin, dass die Messung auf wenige Prozent genau sein muss, da die Zerfallsphotonen im relevanten Bereich etwa 90% aller erzeugten Photonen ausmachen.

Das STAR-Experiment stellt verschiedene Detektoren zur Verfügung, um Photonen und π^0 -Mesonen zu messen. Die primären Detektoren dafür sind die elektromagnetischen Kalorimeter. Die in dieser Arbeit beschriebene Analyse nutzt aber die Spurendriftkammer (TPC). Da Photonen nicht elektrisch geladen sind und die Driftkammer nur für geladene Teilchen empfindlich ist, wird eine vorherige Konversion des Photons in ein Elektron-Positron-Paar notwendig. Dies passiert innerhalb des elektromagnetischen Feldes der Atomkerne oder der Hüllenelektronen des Detektormaterials im experimentellen Aufbau von STAR. Die resultierenden Elektron- und Positronspuren werden in der Spurendriftkammer gemessen.

Kapitel 2 gibt eine Übersicht über den RHIC Beschleunigerkomplex und die Experimente. Der größte Teil des Kapitels beschäftigt sich mit dem Aufbau von STAR. Da für diese Analyse die Driftkammer genutzt wird, um Konversionselektronen zu messen, wird bei der Beschreibung des experimentellen Aufbaus von STAR besonders auf das Detektormaterial zwischen dem Strahlrohr und der TPC eingegangen.

Kapitel 3 erklärt, wie Photonen und π^0 -Mesonen für diese Arbeit gemessen wurden: Aus allen gemessenen Spuren werden Elektron- und Positronkandidaten anhand des gemessenen spezifischen Energieverlustes ausgewählt. Da die Spuren ihren Ursprung am Ort der Konversion haben und im Allgemeinen nicht zum Hauptvertex der Interaktion zurücklaufen, werden Paare von Spuren ausgewählt, die einen gemeinsamen Vertex haben, der nicht mit dem Hauptvertex übereinstimmt. Weil ein Photon keine Ruhemasse hat, wird bei der Selektion gefordert, dass der Öffnungswinkel der beiden Spuren und die invariante Masse des Paares klein ist. Da direkte Photonen aus dem Hauptvertex kommen und auch Zerfallsphotonen wegen der begrenzten Detektorauflösung von dort zu kommen scheinen, ist das nächste Auswahlkriterium, dass der Impulsvektor des rekonstruierten Photonkandidaten vom Konversionsvertex zum Hauptvertex zurückzeigen muss.

Die rohen Spektren von π^0 -Mesonen wurden gemessen, indem für Paare von gemessenen Photonen in einem Ereignis die invariante Masse berechnet wird. Deren Verteilung hat ein lokales Maximum bei der Masse des π^0 -Mesons. Da der kombinatorische Untergrund größer ist als das Signal, wird die Zahl der Mesonen bestimmt, indem der Verlauf des Spektrums im Bereich des Maximum mit einer Gaußfunktion plus einem Polynom für den Untergrund angenähert wird. Alternativ wird das Signal nicht mit einer Gaußfunktion, sondern mit einer Verteilung, deren Form mit Monte-Carlo-Simulationsmethode ermittelt wurde, angenähert. Bei einer dritten Methode werden der kombinatorische Untergrund abgezogen und die verbleibenden Einträge im Signal gezählt. Die verschiedenen Methoden weisen im Mittel Unterschiede von bis zu 10% auf. Dies ist ein Beitrag zum systematischen Fehler der π^0 -Spektren.

In Kapitel 4 wird erklärt, wie die Effizienz der Photonen- und π^0 -Messung bestimmt und wie die Spektren für diese Effizienz korrigiert werden. Ersteres geschieht mit Hilfe einer Monte-Carlo-Methode. Dazu werden π^0 -Mesonen mit ihren Zerfällen und Photonen simuliert. Als Ursprungsort dieser Teilchen wurde der Hauptvertex einer echten Schwerionenkollision genommen. Die Trajektorie der Photonen durch das Experiment wurde berechnet und Konversionen längs der Trajektorie in dem Detektormaterial simuliert. Danach werden die Trajektorien der erzeugten Elektronen und Positronen berechnet. Im zweiten Schritt werden das von den Elektronen und Positronen in der Driftkammer ionisierte Gas, die Drift der Ladungen und das auf den Ausleseflächen erzeugte Signal simuliert. Realistische Umfeldbedingungen für die Rekonstruktion dieser Elektronen-Positronen-Paare werden geschaffen, indem die so erzeugten Detektorsignale in die aufgezeichneten Signale von wirklichen Stoßereignissen eingebettet werden. Die so mit simulierten Konversionen angereicherten Ereignisse werden nun rekonstruiert. Dabei wird festgestellt, welche Monte-Carlo-Spuren zu welchen rekonstruierten Spuren gehören. Am Ende wird untersucht, ob die beiden rekonstruierten Spuren, die zu den simulierten Spuren gehören, einen Photonkandidaten erzeugen, der alle Auswahlkriterien erfüllt. Mit dieser ganzen Monte-Carlo-Prozedur werden die Konversionswahrscheinlichkeit und die Rekonstruktionseffizienz für Photonen und π^0 -Mesonen bestimmt. Das Produkt der beiden ist die Nachweiswahrscheinlichkeit der in Kapitel 3 beschriebenen Methode zur

Messung von Photonen oder π^0 -Mesonen.

Der größte Unsicherheitsfaktor dieser Prozedur ist die Beschreibung der Detektorgeometrie, die zur Bestimmung der Konversionswahrscheinlichkeit in den einzelnen von den Photonen durchquerten Detektorbereichen benutzt werden. Dabei ist besonders die Beschreibung des Silicon Vertex Trackers (SVT) und des Silicon Strip Detectors (SSD), den Detektoren zwischen dem Strahlrohr und der TPC, wichtig, da ein großer Teil der Konversionen in diesen beiden Detektoren statt findet und beide eine komplizierte Struktur besitzen und daher die Genauigkeit ihrer Beschreibung fraglich ist. Da diese Beschreibung für das Gas in der Driftkammer wegen der einfachen Geometrie am verlässlichsten ist, wurden die Konversionen in diesem Volumen zur Normierung der Anzahl der Konversionen in den anderen Detektorvolumina genutzt. Diese Methode zeigte, dass in dem SVT und dem SSD etwa ein Drittel des Materials in der Geometriebeschreibung fehlt. Die Berechnung der Effizienz wurde dann dementsprechend für Konversionen in den Volumen dieser Detektoren korrigiert. Die Unsicherheit dieser Korrektur wurde untersucht, indem die Zahl der Konversionen nach der Korrektur und Normalisierung im TPC-Gas für verschiedener Phasenraumbereiche und Kollisionszentralitäten verglichen wurde. Daraus wurde ein systematischer Fehler der Photonenspektren von 10% und der π^0 -Spektren von 20% bestimmt.

Die weiteren Unsicherheiten in der Methode zur Effizienzbestimmung wurden untersucht durch Variation der verschiedenen Auswahlkriterien. Für jede Variation wurde eine Analyse der echten Daten durchgeführt und die entsprechenden Effizienzen aus den simulierten Daten bestimmt. Die Verhältnisse der Transversalimpulsspektren unter 4 GeV/c mit variierten zu den mit normalen Selektionskriterien wurden gemittelt. Die dadurch bestimmten systematischen Fehler belaufen sich auf 5% für die Photonenspektren und 10% für die π^0 -Spektren.

In Kapitel 5 werden die eigentlichen Resultate der Analyse vorgestellt. Der Datensatz, auf dem die Analyse basiert, besteht aus Gold-Gold-Kollisionen bei einer Schwerpunktsenergie von $\sqrt{s_{NN}} = 62$ GeV. Die Selektionskriterien der einzelnen Ereignisse bei der Datennahme und der Analyse werden erklärt. Der Datensatz wird in vier verschiedene Zentralitäten eingeteilt. Das erste Resultat sind die Transversalimpuls- und Rapiditätsspektren von inklusiven Photonen für alle vier Zentralitäten sowie den gesamten Datensatz. Von π^0 -Mesonen werden Transversalimpulsspektren für die vier Zentralitäten und den gesamten Datensatz gezeigt. Die Resultate für π^0 -Mesonen werden mit Resultaten der PHENIX Kollaboration bei der gleichen Energie verglichen und stimmen innerhalb der systematischen Fehler mit diesen überein. Ein zweiter Vergleich findet mit STAR Resultaten auf Basis der gleichen Methode, die in dieser Arbeit erklärt wird, aber bei einer Kollisionsenergie von $\sqrt{s_{NN}} = 130$ GeV statt. Dieser Vergleich zeigt, dass die Spektren wie erwartet bei der höheren Energie härter sind. Weiterhin werden die π^0 -Spektren aus dieser Arbeit mit den von STAR im gleichen Datensatz mit der TPC und dem Flugzeitdetektor (ToF) gemessenen Mittel der π^+ - π^- -Spektren verglichen. Dieser Vergleich der Transversalimpulsspektren zeigt keine Abweichungen, die größer sind als die

systematischen Fehler. Die $\pi^+\pi^-$ -Spektren wurden an Stelle der π^0 -Spektren benutzt, um durch eine Simulation die Spektren der Zerfallsphotonen zu bestimmen und die Zentralitätsabhängigkeit dieser Photonenspektren mit derjenigen der gemessenen Photonenspektren zu vergleichen. Dazu wurden die Verhältnisse der Spektren in zentralen mit denjenigen in peripheren Kollisionen verglichen, was den Vorteil hat, dass sich durch die Verhältnisse die meisten systematischen Fehler neutralisieren. Der Vergleich zeigt, dass die Zentralitätsabhängigkeit der gemessenen Photonenspektren mit derjenigen der simulierten bis 4 GeV/c Transversalimpuls gut übereinstimmt.

Um die Spektren der direkten Photonen zu erhalten, müssen von den Spektren der inklusiven Photonen die Spektren der Zerfallsphotonen abgezogen werden. Letztere müssen berechnet werden. Die naheliegendste Methode wäre in diesem Fall, dazu die in dieser Arbeit gemessenen π^0 -Spektren heranzuziehen. Deren statistische Fehler sind sehr viel größer als die der $\pi^+\pi^-$ -Spektren, deren mittel mit den π^0 -Spektren äquivalent ist. Aufgrund der kleineren statistischen Fehler erlauben sie sehr viel kleinere Unsicherheiten einer Annäherung durch eine Funktion. Für die zweite wichtige Quelle von Zerfallsphotonen, die η -Mesonen, wurde eine m_t -skalierte Version der $\pi^+\pi^-$ -Spektren genutzt. Die aus diesen $\pi^+\pi^-$ - und η -Spektren resultierenden Photonen wurden simuliert. Das Verhältnis der inklusiven Photonenspektren zu den so ermittelten Zerfallsphotonenspektren liegt im Bereich von 1 bis 3 GeV/c Transversalimpuls bei 1.1 bis 1.2. Da dieser Wert unter Berücksichtigung aller systematischen Fehler der Photonenspektren und $\pi^+\pi^-$ -Spektren konsistent mit 1 ist, ist eine Bestimmung des Anteils direkter Photonen nicht möglich.

In Kapitel 6 wird neben der Zusammenfassung der Ergebnisse diskutiert, was für die Messung direkter Photonen mit STAR im Bereich von 1 bis 3 GeV/c Transversalimpuls notwendig ist. Der größte einzelne Unsicherheitsfaktor bei dieser Analyse ist die Unsicherheit in der Geometriebeschreibung der Detektoren zwischen dem Strahlrohr und der Driftkammer. Ein weiterer Unsicherheitsfaktor sind die großen statistischen Fehler der π^0 -Spektren.

Eine Möglichkeit für eine zukünftige Datennahmeperiode besteht darin, zum experimentellen Aufbau von STAR einen speziellen Photonenkonverter hinzuzufügen. Ein solcher Konverter würde das Problem mit der Geometriebeschreibung lösen, wenn er aus einem massiven Stück schweren Metalls gefertigt wäre, da eine solche Geometrie sehr einfach zu beschreiben ist. Wenn ein solcher Konverter eine Strahlungslänge von 10% hätte, würde er eine ähnliche Zahl von Konversionen erzeugen wie der SVT und SSD zusammen. Platziert nahe am inneren Feldkäfig der TPC würde sich die Akzeptanz zu niedrigeren Transversalimpulsen erstrecken als für Konversionen in den beiden Detektoren. Auch ein dickerer Konverter wäre möglich, würde aber wohl einen exklusiven Zeitraum zur Datennahme für Konversionsphotonen benötigen, da die Vielfachstreuung von allen Teilchen in einem solchen Konverter für andere Analysen sehr störend wäre.

Den zentrale Punkt dieser Dissertation bildet neben der Messung von Photonenspektren und π^0 -Spektren in Gold-Gold-Kollisionen bei einer Energie von $\sqrt{s_{NN}} = 62$ GeV insbe-

sondere die detaillierte Analyse der systematischen Fehler dieser Messungen und deren Auswirkungen auf eine mögliche Messung von direkten Photonen in der Zukunft.

Contents

1	Introduction	11
1.1	The strong interaction	12
1.2	Heavy Ion Collisions	15
1.2.1	Experimental parameters	16
1.2.2	Heavy ion accelerator facilities	17
1.2.3	Observables	18
1.3	Photons in Heavy Ion Collisions	19
1.3.1	Jets and Photons	20
1.3.2	Medium production of Photons	22
1.3.3	The composition of direct photon spectra	24
1.3.4	Decay Photons	25
1.4	Direct photon measurements	26
1.4.1	WA98	26
1.4.2	PHENIX	27
1.4.3	Future measurements at LHC	31
1.5	Photon measurement at STAR	31
2	The STAR experimental setup	33
2.1	Accelerators	34
2.2	STAR	35
2.2.1	The STAR coordinate system	36
2.2.2	Magnet	37
2.2.3	Inner parts of the experimental setup	38
2.2.4	Time Projection Chamber	39
2.2.5	Trigger System	41
2.2.6	Outer detectors	42
3	Detecting photons and π^0-mesons	45
3.1	Photon interaction processes in matter	46
3.2	Photon conversions	47
3.2.1	Radiation Length	47
3.3	Photon measurement techniques	49
3.4	Reconstruction of photon conversions	50
3.4.1	The STAR track model	50
3.4.2	Selection of e^+ - and e^- -track candidates	51

3.4.3	Selection of photon conversions	52
3.4.4	Treatment of the combinatorial background	56
3.4.5	Overall effect of the cuts on signal and background	58
3.5	Reconstruction of the π^0 -meson yield	59
4	Efficiency and acceptance correction	67
4.1	The photon- and π^0 -embedding process	68
4.1.1	Number and distribution of embedded particles	70
4.2	Missing material in the geometry description in simulations	70
4.3	Photon matching efficiency	73
4.4	Momentum resolution and energy loss correction	75
4.5	dE/dx cut correction	76
4.6	Estimate of systematic uncertainties	77
4.6.1	Uncertainty in the geometry correction	77
4.6.2	Other uncertainties in the embedding procedure	78
5	Results	81
5.1	Data set	82
5.2	Inclusive photons	83
5.2.1	Photon detection efficiency	83
5.2.2	Inclusive photon spectra	84
5.3	π^0 -mesons	87
5.3.1	π^0 detection efficiency	87
5.3.2	π^0 -spectra	88
5.4	Comparison to other measurements	90
5.4.1	π^0 -mesons from PHENIX at $\sqrt{s_{NN}} = 62$ GeV	90
5.4.2	π^0 -mesons from the STAR TPC at $\sqrt{s_{NN}} = 130$ GeV	91
5.4.3	$\pi^+\pi^-$ -spectra from STAR at $\sqrt{s_{NN}} = 62$ GeV	91
5.4.4	Comparison of photons to $\pi^+\pi^-$ -spectra from STAR	94
5.5	Photons from electro-magnetic hadron decays	96
5.5.1	Direct photons	97
5.6	Summary of all systematic uncertainties	99
6	Conclusion	101
6.1	Inclusive photons and π^0 -mesons	102
6.2	Direct photons	102
6.3	Outlook	103

1 Introduction

1.1 The strong interaction

Hadrons are all measured particles, which are subject to the strong interaction. In the standard model of particle physics hadrons consist of strongly interacting quarks. The theory describing the strong interaction is Quantum Chromo Dynamics or QCD, a non-abelian gauge theory. The Lagrangian density of QCD is

$$\mathcal{L} = \sum_{i=1}^{n_f} \bar{\psi}_i \gamma_\mu (i\partial^\mu - gA_a^\mu \frac{\lambda_a}{2}) \psi_i - \sum_{i=1}^{n_f} m_i \bar{\psi}_i \psi_i - \frac{1}{4} \sum_a F_a^{\mu\nu} F_{a,\mu\nu} \quad (1.1)$$

A_a are the gluon and ψ_i the quark fields, λ_a the Gell-Mann-Matrices and $F_a^{\mu\nu} = \partial^\mu A_a^\nu - \partial^\nu A_a^\mu + igf_{abc}A_b^\mu A_c^\nu$ the gluon field strength tensor. QCD is often compared to Quantum Electro Dynamics, QED, which is the theory describing the electro-magnetic interaction. Compared to QED the QCD Lagrangian is different by having the Gell-Mann-Matrices (λ_a) and the third term in the gluon field strength tensor ($igf_{abc}A_b^\mu A_c^\nu$). This corresponds to self-interacting field quanta with $SU(3)$ as the underlying symmetry, which is much more complex than $U(1)$ in QED. In QED electrically charged particles interact with each other by exchanging electro-magnetic field quanta called photons. In contrast in QCD there is not just one charge but three color charges. Each color has two states analogous to the positive and negative electric charges. They are commonly referred to as color and anti-color. Quarks carry one of the three colors, while anti-quarks carry one of the anti-colors. The field quanta exchanged between colored particles are gluons, which in contrast to the photons also carry color themselves and therefore are self-interacting. Their color states are non-neutral mixtures of colors and anti-colors.

The strength of the coupling in QCD varies strongly with the distance between the colored objects or with the magnitude of the momentum transfer. For small distances and large momentum transfers, the coupling is weak, which corresponds to a property referred to as asymptotic freedom. Due to this weak coupling it is possible to calculate interactions with a large momentum transfer perturbatively. At large distances and small momentum transfers, the coupling is strong. Because the force between colored objects stays constant when increasing the distance, an infinite amount of energy would be necessary to separate two colored objects, which are in a color-neutral state. Therefore all colored objects are confined into color-neutral states. This property is commonly called confinement.

In the strong coupling regime all higher order processes involving more than one gluon contribute with the same magnitude as the single gluon exchange. Therefore it is impossible to calculate perturbatively interactions in the strong coupling regime. One solution to this calculational difficulty is the lattice gauge theory, which uses a discrete space-time lattice. However on the lattice the calculations are limited to systems in thermodynamic equilibrium and with baryon densities much lower than in nuclear matter.

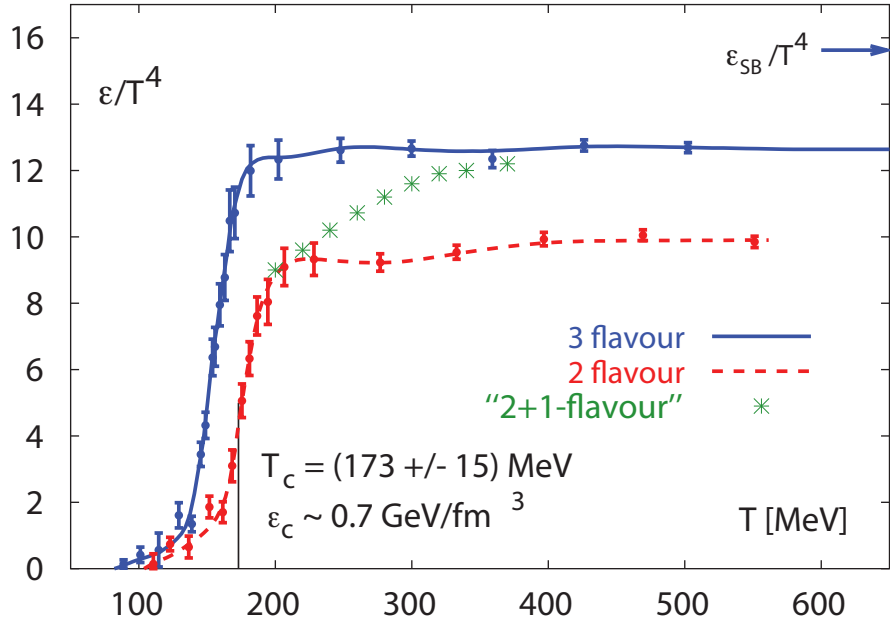


Figure 1.1: In QCD calculations on the lattice a phase transition is observed. The two different curves are for 2 and 3 light quark flavors, while the stars are an estimate for realistic quark masses [KLP⁺]. They show the energy density (ϵ) divided by temperature (T) to the 4th power versus the temperature. ϵ_{SB}/T^4 is the Stephan-Boltzmann-Limit for an ideal gas.

For such systems in equilibrium the relation of the energy density to the temperature has been calculated on the lattice. As shown in figure 1.1 it exhibits a phase transition from a hadronic gas to a phase, where the confinement of quarks and gluons into hadrons is broken. In this quark-gluon-plasma (QGP) quarks and gluons are the relevant degrees of freedom. The phase transition is expected to be at a temperature of about 170 MeV and at an energy density on the order of 1 GeV/fm³.

A schematic phase diagram of strongly interacting matter is shown in figure 1.2: It shows the relation of the temperature to the baryo-chemical potential μ_B of a system. Normal nuclear matter sits at $\mu_B = 1$ and at low temperature. For high temperatures or baryon number densities much higher a phase transition from hadronic matter to a quark-gluon-plasma is expected [CP75]. This phase transition has been studied for low μ_B using lattice gauge theory and was found to be a rapid cross over up to a critical point, where it changes to a first order phase transition [FK02]. For low temperatures and very high baryon densities more exotic phases like color superconductors are predicted to exist [ARW98].

In the early universe a few tens of microseconds after the Big Bang, the universe was expanding and cooling down rapidly. At that time the energy density was still much

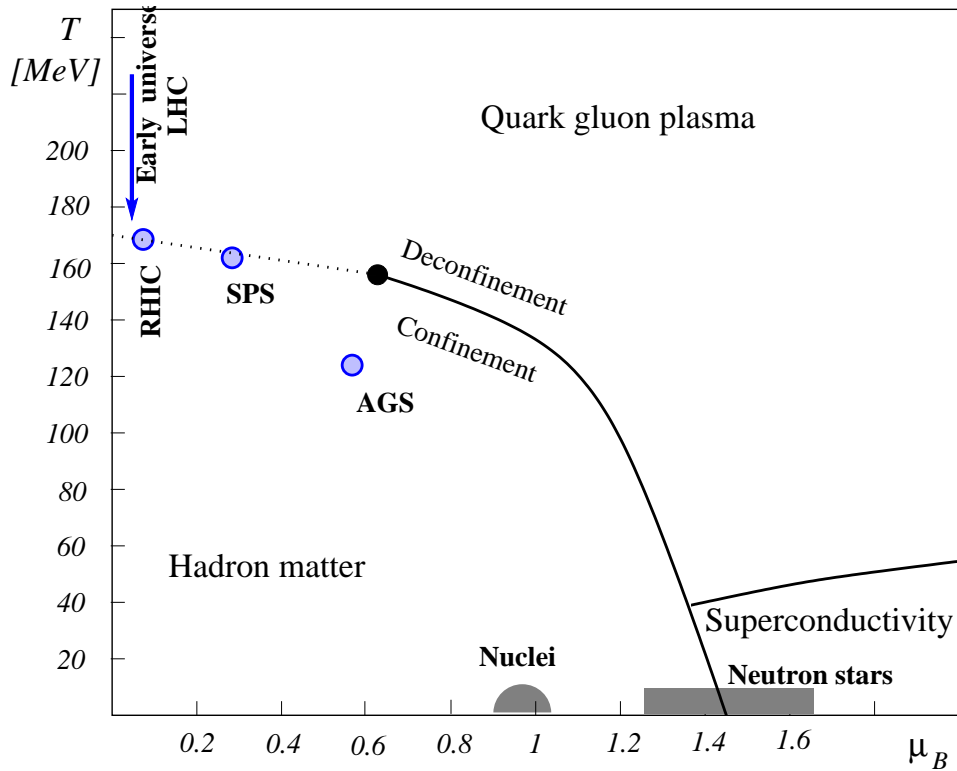


Figure 1.2: Schematic phase diagram of QCD [FM04].

higher than $1\text{GeV}/\text{fm}^3$ and thus the predominant form of matter could not have been hadronic but rather a quark-gluon-plasma. The trajectory the matter in the universe was going through at that stage is indicated by the arrow in the top left corner of the phase diagram. Nowadays a quark-gluon-plasma might still be found at the core of compact astronomic objects like neutron stars, where the baryon density is very high and the temperature very low. This is indicated in the lower right corner of the phase diagram.

The circles in the diagram labeled RHIC, SPS and AGS are three examples for freeze out points, which were derived from measurements in heavy ion collisions. They are discussed in more detail in the next section.

The theoretical treatment with lattice gauge theory is so far only possible in the high temperature region and reaching up in baryon density to the region, where the critical point is expected to sit, which marks the transition from a cross over to a first order phase transition.

1.2 Heavy Ion Collisions

In the laboratory strongly interacting matter is available in the form of atomic nuclei. These consist of protons and neutrons, which are baryons. Baryons are hadrons that are composed of three strongly interacting quarks. To increase the energy in such nuclear matter, two nuclei can be accelerated and collided. To create a quark-gluon-plasma quarks and gluons have to be deconfined from the volume of a single hadron. Therefore the only way to access strongly interacting matter at the volumes and energy densities necessary to create a quark-gluon-plasma in the laboratory is by colliding heavy ions at very high energy. However, even if high energy density matter is produced in heavy ion collisions, the produced system is of finite size, lives very shortly and expands rapidly.

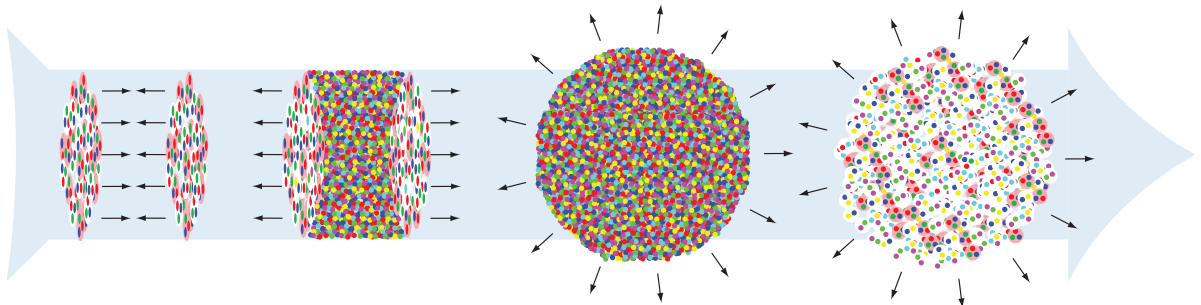


Figure 1.3: Schematic display of a heavy ion collision at ultra-relativistic energies. Shown are the different stages of the approaching nuclei, the interpenetration and creation of new matter, the expansion of a quark-gluon-plasma and the expansion of hadronic matter.

The evolution of heavy ion collisions at ultra-relativistic energies is illustrated in figures 1.3 and 1.4: In the initial state particles from the two nuclei have very high relative longitudinal momenta along the beam direction. By subsequent collisions with particles from the other nucleus the longitudinal momenta are partially or completely converted into transverse momenta and production of new particles. These are produced mostly with low center of mass momenta in the area, where both nuclei interacted. Particles in this densely populated interaction zone subsequently experience enough interactions to reach thermal and chemical equilibrium. It is then justified to describe the system with thermodynamic parameters, which define the coordinates of the created matter in the QCD phase diagram.

Depending on the collision energy the system may equilibrate into a hadronic matter or a quark-gluon-plasma. In both cases the very high energy density in the interaction zone and the low energy density in the vacuum surrounding it result in a rapid expansion of the system. During the expansion the system will cool down and cross various transitions: If a quark-gluon-plasma was formed, the first transition will be to hadronic matter,

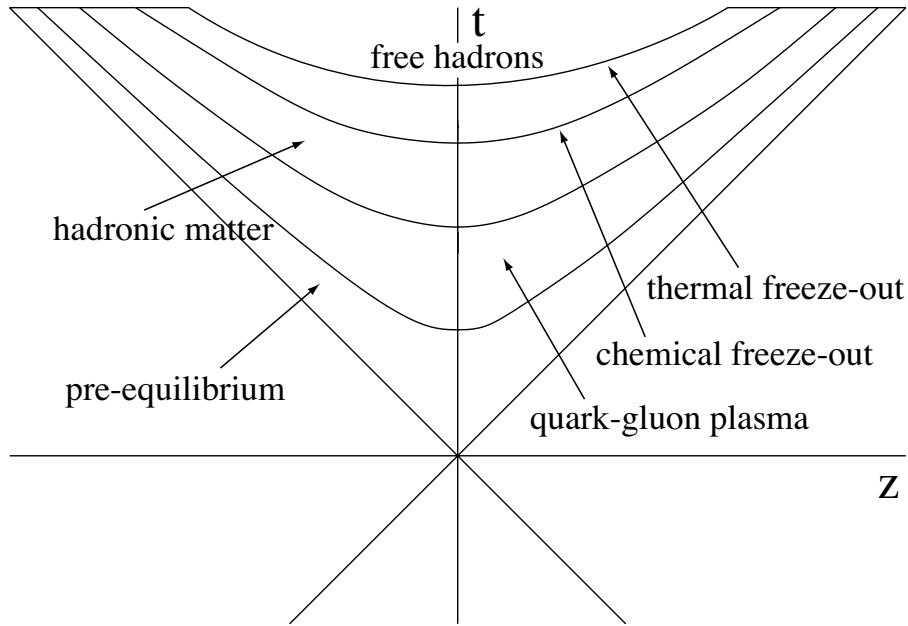


Figure 1.4: Evolution of a heavy ion collision traversing phases and phase transitions in space-time are shown [Sat03]. The system starts in a not equilibrated state, transitions into a quark-gluon-plasma and later into hadronic matter until it ends up as a final state of free hadrons.

where the partons are confined into hadrons. The hadronic matter keeps expanding and cooling and eventually all inelastic interactions will stop. This is called the chemical freeze out, because the particle species are no longer changed by collisions but only by decays. Finally all elastic interactions stop, and the momentum distributions of the particles are fixed. This is commonly referred to as the thermal or kinetic freeze out.

1.2.1 Experimental parameters

In heavy ion collisions there are basically two parameters which can be varied: The collision energy and the system size.

The use of heavy nuclei is necessary to produce strongly interacting matter at a high energy density over a volume, which is large enough to possibly produce a quark-gluon-plasma.

To study the evolution of the observables with the system size from a proton-proton-collision without a QGP to a heavy ion collision possibly with a QGP, lighter ions like carbon, silicon and copper can be collided. As an alternative the centrality of heavy

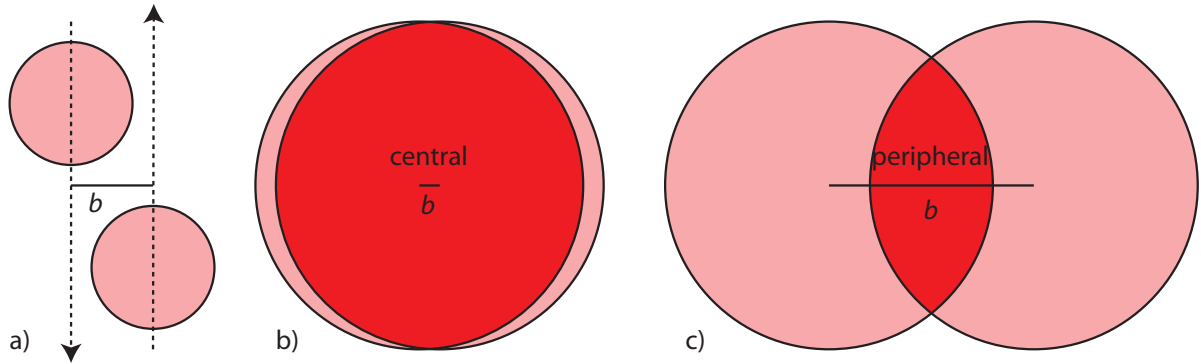


Figure 1.5: In figure a) two nuclei are shown and the trajectories of their centers are indicated by the dashed arrows. The distance between these two trajectories is the impact parameter b . In figures b), c) and d) the view is along the momentum vectors. Figures b) and c) illustrate configurations with different impact parameters corresponding to different centralities.

ion collisions can be varied as shown in figure 1.5. In subfigure a) two nuclei and the trajectories of their centers are shown before the collision. The impact parameter b is defined as the distance between these two trajectories. In the subfigures b), c) and d) the view is along the trajectories. Subfigure b) with a small impact parameter corresponds to a central and subfigure c) with the large impact parameter to a peripheral collision. The dark colored central region indicates the matter which takes part in the collision and corresponds to the volume of the created matter. The light colored regions at the side are the nucleons which do not directly take part in the interaction and are therefore called spectators.

To examine, whether observables are modified by the medium created, asymmetric collisions such as deuteron-gold or proton-lead have been used. In these system there is a heavy nucleus in the initial state, but no large volume of strongly interacting matter is produced.

As a second parameter the collision energy can be varied, which affects the energy density in the created system. It is important to study the evolution of experimental observables over a wide range of energies to identify, what changes point to a phase transition and which ones do not.

1.2.2 Heavy ion accelerator facilities

The first measurements of relativistic heavy ion collisions were made at the Lawrence Berkeley National Laboratory at the BEVALAC, which allowed to accelerate ions beams

to energies of up to 2 AGeV. Later on, the Synchrotron at the Joint Institute for Nuclear Research in Dubna was also used. A more modern machine for a similar energy range is the Schwerionensynchrotron (SIS) at the Gesellschaft für Schwerionenforschung (GSI) in Darmstadt. It offers heavy ion beams up to Uranium at an energy of 1.5 AGeV and lighter ions up to 2 AGeV. The Alternating Gradient Synchrotron (AGS) at the Brookhaven National Laboratory (BNL) offered gold beams up to an energy of 11.7 AGeV and the possibility to study gold-on-gold-collisions at center of mass energies per nucleon pair from $\sqrt{s_{NN}} = 2.68$ GeV to $\sqrt{s_{NN}} = 4.75$ GeV. At the Super Proton Synchrotron (SPS) at CERN beams of lead-ions can be accelerated up to an energy of 158 AGeV and allows to study lead-lead-collisions with up to $\sqrt{s_{NN}} = 17.3$ GeV. Also collisions of lighter nuclei were studied. A new accelerator is planned to be built at GSI. It is expected to accelerate Uranium beams up to an energy of about 20 AGeV.

The Relativistic Heavy Ion Collider (RHIC) at BNL is the first heavy ion collider and was built as a machine dedicated primarily to heavy ion physics. Gold nuclei can be collided at energies up to $\sqrt{s_{NN}} = 200$ GeV as well as lighter systems. The next step in development will be the Large Hadron Collider (LHC) at CERN, which is expected to start running in 2007. While it is originally designed as a proton-proton-collider for energies up to $\sqrt{s} = 14$ TeV, it will also collide lead ions up to energies of $\sqrt{s_{NN}} = 5.5$ TeV.

1.2.3 Observables

A lot of different observables probe the properties of the system at different stages of the collision. Hadrons, which are most of the produced particles in the final state, are affected by interactions until the kinetic freeze out of the system. Therefore it is non-trivial to extract parameters describing the system in the stage of the highest energy density after equilibration and the combination of different observables is necessary to obtain a coherent picture.

The early stage of the collision can be studied by probing the medium with hard partons, which are created in initial hard scatterings of partons in the two colliding nuclei. Due to their very high momentum they traverse the medium, while it is still at a high energy density. By interactions they transfer a part of or all their energy and momentum to the medium before they possibly leave the medium and fragment into a jet of particles. In heavy ion collisions a complete jet reconstruction, which allows to measure the full energy of the parton, is not possible yet due to the large particle multiplicities from soft interactions. Therefore particles with transverse momenta of a few GeV/c are studied. At these momenta particles are mainly produced from hard scatterings and not from the soft processes in the medium. At high RHIC energies it has been observed that, compared to proton-proton-collisions, the number of particles measured at high transverse momenta is suppressed [A⁺02, A⁺03e]. This is after dividing the measurements from heavy ion collisions by the number of initial state nucleon-nucleon-collisions. Angular

correlations of the projection of particle momenta into the plane perpendicular to the beam direction show a correlation peak at low angles in gold-gold-collisions and proton-proton-collisions. While in proton-proton-collisions there is a second peak visible on the opposite side, where the opposite jet is expected, there is no clear peak visible in central gold-gold-collisions [A⁺03g]. In deuteron-gold-collisions at the same energy a similar suppression and modification of the away side jet have not been observed as in gold-gold collisions [A⁺03h, A⁺03d]. The suppression of high transverse momentum particles in Au+Au-collisions is interpreted as energy loss of the particles due to interaction with the medium they have to traverse. Because this suppression is not observed in d+Au-collisions, where no medium is created, which has to be traversed by jet fragments, the conclusion is that the matter produced in Au+Au-collisions is causing the suppression and not the nucleus in the initial state.

Another observable probing the early stage of the collision is elliptic flow: In a non-central heavy-ion-collision the projection of the interaction region into the plane perpendicular to the beam direction has an elliptical shape. Due to the high pressure created in the center of the collision there are pressure gradients from the inside to the outside of the interaction zone. They are much steeper along the minor axis of the ellipse causing a stronger acceleration of particles in this direction. This results in an anisotropy in the momentum distribution. Because the particles are accelerated more along the minor axis of the ellipse, the spacial anisotropy is reduced. As soon as it is gone the momentum anisotropy does not change any longer and should be preserved in the final state of the collision.

In general inclusive particle spectra of hadrons provide a lot of information on the late stage of the collision. Most of these particles have low transverse momenta and are produced thermally by the medium. The ratios of different particles types are sensitive to the chemical freeze out, when the types of the particles are fixed. The shape of the transverse momentum distribution is sensitive to the thermal freeze out, after which particle momenta no longer change.

1.3 Photons in Heavy Ion Collisions

Photons are a penetrating probe in heavy ion collisions, because they only interact electro-magnetically and thus their mean free path in strongly interacting matter is long compared to the size of the created medium. There are several production mechanisms for photons emitted in the course of a heavy ion collision. The sources are initial state hard scattering, interaction of hard partons with the medium, medium production in quark matter and hadronic matter and electromagnetic decay of hadrons. Due to the large number of sources it is important to disentangle the different contributions to the photon spectra. In general one differentiates between photons coming from electromagnetic hadron decays in the final state (decay photons) and photons directly emitted

from the hot nuclear matter (direct photons).

1.3.1 Jets and Photons

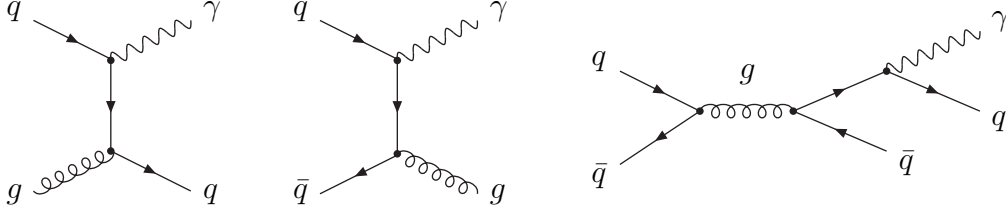


Figure 1.6: Feynman diagrams for the QCD-Compton-scattering, the quark-anti-quark-annihilation and the vacuum Bremsstrahlung.

In the early stage of the collisions quarks and gluons from the nucleons in both nuclei have high relative momenta and can scatter with a high momentum transfer. This can result in quarks, gluons and photons with high transverse momenta. Because color-charged objects like quarks and gluons cannot exist in the vacuum, they will build up a QCD flux tube between themselves and the object they were knocked out from. This tube will eventually fragment into hadrons and photons. Because of the high momentum of the parton, the momenta of most produced particles will be focused into a small cone around the momentum vector of the parton. This is referred to as a jet of particles.

The most common case in hard collisions is the scattering of two incoming partons into two hard partons resulting in the production of two azimuthally opposite jets, a di-jet event. Other configurations are a single jet balanced by a photon, commonly called a γ -jet event, or events with more than two jets, multi-jets, from a single hard scattering. Photon balancing a jet are also called prompt photons.

The dominant production processes for γ -jet events in proton-proton-collisions are the QCD-Compton-scattering and the quark-anti-quark-annihilation shown in the first two diagrams in figure 1.6. The cross sections for these leading order processes, which have been calculated using perturbative QCD, are shown in equations 1.2, 1.3 and 1.4 in terms of the Mandelstam variables (s , u and t) [Owe87]. α is the fine structure constant, α_s the strong coupling constant and e_q the fractional electric charge of the corresponding quark. For comparison the cross sections for the same incident particles without photons in the final state are also given in equations 1.5, 1.6 and 1.7.

$$gq \rightarrow \gamma q \quad \frac{d^3\sigma}{ds du dt} = \frac{\pi\alpha\alpha_s}{s^2} \left(-\frac{e_q^2}{3} \left(\frac{u}{s} + \frac{s}{u} \right) \right) \quad (1.2)$$

$$q\bar{q} \rightarrow \gamma g = \frac{\pi\alpha\alpha_s}{s^2} \left(-\frac{8e_q^2}{9} \left(\frac{u}{t} + \frac{t}{u} \right) \right) \quad (1.3)$$

$$q\bar{q} \rightarrow \gamma\gamma = \frac{\pi\alpha^2}{s^2} \left(-\frac{2e_q^4}{3} \left(\frac{u}{t} + \frac{t}{u} \right) \right) \quad (1.4)$$

$$qq \rightarrow gq = \frac{\pi\alpha_s^2}{s^2} \left(-\frac{4}{9} \left(\frac{s}{u} + \frac{u}{s} \right) + \frac{s^2 + u^2}{t^2} \right) \quad (1.5)$$

$$q\bar{q} \rightarrow gg = \frac{\pi\alpha_s^2}{s^2} \left(\frac{32}{27} \left(\frac{t}{u} + \frac{u}{t} \right) - \frac{8t^2 + u^2}{3s^2} \right) \quad (1.6)$$

$$q\bar{q} \rightarrow q\bar{q} = \frac{\pi\alpha_s^2}{s^2} \left(\frac{4}{9} \left(\frac{s^2 + u^2}{t^2} + \frac{u^2 + t^2}{s^2} \right) - \frac{8}{27} \frac{u^2}{st} \right) \quad (1.7)$$

By comparing the equations it can be seen that the production cross section for prompt photons is several orders of magnitude lower than for jets, mainly due to the two order of magnitude difference in the coupling constants. Not shown are processes with two quarks or two gluons in the initial state, which cannot produce prompt photons in leading order QCD processes ($qq \rightarrow qq$, $gg \rightarrow gg$ and $gg \rightarrow q\bar{q}$) but only jets.

Bremsstrahlung photons are radiated off a parton before the jet fragments. An example for the process is shown in the third diagram in figure 1.6. While it can occur in the vacuum, it can as well be induced by scattering of the parton in the medium. In contrast to the prompt photons these photons don't carry the full momentum transferred in a hard collision but can be part of a jet.

Jets in heavy ion collisions

Before a jet is produced in a heavy ion collision, the parton from the hard scattering can interact with soft particles in the medium while traversing it (see figure 1.8) [BSZ00]. The corresponding loss of energy is referred to as jet-quenching. Photons can be produced in these parton medium interactions via the leading order processes of quark-anti-quark-annihilation and QCD-Compton scattering. The two most important higher order processes contributing to photon production are bremsstrahlung induced by a hard quark scattering in the medium and quark-anti-quark-annihilation after scattering of hard quark in the medium. The corresponding diagrams are shown in figure 1.7. These jet induced photon sources can contribute significantly to the direct photon yield [FMS03].

The initial partonic scattering processes in nucleus-nucleus interactions should be similar to those occurring in proton-proton-interactions, which have been extensively studied at various collision energies. Their production probabilities can be calculated using perturbative QCD. While the partons produced in initial hard scattering interact with the medium, prompt photons (produced as in figure 1.6 graph one and two) pass through the medium without interaction. Therefore the production characteristics of photons

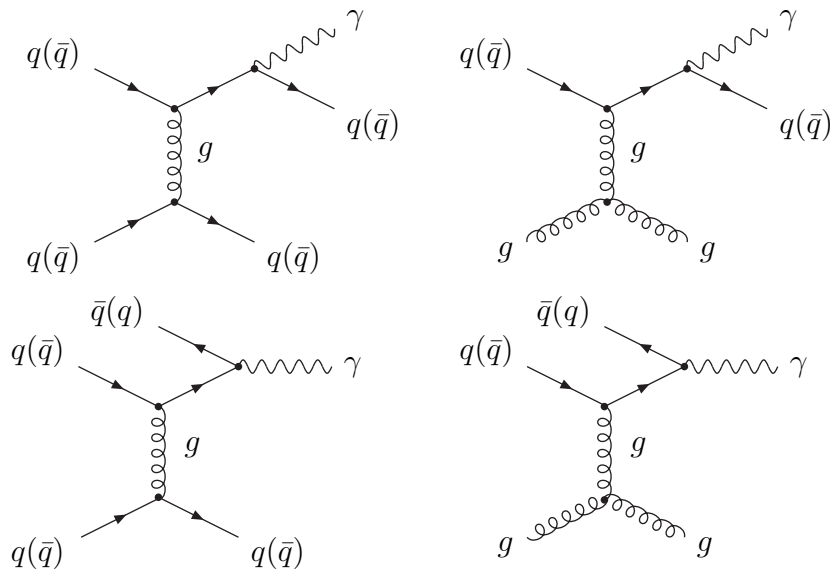


Figure 1.7: Feynman diagrams of two examples for Bremsstrahlung in the medium by strong interaction with quarks and gluons (upper row) and of quark-anti-quark-annihilation after strong scattering off quarks or gluons in the medium. (lower row)

from hard scattering processes are the same as in proton-proton-collisions. The result obtained for proton-proton-collisions are scaled by the number of binary nucleon-nucleon-collisions in a heavy ion collision.

Because the production of prompt photons is well understood and they carry the same momentum as the jet they are recoiling from, they provide a good baseline to study the modification of the opposite jet by the medium [WHS96].

1.3.2 Medium production of Photons

During the entire evolution of the collision photons are produced in soft collisions. There are a lot of different such processes in both the partonic and the hadronic phase.

Calculations for the expected thermal contribution from quark matter were published by Hwa and Kajantie [HK85]. They suggested the thermal component in the photon spectra, which is not reproducible by QCD calculations based on nuclear structure functions, as a signature of the formation of quark matter.

The expected photon production in an equilibrated quark-gluon-plasma has been cal-

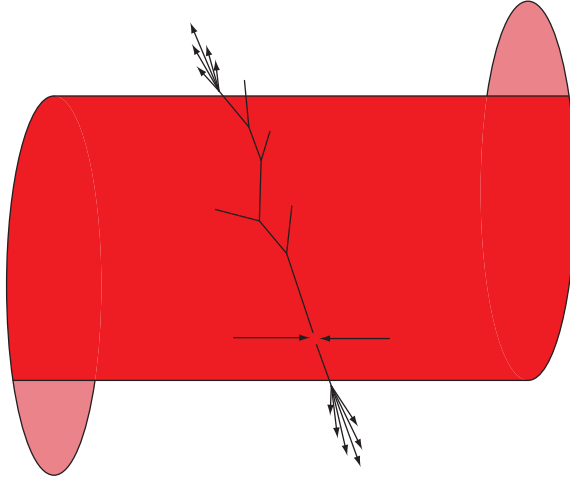


Figure 1.8: Two partons with a large transverse momentum produced in initial hard scattering are shown inside the strongly interaction medium. While the lower one has only a short path length through the medium and escapes unmodified, the upper one scatters several times with soft particles in the medium and loses energy. The jets of particles observed in the final state are illustrated by the two sets of arrows.

culated by Kapusta, Lichard and Seibert [KLS91]. Their calculation is based on QCD Compton scattering ($gq(\bar{q}) \rightarrow \gamma q(\bar{q})$) and quark anti-quark annihilation ($q\bar{q} \rightarrow \gamma g$) processes. The diagrams are the same as for the γ -jet related processes shown in figure 1.6, but are on a different momentum scale due to the lower momentum transfer in a thermalized system. In the same paper they also calculated the emitted photon spectra in the hadronic phase for a gas consisting of π^- , ρ^- , ω^- and η^- -mesons. The processes $\pi\pi \rightarrow \rho\gamma$ and $\pi\rho \rightarrow \pi\gamma$ and the vector meson decays $\omega \rightarrow \pi\gamma$ and $\rho \rightarrow \pi\pi\gamma$ were the main photon sources in the hadronic phase. Their conclusion was that the spectra of photons emitted from a quark-gluon-plasma are the same as those emitted from a hadron gas at the same temperature.

Arnold *et. al.* [AMY01] studied photon production in a quark-gluon-plasma due to bremsstrahlung in the medium, $qg \rightarrow q\gamma$, and inelastic pair annihilation, $q\bar{q}g \rightarrow \gamma$. The diagrams for both processes are shown in figure 1.7. They concluded that these two processes contribute to the same order as the QCD-Compton scattering and quark-anti-quark-annihilation to the photon spectra emitted from a quark-gluon-plasma, and included them in their calculation.

More recent calculation for the photon yields from a hadron gas take into account strange mesons and resonances, of which especially the a_1 -resonance contributes significantly to the photons spectra [Hag04, TRG04].

1.3.3 The composition of direct photon spectra

Most calculations predicted the photon spectra emitted from an equilibrated quark-gluon-plasma or hadron gas at a constant temperature. A heavy ion collision, however, is an evolving system as illustrated in figure 1.4. It starts in an early un-equilibrated phase, in which there is no temperature defined but photons are produced. Depending on the initial energy this system can equilibrate either into a quark-gluon-plasma or a hadron gas, from which additional thermal photons are emitted. Due to the fast expansion of the system it cools down rapidly traversing the phase transition to a hadron gas if it was a quark-gluon-plasma, until it freezes out into its final state, where the production of thermal photons stops.

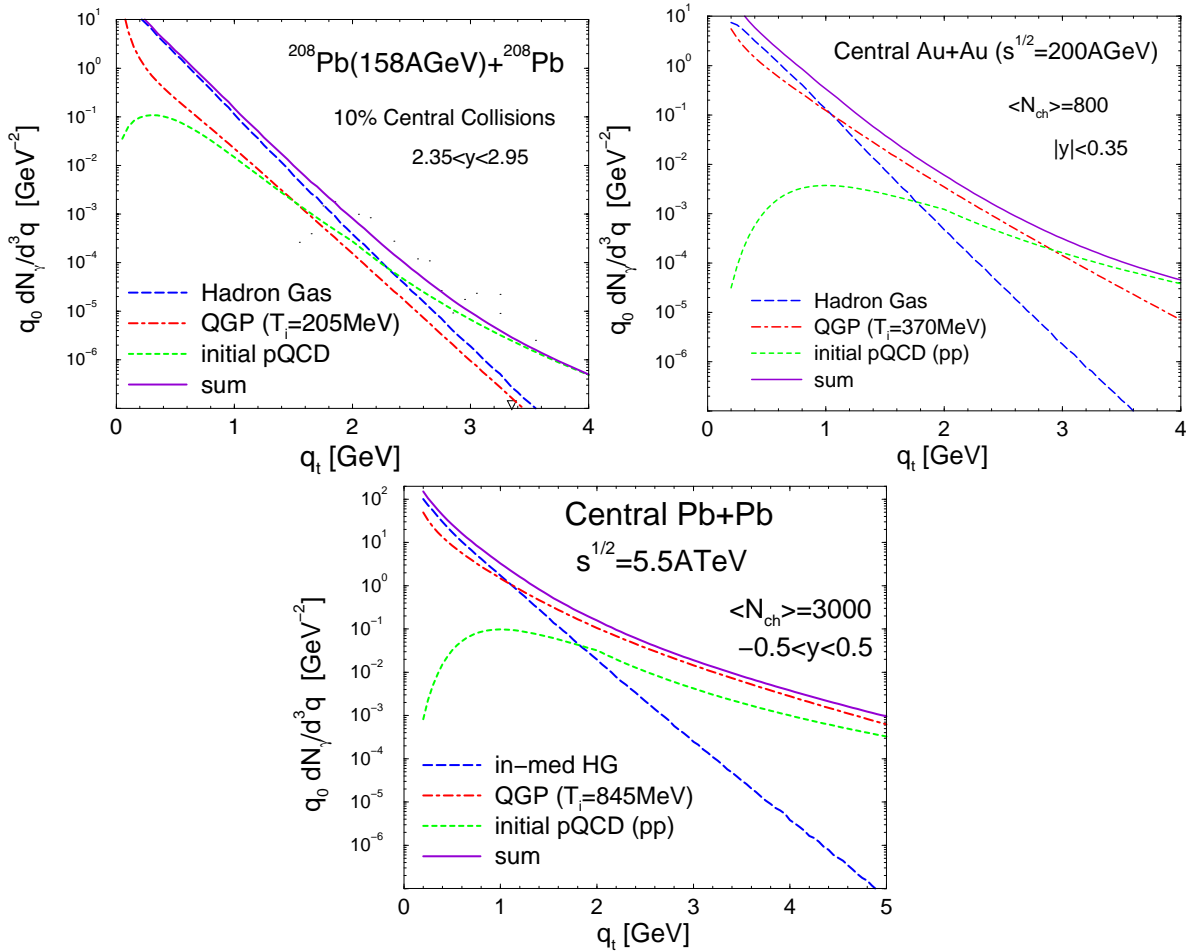


Figure 1.9: Calculation of contributions to the direct photon spectra from hard collisions and thermal photons from a quark-gluon-plasma and hadronic matter at SPS, RHIC and LHC energies [TRG04].

Turbide, Rap and Gale used an expanding fireball model to take the evolution of a

heavy ion collision into account [TRG04]. They compared the contributions from initial hard scattering using perturbative QCD, from the quark-gluon-plasma and from the hadron gas to the photon spectra at the highest SPS, RHIC and LHC collision energies of $\sqrt{s_{NN}} = 17.2 \text{ GeV}$, $\sqrt{s_{NN}} = 200 \text{ GeV}$ and $\sqrt{s_{NN}} = 5500 \text{ GeV}$ respectively. As shown in figure 1.9, photons from each stage dominate a different region in transverse momentum at different collision energies. At RHIC the dominant contribution above $3 \text{ GeV}/c$ comes from initial scattering described by perturbative QCD. Between $1 \text{ GeV}/c$ and $3 \text{ GeV}/c$ the main contribution is expected to be thermal photons from the quark-gluon-plasma phase. Below $1 \text{ GeV}/c$ transverse momentum the dominant contribution are the thermal photons from the hadron gas in the late stage of the collision. Therefore this model predicts that the region between $1 \text{ GeV}/c$ and $3 \text{ GeV}/c$ transverse momentum is suited best to measure the temperature of a quark gluon plasma produced in Au+Au-collision at RHIC.

1.3.4 Decay Photons

In the final state of the collision several meson species decay electromagnetically into photons. The largest contribution comes from the π^0 -meson decays $\pi^0 \rightarrow 2\gamma$ and $\pi^0 \rightarrow e^+e^-\gamma$ with a branching ratio of 98.798% and 1.198% respectively. The η -meson decays $\eta \rightarrow 2\gamma$ with a branching ratio of 39.43%. These two sources produce about 99% of the photons coming from the decay of particles. Other contributions come mainly from η' - and ω -mesons.

Due to the large abundance of the π^0 - and η -mesons they are the source of most of the photons measured in a heavy ion collisions. To show the composition of the photon spectra from decays, proton-proton-events at an energy of $\sqrt{s} = 62 \text{ GeV}$ have been simulated using the Pythia event generator [SLM01, S⁺01]. The contribution of the different photon sources to the transverse momentum spectra are shown in figure 1.10. It can nicely be seen that the decay photons dominate the spectra below $4 \text{ GeV}/c$ and the contribution photons related to hard processes becomes significant at higher transverse momenta. Also at each transverse momentum in the shown range photons from π^0 - and η -decays make up at least 96% of the decay photons. While these simulations show the composition of the inclusive photon spectra in proton-proton-collisions, heavy ion collisions include in addition thermal photons from partonic and hadronic matter. To determine the contribution of the decay photons to the inclusive photon spectra, the spectra of the decaying particles have to be known. These can be used as input to calculate the yield of photons and the shape of the resulting photon spectra from the decays. The ratio of inclusive photons to photons from electro-magnetic decays has been measured by the PHENIX collaboration at a collision energy of $\sqrt{s_{NN}} = 200 \text{ GeV}$ and is shown in figure 1.12 on the left side [A⁺05]. Only for transverse momenta above $4 \text{ GeV}/c$ the ratio becomes significantly larger than one. In the most central bin the direct photons become the dominant contribution to the photon spectra above $6 \text{ GeV}/c$

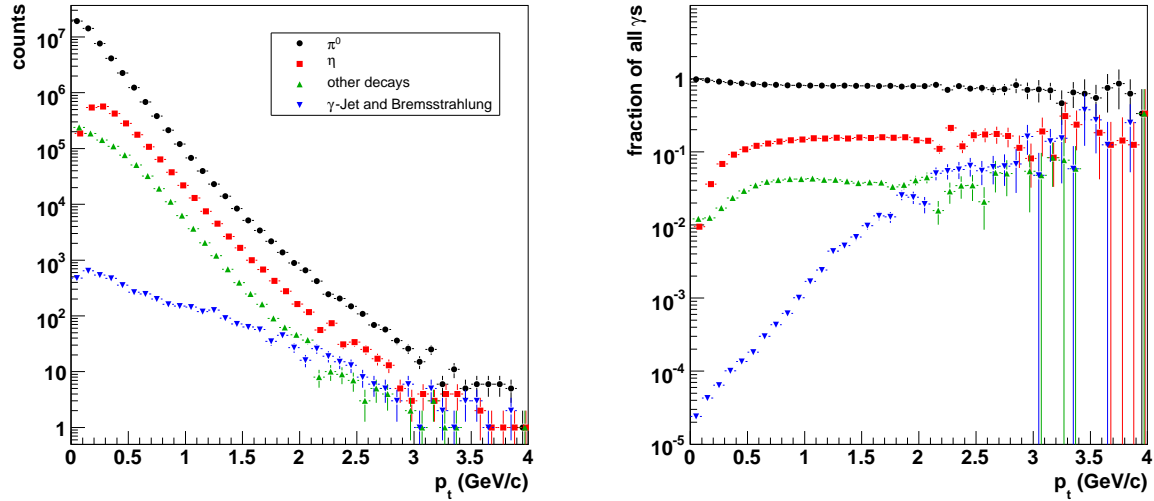


Figure 1.10: The different contributions to the photon transverse momentum spectra in proton-proton-collisions at $\sqrt{s_{NN}} = 62 \text{ GeV}$ from different electromagnetic hadron decays, from γ -jets and from bremsstrahlung-photons are shown on the left side. On the right side the ratios of the photons from different sources to the total inclusive photon spectra are plotted. These spectra and ratios were obtained from Pythia-simulations [SLM01, S⁺01]. They simulate p+p-collisions and therefore do not include any thermal components. However they show nicely, which are the predominant decays contributing to the photon spectra as well as what the relative size of the jet contribution is.

transverse momentum. The experimental results are discussed in detail in the next section.

1.4 Direct photon measurements

1.4.1 WA98

The WA98 collaboration determined the direct photon contribution from their photon spectra in Lead-Lead-collisions at the CERN SPS. The center of mass energy in these collisions was $\sqrt{s_{NN}} = 17.3 \text{ GeV}$ [A⁺00].

Their results show no significant excess of photons over the photon contribution from meson decays in peripheral Pb-Pb-collisions in figure 1.11 on the top of the left side. The

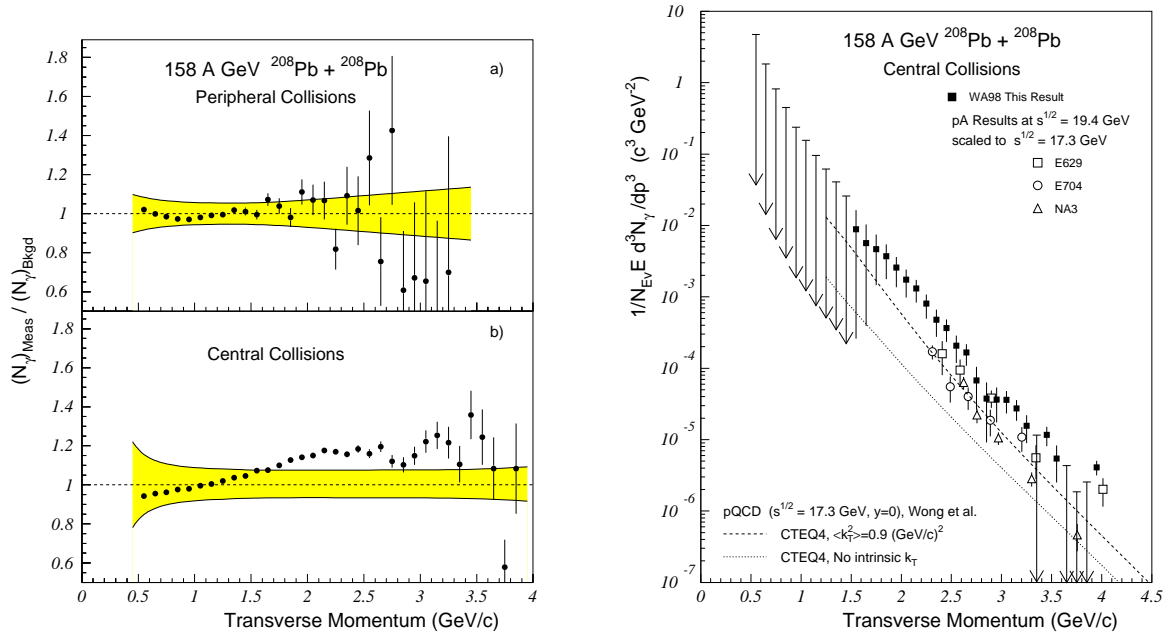


Figure 1.11: On the left side the ratio of inclusive photons over the expected background from meson decays is shown for peripheral and central Pb+Pb-collisions at $\sqrt{s_{\text{NN}}} = 17.3$ GeV measured by WA98 [A⁺00]. The figure on the right side shows the direct photon spectra in central Pb+Pb-collisions.

bottom left plot shows a significant excess of direct photons at a transverse momentum of more than 1.5 GeV/c. The resulting direct photon spectra are shown on the right side. Measurements in proton-nucleus-collisions, which were scaled to take into account the different energy and number of binary nucleon-nucleon-collisions, are shown for comparison. The comparison shows a higher photon emission rate in Pb+Pb-collisions than in p+A-collisions. This additional photon yield may be attributed to thermal photon production in the medium.

1.4.2 PHENIX

The PHENIX collaboration has published results on direct photon measurements in Au+Au-collisions at an energy of $\sqrt{s_{\text{NN}}} = 200$ GeV [A⁺05]. It shows a significant enhancement of the inclusive photon spectra over the expected background from meson-decays for transverse momenta above 4 GeV/c in central collisions as shown in figure 1.12 on the left side. The actual quantity plotted is the double ratio. In the numerator is the ratio of measured photons to measured π^0 -mesons. The denominator is the ratio of the

photon spectra obtained from decay simulations of a π^0 -spectrum to this π^0 -spectrum. The advantage of this double ratio is that some systematic errors cancel. Their photon spectra after subtraction of the contribution from meson decays also is shown in figure 1.12 on the right side.

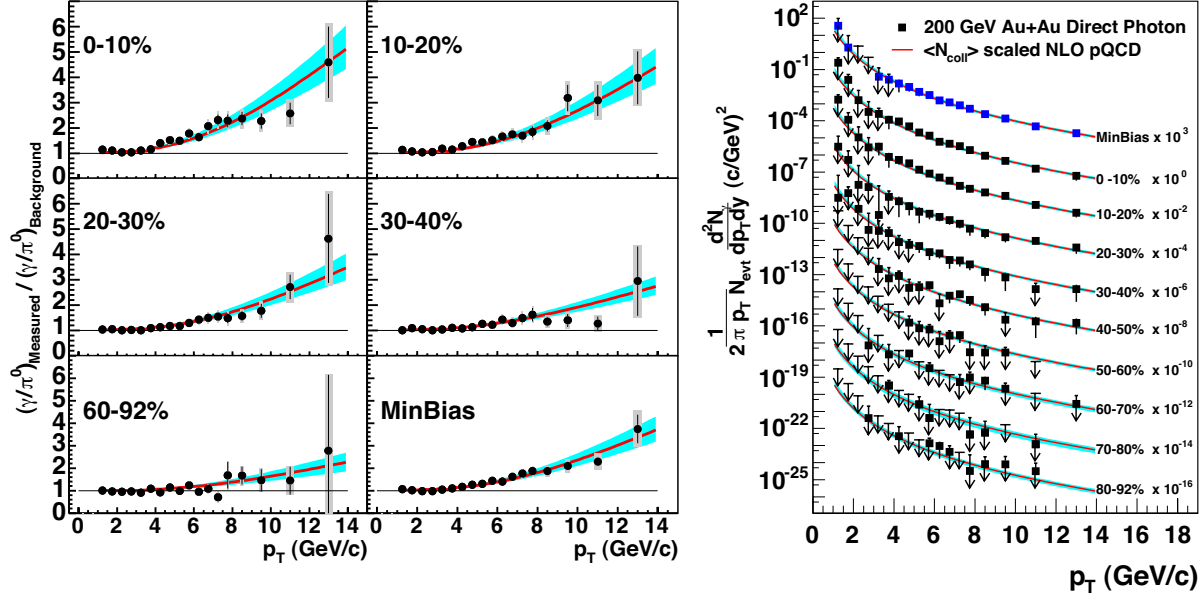


Figure 1.12: The figure on the left side shows the double ratio of measured to background photon to π^0 ratios in Au+Au-collisions. It is measured by the PHENIX collaboration at a collision energy of $\sqrt{s_{\text{NN}}} = 200$ GeV. On the right side direct photon spectra are shown. The lines in both plots are QCD based calculations [A⁺05].

The uncertainty on the direct photon spectra is large below 4 GeV/c transverse momentum in central collisions and therefore only allows the determination of upper limits on the direct photon spectra for this phase space region. At higher momenta, however, the uncertainties are much smaller. As shown earlier the main contribution to the direct photon spectra at RHIC above 3 GeV/c transverse momentum is coming from initial hard scattering. The particle production in initial hard scattering can be calculated using perturbative QCD. This provides particle production cross sections at large transverse momentum in proton-proton-collisions. Therefore the results are scaled by the number of binary nucleon-nucleon-collisions in a heavy ion collision at the respective centrality. The lines on both plots in figure 1.12 show these perturbative QCD calculations. They are nicely in agreement with the data.

To study the modification of jet production in heavy ion collisions R_{AA} is used, which is defined as

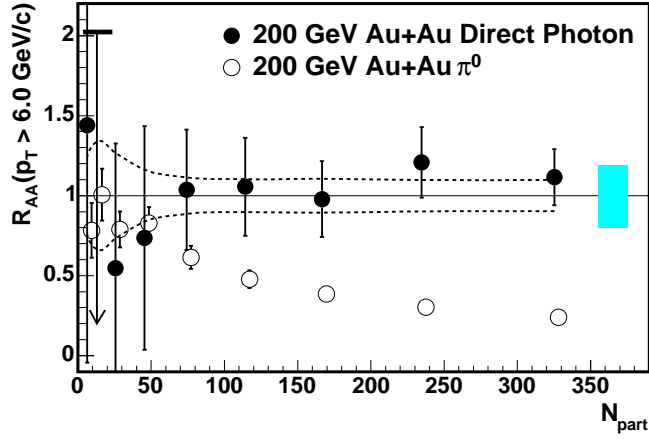


Figure 1.13: The R_{AA} for photons and π^0 -mesons with transverse momenta above 6 GeV/c are shown [A⁺05].

$$R_{AB} = \frac{d^2/dp_t d\eta}{T_{AB} d^2\sigma_{pp}/dp_t d\eta} \quad (1.8)$$

This is the ratio of the yield of particles observed in A+A-collisions to the cross section in proton-proton-collisions after scaling by the number of binary nucleon-nucleon-collisions, which is the factor T_{AB} . R_{AA} was calculated by PHENIX as a function of centrality for direct photons and π^0 -mesons. The result for particle spectra integrated above 6 GeV/c transverse momentum is shown in figure 1.13. While the π^0 - R_{AA} is close to one for peripheral and drops to about 0.2 for central collisions, the photon- R_{AA} is consistent with one for all centralities within systematic uncertainties. This shows that the photon production at large transverse momentum is not strongly modified in heavy ion collisions. Because photons are not strongly interacting, they penetrate the medium created in the final state largely without interaction. This indicates that the initial state of an A+A-collision is not much different from a p+p-collision. Rather the suppression of strongly interacting particles is an effect caused by their interaction with the medium produced in the final state.

This standard PHENIX photon measurement using the calorimeters extends down to low transverse momenta of about 1 GeV/c, but the systematic errors below 3 GeV/c are similar to the measured direct photon contribution and thus no significant signal is visible. However there exists an alternative approach to measure the direct photon contribution to the inclusive photon spectra in this region [Bat05]: The analysis of low mass di-lepton pairs allows to determine the ratio of direct virtual photons and virtual photons coming from π^0 , η and other Dalitz decays. This ratio should be equal to the ratio of direct photons to photons from π^0 , η and other decays. This has been measured

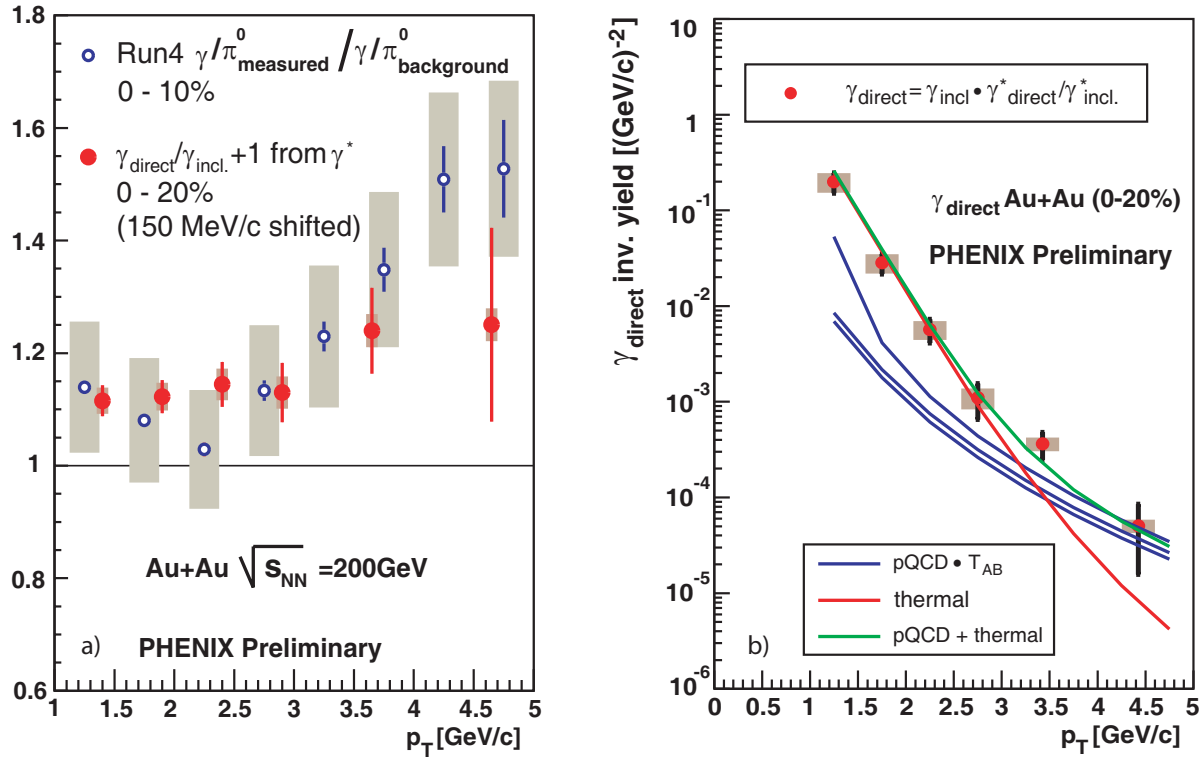


Figure 1.14: Direct photon measurements from PHENIX in Au+Au-collisions at $\sqrt{s_{NN}} = 200$ GeV [Bat05]. On the left side the blue open circles show the direct photon contribution for photons measured in the calorimeter to photons from electromagnetic meson decays. The red solid circles show the direct photon contribution to photons from electromagnetic decays measured using virtual photons. On the right side the photon spectrum resulting from the virtual photon method is shown by the red solid circles. The curves are calculations from a thermal model and scaled perturbative QCD.

by PHENIX. The result is shown in figure 1.14 on the left side (red solid circles). In this case it is plotted as the ratio of direct to the inclusive photon yield plus one. The ratio of direct photons to inclusive photons in the transverse momentum range of 1 – 3 GeV/c is between 10 and 15%. On the right side of figure 1.14 the direct photon spectra are shown. It was obtained by multiplying the ratio of direct to inclusive photons from the virtual photon method by the photon spectra from the calorimetric measurement. The curves on the plot are calculations from perturbative QCD and a thermal model, which together describe the data nicely within the systematic uncertainties. The quoted systematic errors for the direct photon spectra are 25% and are dominated by the η/π^0 -ratio measurement.

1.4.3 Future measurements at LHC

At the large hadron collider the center of mass energy of a Pb+Pb-collision will be up to $\sqrt{s_{NN}} = 5500 \text{ GeV}$ per nucleon pair. Due to the higher incident energy the temperature of the thermalized system will be higher than at RHIC. As a result the thermal photon spectra will be harder and the system will remain in the phase of a quark-gluon-plasma longer. As it is illustrated in figure 1.9, the direct photon spectra between $1 \text{ GeV}/c$ and $5 \text{ GeV}/c$ transverse momentum may be dominated by the thermal photons emitted from the quark-gluon-plasma.

At the LHC collision energy the cross sections for jets will be much higher than at the highest RHIC energy. Therefore the contribution of γ -jets and jet related photons will be higher than at RHIC. The average transverse momenta in a hard collision will be much higher, which will make the measurement of the energy of a jet much more precise, because the difference relative to the thermal background from the event will be much larger.

1.5 Photon measurement at STAR

As it has been discussed in this chapter, direct photons in different transverse momentum regions probe different stages of heavy ion collisions. PHENIX has shown that direct photons in the perturbative regime, which at RHIC starts at about $4 \text{ GeV}/c$ transverse momentum, can nicely be measured with its calorimeters in central collisions. A similar measurement should be possible with the STAR calorimeters.

At RHIC photons below $3 \text{ GeV}/c$ transverse momentum are expected to come mainly from thermal photon production in the medium and therefore probe the temperature of the medium. In this region, however, the calorimetric measurement of PHENIX was subject to systematic uncertainties, which are large compared to the direct photon contribution to the inclusive photon spectra. Therefore different measurement techniques in this regime can turn out to be more successful. Phenix used the measurement of di-lepton pairs or virtual photons to determine the ratio of direct photons to decay photons.

Another possibility is to measure the inclusive photon spectra in this transverse momentum range more precisely. In STAR the main detector is a time projection chamber (TPC), which is a tracking detector for charged particles. While a photon is not charged, it can convert in the electro-magnetic field of a nucleus or the atomic shell to a pair of an electron and a positron. These two daughter particles can be measured in charged particle tracking detectors as the STAR TPC and subsequently be used to reconstruct the photon they originated from.

The main disadvantage of this method is that the STAR experimental setup was designed to have as little material as possible between the interaction point and the TPC to increase the momentum resolution of the detector and minimize lepton production from photon conversions. Because STAR is not optimized to measure conversions, the detection efficiency of photons is below 10% and the systematic uncertainties are not well known. However, the statistical limitation due to the low efficiency is not really a problem for the transverse momentum region below 3 GeV/ c , where lots of particles are produced.

This method has already been used at STAR in Au+Au-collisions at $\sqrt{s_{\text{NN}}} = 200$ GeV [A⁺04, Joh03]. In the end it yielded no significant result for the direct photon spectra. Newly available data sets at center-of-mass energies of $\sqrt{s_{\text{NN}}} = 62$ GeV and $\sqrt{s_{\text{NN}}} = 200$ GeV contain several times more recorded collisions and therefore allow to reduce the statistical errors. Also the systematic uncertainties can be studied in much more detail.

The subject of this thesis work was to explore the possibilities of STAR to provide an independent measurement on the direct photon production in the transverse momentum region, which at RHIC is presumably dominated by thermal photon production from a quark-gluon-plasma. This will be tested by using the data set of Au+Au-collisions at $\sqrt{s_{\text{NN}}} = 62$ GeV to measure inclusive photon- and π^0 -spectra. This includes a detailed study of all systematic uncertainties in this analysis. In the end an estimate on the magnitude of the direct photon contribution to the inclusive photon spectra will be given including all systematic uncertainties.

2 The STAR experimental setup

2.1 Accelerators

The STAR detector is one of four detectors at the Relativistic Heavy Ion Collider (RHIC [HLO03, H⁺03]) at Brookhaven National Laboratory designed to study heavy ion collisions. RHIC is fed by a series of other accelerators, which are illustrated in figure 2.1.

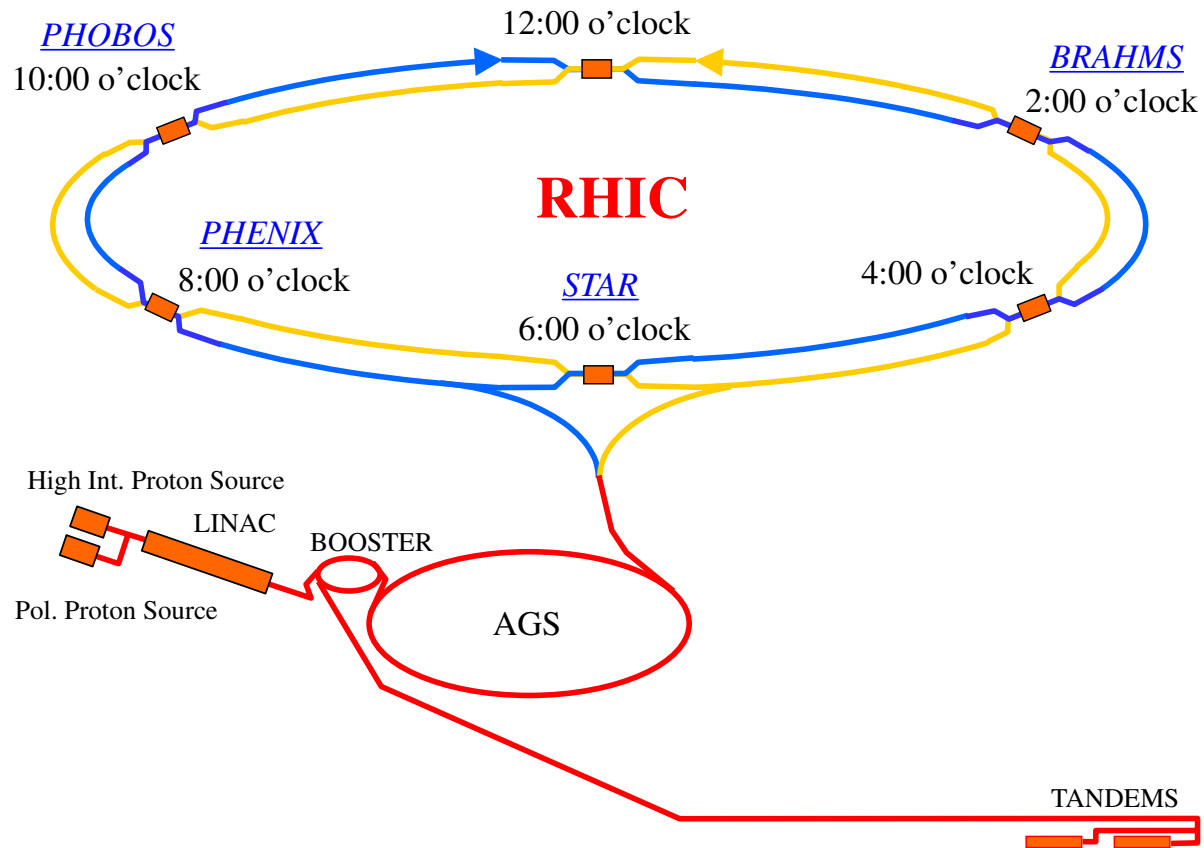


Figure 2.1: RHIC and supporting accelerators.

There are two different ion sources available: A linear accelerator is used to create and preaccelerate protons to a kinetic energy of 200 MeV, while in a Tandem-Van-de-Graaf accelerator a large variety of ions can be produced with a kinetic energy of 1 MeV/u. So far in RHIC running deuteron, gold and copper ions have been used. Beams from these sources are injected into the booster ring. Here gold ions are accelerated to 95 MeV/u before they are injected into the Alternating Gradient Synchrotron (AGS), where they are again accelerated to a kinetic energy of 8.86 GeV/u, while protons are accelerated to 24.3 GeV. Then the particles are injected into RHIC via the AGS to RHIC transfer line (AtR).

RHIC consists of two concentric accelerator rings, which have six common interaction

points. The lowest energy at which RHIC is operated is without any further acceleration after the injection, which results in a center of mass energy of $\sqrt{s_{NN}} \approx 19.6$ GeV for gold ions and $\sqrt{s_{NN}} \approx 50$ GeV for protons. The maximum energy is $\sqrt{s_{NN}} \approx 200$ GeV for gold-gold- and $\sqrt{s_{NN}} = 500$ GeV for proton-proton-collisions.

A special feature of the whole accelerator system is that beams of polarized protons can be accelerated and kept polarized while stored in the RHIC rings.

Besides the STAR detector there are three other experiments studying heavy ion collisions: The PHENIX experiment [A⁺03f] was designed to focus on rare probes like direct photons, quarkonia and lepton pairs. At mid-rapidity it provides charged particle tracking with drift and pad chamber and particle identification with time of flight and ring imaging Cherenkov detectors. Electromagnetic calorimeters measure the energy of photons and electrons. At forward rapidities there are two muon spectrometers, consisting of a drift chamber for tracking and alternating steel absorbers and streamer tubes for muon identification.

BRAHMS [A⁺03c] was primarily designed to measure identified particle spectra over a wide phase space. It consists of two spectrometers at forward and mid-rapidity, which are composed of time projection chambers, time of flight and ring imaging Cherenkov detectors. The pseudo-rapidity coverage of both arms together extends from 0 up to 4 for charged pions, however the solid angle of each spectrometer is small. Therefore only small angle correlation measurements are possible.

The PHOBOS detector [B⁺03a] was designed to measure yet unknown new event signatures. For that it is necessary to measure particles in a large fraction of phase space and record a large fraction of all events without too restrictive trigger conditions. This is accomplished by a cylindrical silicon multiplicity detector, covering almost the entire phase space available in heavy ion collisions at RHIC. In addition there is a silicon based spectrometer and time of flight detector near mid-rapidity. Due to the large acceptance close to 4π -multiplicities and large angle correlations of charged particles can be measured with PHOBOS.

2.2 STAR

The Solenoidal Tracker At RHIC (STAR) [A⁺03b] was designed to measure a wide range of observables in heavy ion collisions. It is in particular suitable to measure event-by-event fluctuations, correlations and jets, which require a large acceptance, good momentum resolution for large transverse momenta and calorimetry. Particle identification provides the possibility to study those observables for different particle species and identified particle spectra. The second purpose of the STAR detector is to measure polarized proton collisions, for which some of the detectors were explicitly designed.

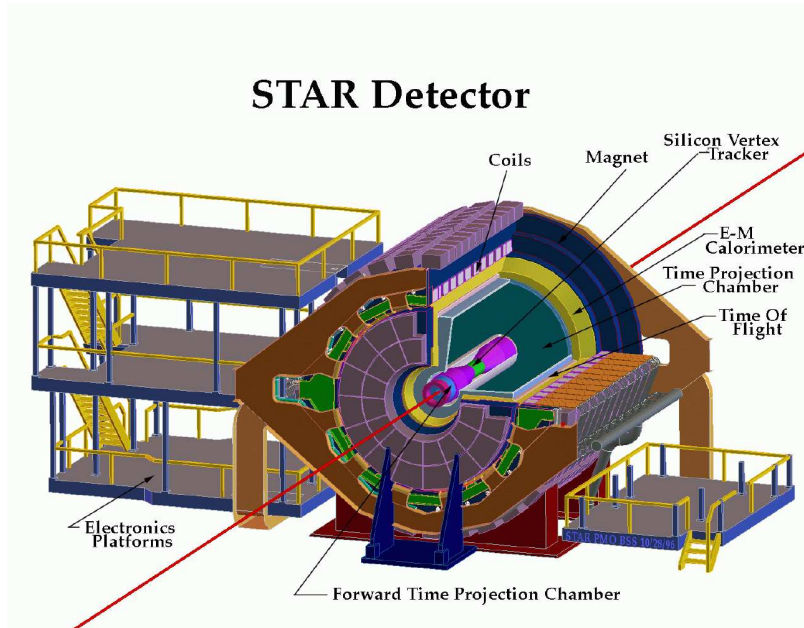


Figure 2.2: Schematic view of the STAR detector setup.

Most detectors are located inside a large solenoidal magnet as shown in figures 2.2 and 2.3. The main tracking detector is a Time Projection Chamber (TPC), which provides the high resolution tracking necessary for the multiplicities encountered in heavy ion collisions, which can be more than 1000 particles per pseudo-rapidity unit in a central Au+Au-collision at RHIC.

Two additional silicon tracking detectors, the SVT and SSD are located closer to the beam line than the TPC. They are designed to improve on distinguishing tracks from the main event vertex from tracks coming from secondary vertices. For tracking at forward rapidities there are two Forward Time Projection Chambers (FTPC) on either side of the inner silicon tracking. To measure π^0 and photonic contribution to jets, the time projection chamber is surrounded by two electro-magnetic calorimeters, one cylindrical to cover the phase space near mid-rapidity and one between one end cap of the TPC and the corresponding end cap of the magnet to cover forward rapidities.

2.2.1 The STAR coordinate system

The STAR experimental setup uses a right-handed Cartesian coordinate system with the origin in the center of the detector. The z axis is defined by the beam axis. Positive values are on the western side. The y axis is vertical with positive values pointing up. The x axis in the horizontal plane perpendicular to the beam axis.

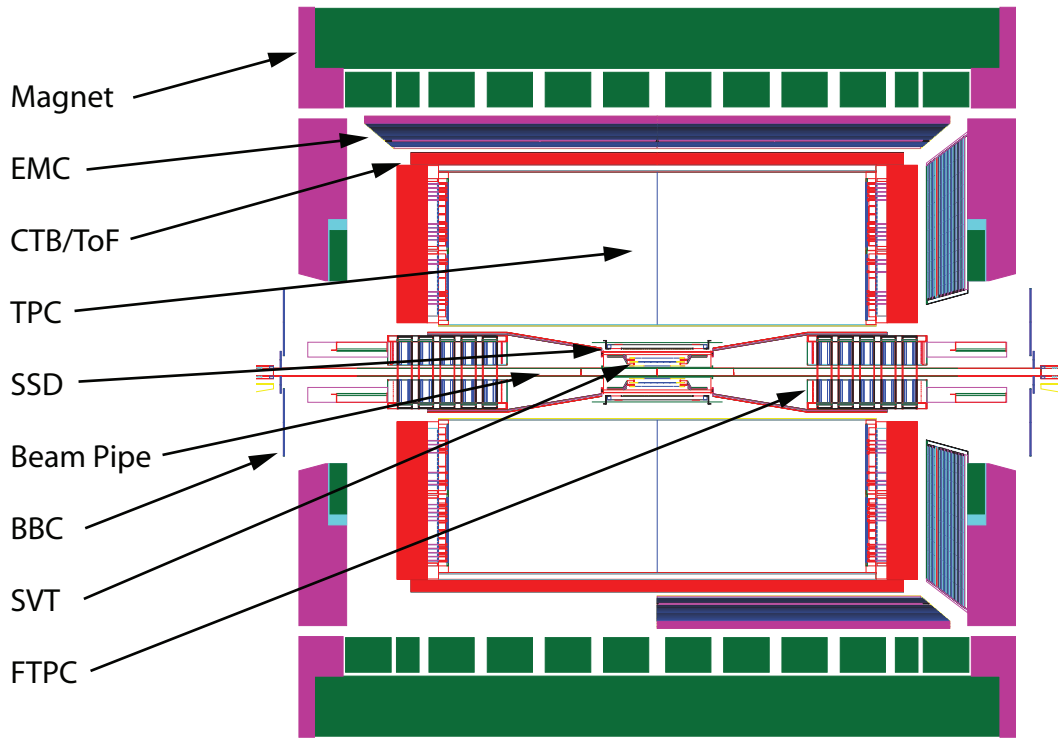


Figure 2.3: Cut through the STAR detector

Due to the cylindrical symmetry of large parts of the experiment, the use of a cylindrical coordinate system is useful. The azimuthal angle ϕ is defined as $x/\sqrt{x^2 + y^2} = \cos(\phi)$ and $y/\sqrt{x^2 + y^2} = \sin(\phi)$. The radial component is $r = \sqrt{x^2 + y^2}$, while the longitudinal variable z is the same as used in the rectangular coordinate system. In addition it is useful to define the *dip*-angle as $z/r = \tan(\text{dip})$.

2.2.2 Magnet

The magnet is a solenoid with the field in its center aligned with the beam line [B⁺03d]. For physics data taking the magnet is usually operated with a field of 0.5 T. Both polarizations of the field are used. To enhance the tracking capabilities for particles with low transverse momentum, the magnet can be used with half of the normal field. The shape of the field in the volumes of the tracking detectors is relatively homogenous: For the full field configuration the radial component of the field is smaller than 50 G, the azimuthal component smaller than 3 G and for the half field configuration half of that. The homogeneity of the field is important for the momentum resolution of tracks in the TPC.

2.2.3 Inner parts of the experimental setup

Data from the detectors between the beam and the Time Projection Chamber are not used for the analysis discussed in this thesis. Instead the material they are made of is used as a medium, which converts photons into e^+e^- -pairs. The crucial information is the distribution and density of the material making up these components.

Beam pipe

The beam is surrounded by the beam pipe [M⁺03]. The center part from -76.2 cm to 76.2 cm consists of Berillium. This material was chosen because of its low density and low nuclear charge to minimize the number of photon conversions and multiple scattering of particles traversing the beam pipe. The outer radius in this section is 4 cm and its thickness 1 mm. For the region extending from ± 76.2 cm to ± 402.59 cm the beam pipe is made of Aluminium and for z larger than ± 402.59 cm of stainless steel.

Silicon Vertex Tracker

The Silicon Vertex Tracker (SVT [B⁺03c]) consists of three layers of silicon wafers. Each wafer is 63 mm long and 63 mm wide. The wafers are arranged in ladders, which contain the carrier material and the readout electronics. Each layer is composed of several ladders. The average thickness of the whole detector is about 6% of a radiation length.

Silicon Drift Detector

The Silicon Drift Detector (SSD [A⁺03l]) consists of one layer of ladders installed at a radius of 230 mm. Each ladder consists of 16 wafers which are 73 mm wide and 40 mm long. The total length of a ladder including the support structure is 1060 mm. The thickness of a ladder is estimated to be 1% of a radiation length.

The number of layers varies for the different running periods. During RHIC run 3 there was only one ladder present. For run 4 10 ladders were mounted covering a quarter of the azimuth at the top and a quarter at the bottom of the acceptance. The complete detector consisting of 20 ladders and covering the full azimuth was finally commissioned for run 5.

2.2.4 Time Projection Chamber

The Time Projection Chamber (TPC [A⁺03k]) is the main detector of the STAR experimental setup and, except for triggering, the only detector used for this analysis. It has the shape of a cylinder and is located around the SSD. It is 4.2 m long and has a diameter of 4 m. The coverage for charged particle tracking reaches up to ± 1.8 units of pseudo-rapidity, however the length of tracks decreases for particles with a pseudo-rapidity above 1 and thus for most purposes the useful acceptance is limited to ± 1 units of pseudo-rapidity.

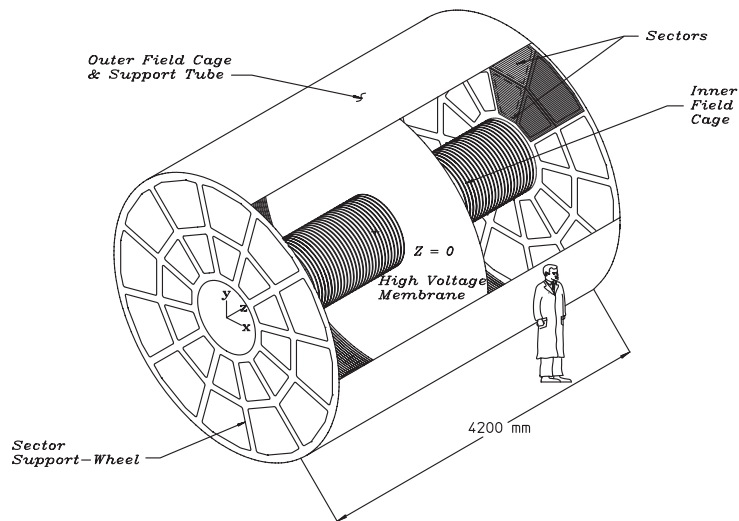


Figure 2.4: The STAR time projection chamber [A⁺03k].

The TPC is filled with a mixture of Methane and Argon. The electric drift field is parallel to the magnetic field. The cathode is a thin conductive membrane in the center of the detector at a potential of 28 kV. The readout planes on both endcaps of the cylinder are at ground potential. They are segmented into 12 sectors. Each sector has 45 pad rows. 13 pad rows are located between the radii of 60 and 119.6 cm with a relatively large distance between the rows and small pads to optimize the two-track resolution. The remaining 32 rows are located between 127.2 and 189.2 cm radius with a smaller spacing and larger pads, to accumulate as much of the created charge as possible to maximise the energy loss measurement resolution.

The acceptance of particles originating from the main vertex has a lower cutoff in transverse momentum, because the trajectories of low momentum particles are curved too much to reach the TPC and leave a track of sufficient length in the TPC gas. A charged particle track at mid-rapidity originating from the main vertex needs about 90 MeV/c

transverse momentum to cross the the first twelve pad rows.

For the analysis of photon conversions the situation is a bit different: Because photons are neutral their momentum will not be affected by the magnetic field. The e^+ and e^- produced in a photon conversion are affected, but they originate from the conversion vertex, which can be at any radius in the detector. This results in a lower transverse momentum cut off for e^+ and e^- originating from photon conversions close to or in the TPC gas. If the photon converts beyond 100 cm radius, where the pad row spacing decreases, the cut off is even lower because tracks can reach the required number of points with a smaller radius. This way photons can be measured down to below 100 MeV/c transverse momentum even though their momentum is split on the two conversion products, but due to the low conversion probability in the gas relative to the SVT and SSD, the photon detection efficiency is very small at low transverse momentum.

Besides tracking the TPC measures the energy loss (dE/dx) of the charged particles traversing the gas with a resolution of 7%. Together with the momentum this offers good particle identification for π^+/π^- , protons, kaons and deuterons at momenta with $\beta \ll 1$. For electrons and all the other particles at relativistic momenta with $\beta \approx 1$, the energy loss reaches the relativistic plateau region of the Bethe-Bloch-Function. In this region the energy loss for all particle species is similar and the distributions overlap, which makes track-wise particle identification impossible. However, particles can be identified on a statistical basis up to several GeV/c transverse momentum.

Inner field cage

The inner wall of the field cage is located at a radius of 468 mm. It consists of a 12.7 mm layer of Nomex as a support material, which is enclosed on each side by a sandwich of two layers of 0.01 mm Aluminium and one layer of 0.075 mm Kapton. The total thickness of the structure adds up to 0.52% of a radiation length. The space between the field cage and the SSD is filled with N_2 -gas, which contributes an additional thickness of 0.1% of a radiation length. A resistor chain is mounted parallel to the beam at an azimuthal angle of 1.9 rad on the inner side of the field cage. The contribution to the radiation length is not calculated, but using photon conversions it is estimated to be 20% of the total conversion probability in the inner field cage.

TPC gas

The TPC gas is P10, a mixture of 90% Argon and 10% Methan. The gas is kept at 2 mbar above atmospheric pressure and at a constant temperature of about 24.9 °C. The gas volume has an inner radius of 500 mm and an outer radius of 2000 mm. This results in a total thickness of 1.17% of a radiation length. An example how that can be

calculated is shown in section 3.2.1.

Outer field cage

The outer field cage is of a similar design as the inner field cage, but instead of Aluminium Copper was used and the overall thickness is higher by about 1.26% of a radiation length. However, conversions taking place in the outer field cage are not measured in the TPC because the produced e^+e^- -pairs are pointing out of the TPC volume.

2.2.5 Trigger System

At RHIC the rate of bunch crossings in heavy ion operation is 10 MHz, while the STAR event taping operates at about 100 Hz due to the limited read-out rates of the slow detectors, which are the TPC and SVT. The trigger system [B⁺03e] is designed to make a decision for every bunch crossing using a number of trigger detectors:

Between the TPC and the Barrel Calorimeter is the Central Trigger Barrel (CTB), which has 240 segments, each consisting of a scintillator, light guide and photo-multiplier. The CTB covers ± 1 unit of pseudo-rapidity and is divided into 4 section longitudinally and 60 section azimuthally. It provides information about the overall multiplicity in the central region of the collision, but can also be used for triggers requiring a more complex geometry by making use of the segmentation in η and ϕ .

At a very small angle to the beam line far outside the magnet volume and beyond the first dipole of the RHIC rings two zero degree calorimeters (ZDC) are located. They cover a small solid angle near zero degrees. They are used to measure the energy of spectator neutrons, which are close to beam rapidity and have little transverse momentum. While the CTB returns the highest multiplicity for central collisions, the ZDC measures the highest energy for peripheral collisions. Both detectors together can be used to select different centralities. In addition the difference in the timing signal of both ZDCs can be used to select the position range in z of the main interaction vertex.

The beam-beam-counters (BBC) are two arrays of scintillator detectors around the beam pipe outside of the magnet. They cover a pseudorapidity range of $3 < \eta < 4.1$ and thus do not measure spectators unlike the ZDC. They have been used for triggering central collisions, in which there are few spectators, but many particles produced in the BBC acceptance. The z position of the main interaction vertex can also be selected with the timing signal difference of the two BBCs.

The two electro-magnetic calorimeters (see section 2.2.6) can also be used as trigger detectors. However, only the energy measured in the individual towers is available for

triggering and not the information from the shower-maximum detectors. Events, in which the energy measured in a tower exceeds a certain threshold, can be selected to enhance the sample of events, in which a hard interaction took place, which produce photons or electrons with high transverse momenta.

The exact trigger setup used for analysis in this thesis is discussed in section 5.1.

2.2.6 Outer detectors

There are additional detectors, which should only briefly be mentioned as they are not of central importance to this analysis.

Calorimeters

STAR has a few different calorimeters: An electro-magnetic calorimeter barrel surrounds the TPC [B⁺03b]. It consists of calorimeter towers covering $\Delta\eta = 0.05$ rad and $\Delta\phi = 0.05$ rad each measure the energy. In addition there is shower maximum detector to determine the shower shape. Another disc shaped calorimeter of similar design with shower maximum detector, the endcap calorimeter, is located behind the eastern read-out plane of the TPC. It covers the pseudo-rapidity range of $1 < \eta < 2$ with full azimuthal acceptance [A⁺03j].

The barrel calorimeter measures photons and π^0 -mesons in the same phase space region as the TPC does, but with different systematic uncertainties. The main advantage of the calorimeter is the higher efficiency, which makes it the primary photon and π^0 detector in STAR. The endcap calorimeter can measure photons at higher pseudo-rapidities, but the segmentation of the detector is not fine enough for the high occupancy in heavy ion collisions.

For the RHIC run 4 a shower maximum detector has been added to the zero degree calorimeters. It resolves the spacial distribution of the spectators hitting the ZDC and provides the azimuthal orientation of the collision's impact parameter.

Forward Time Projection Chamber

The forward time projection chambers (FTPC [A⁺03a]) are located at the same radii as the SVT and SSD but outside of the central region of the detector at large distance along the beam line from the interaction point. They use a radial drift field and provide charged particle tracking from ± 2.5 to ± 4 units of pseudo-rapidity. Because the momentum and

energy loss resolution is lower than in the TPC, particle identification is not possible in the FTPC.

Photon Multiplicity Detector

The photon multiplicity detector (PMD [A⁺03i]) is mounted in a plane perpendicular to the beam outside of the magnet. It consists of a charged particle veto layer, a 3-radiation-length photon converter and a pre-shower detector. It measures the position of photons and thus allows to determine their pseudo-rapidity and azimuthal distribution between 2.3 and 3.5 units of pseudo-rapidity. The photon energy cannot be measured.

3 Detecting photons and π^0 -mesons

3.1 Photon interaction processes in matter

For photons there are different ways to interact with matter. The dominant process at lower energies is the photoelectric effect, where the photon is captured by an atom and excites the state of one of the electrons in the shell to a higher energy or ionizes the atom. The next important process is the Compton scattering of the photons off electrons. Starting at an energy of 1022 keV, twice the electron mass, the conversion of the photon to an electron positron pair is possible in the electromagnetic field of a nucleus or an electron. Above a photon energy of 100 MeV this is the dominant process. The cross section for this process saturates at some higher photon energy. In figure 3.1 the different contributions to the total photon interaction probability are displayed versus the momentum of the photon traversing the gas, which fills the STAR TPC.

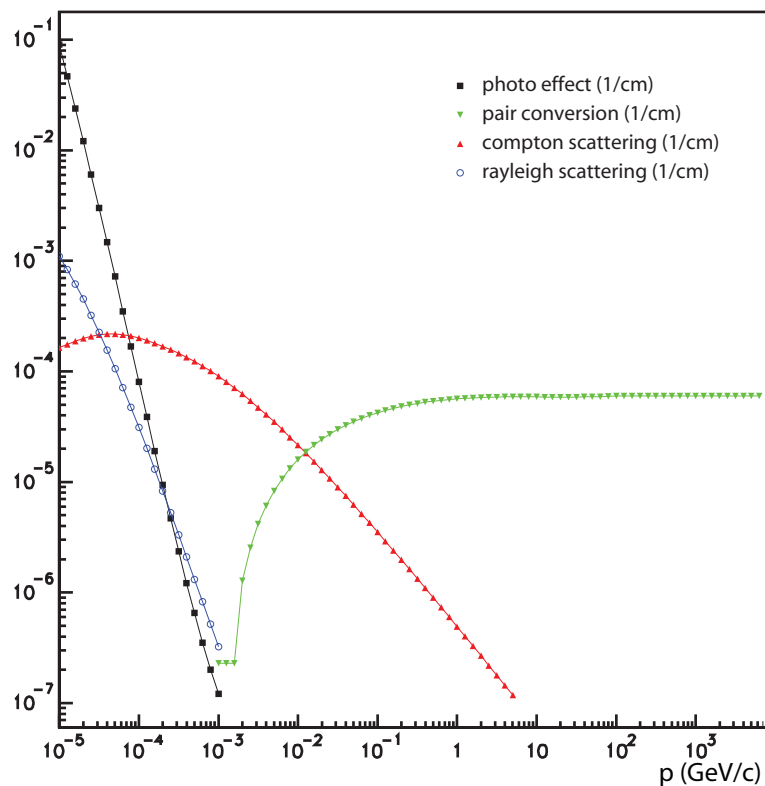


Figure 3.1: Photon interaction probabilities in the TPC gas for different processes versus momentum of the photon [GST, GEA].

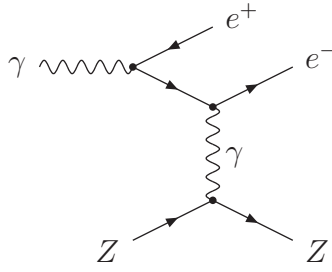


Figure 3.2: Feynman diagram of a photon conversion to an e^+e^- -pair in the electromagnetic field of an electron or a nucleus with the charge Z .

3.2 Photon conversions

Because of energy and momentum conservation a photon cannot decay in the vacuum to an e^+e^- -pair. To balance the equations a part of the momentum has to be transferred away from the electron or positron. As it is shown in figure 3.2, this can happen by exchanging a photon with a charged particle. For a photon traversing detector material this charged particle can be an electron but is most likely to be a nucleus.

3.2.1 Radiation Length

The radiation length X_0 provides information about the photon conversion probability in a specific material. The dependence of the radiation length X_0 on the material traversed by the photon is given by the following formula [H⁺02]:

$$\frac{1}{X_0} = 4\alpha r_e^2 \frac{N_A}{A} (Z^2(L_{rad} - f(Z)) + ZL'_{rad}) \quad (3.1)$$

where $\alpha \approx \frac{1}{137}$ is the fine structure constant, $r_e = 2.818\text{fm}$ the classical electron radius, $N_A = 6.022 \times 10^{23}\text{mol}^{-1}$ the Avogadro number, A the atomic mass and Z the atomic number of the material. The product of the constants $4\alpha r_e^2 N_A$ is equal to $(716.408\text{molcm}^{-2})^{-1}$. The coefficients L_{rad} and L'_{rad} are given in table 3.1. The function $f(Z)$ can be expanded as

$$f(Z) = a^2((1 + a^2)^{-1} + 0.20206 - 0.0369a^2 + 0.0083a^4 - 0.002a^6) \quad (3.2)$$

with $a = \alpha Z$. It should be noted that the radiation length X_0 in equation 3.1 depends

on the square of the atomic number Z .

The dimension of the radiation length is g cm^{-2} . With the density ρ of the material, the mean free path of a photon in this material is $9X_0/7\rho$, if the photon energy is in the region, where the photon conversion probability saturates.

Material	Z	L_{rad}	L'_{rad}
H	1	5.31	6.144
He	2	4.79	5.621
Li	3	4.74	5.805
Be	4	4.71	5.924
Others	> 4	$\ln(184.152Z^{-1/3})$	$\ln(1194Z^{-2/3})$

Table 3.1: Parameters L_{rad} and L'_{rad} .

In the case that different materials are mixed, the radiation length of the compound is

$$\frac{1}{X_0} = \sum_j \frac{w_j}{X_j} \quad (3.3)$$

where w are the weights for the different materials j in by their weight.

Example: The TPC gas

One can use these formulas to calculate the radiation length of the TPC gas, which is composed of 90% Argon and 10% Methane by volume. The temperature in the STAR TPC is regulated to be 75F. The pressure is set to be 2mbar above the ambient air pressure. During the d+Au run 2003 the average pressure was measured to be 1016.59mbar, and is assumed to be the same pressure as in the year 2004 Au+Au run, during which the data used for this thesis were taken. This information allows to calculate the relative densities of the gas components in the TPC as shown in table 3.2.

Using the calculated radiation length of the TPC gas in table 3.3 and its density the mean free path of a high energy photon is 16728.1 cm. This is consistent to better than a permille with the number 16723,3 cm obtained from the STAR simulation software, where the photon mean free path saturates above 100 GeV/ c photon energy.

Material	density (g/cm^3)	density in mixture (g/cm^3)
Argon	0.0016387	0.0014748
Methan	0.000658	0.0000658
Carbon		0.0000492
Hydrogen		0.00000165
TPC gas	0.00154065	

Table 3.2: Density of the different components of the gas mixture in the TPC. The central column is the density of the pure gas at the given temperature and pressure, the right one the density contribution to the TPC gas mixture.

Material	Z	A	$X_0(g/cm^2)$
Argon	18	39.948	19.549
Carbon	6	10.0107	42.6969
Hydrogen	1	1.00794	63.0435
TPC gas			20.0449

Table 3.3: Charge and mass of the nuclei in the TPC gas mixture. Also given is the resulting radiation length X_0 .

3.3 Photon measurement techniques

As the dominant interaction process at higher energies is pair conversion, this mechanism is used to detect photons in high energy physics. Electromagnetic calorimeters are made of a material with a high nuclear charge to maximize the conversion probability. Photons convert in the calorimeter and the resulting electrons and positrons will produce new photons mainly by Bremsstrahlung processes in subsequent interactions and produce an electro-magnetic shower in the detector. Often scintillators are used to detect these shower particles: They absorb these particles, which are still at relatively high energies, and subsequently emit photons with longer wavelengths close to or in the visible spectrum. The resulting low energy photons are collected in photo-multipliers and the measured energy allows to determine the full energy of the shower and thus the original photon.

Another way to measure the photon is to use only a small amount of conversion material to avoid subsequent interactions of the produced electron positron pair. Charged particle tracking detectors can measure the momenta of the two conversion daughters, from which energy and momentum of the photon can be reconstructed.

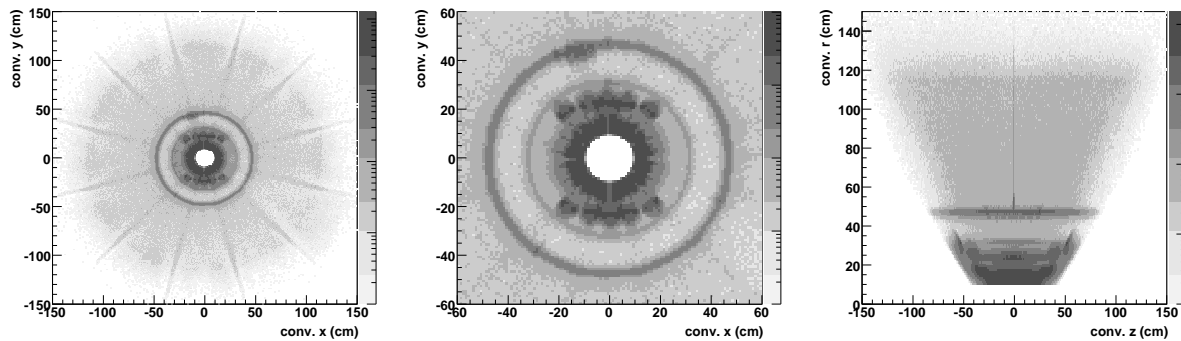


Figure 3.3: Distribution of conversion vertices in the xy-plane (left) and the rz-plane (right).

3.4 Reconstruction of photon conversions

The distribution of photon conversion points in space reflects in various ways the distribution of material in the experimental setup. This can be seen for the STAR experimental setup in particular in figure 3.3 in the middle plot, showing the distribution of reconstructed conversion points in the inner region of the experiment. Visible are the SVT, the ten individual ladders of the SSD and the inner field cage. The twelve-fold structure on the left side is a reconstruction effect caused by the sector structure of the TPC read out. The typical topology of a photon conversion is shown in figures 3.4 and 3.5. It is a pair of tracks with a small opening angle at a common vertex, which is different from the main event vertex. To find possible conversion vertices, the following selection criteria are used.

3.4.1 The STAR track model

To understand some of the cuts and how the conversion reconstruction works, it is useful to know about the STAR track model: In it a track is parameterized by a helix. This corresponds to a circular trajectory if projected into the xy-plane. For a path of the length s along the trajectory of the helix in three-dimensional space the change of the z-coordinate is proportional to s . The dip angle of helix is defined as $\sin(\text{dip}) = dz/ds$. This model assumes a particle traversing a perfectly homogenous magnetic field in the vacuum. The magnetic field in STAR is homogenous to about 1% and the average energy loss of electrons in the detector material is about 2%, which gives only small deviations from the helix track model.

3.4.2 Selection of e^+ - and e^- -track candidates

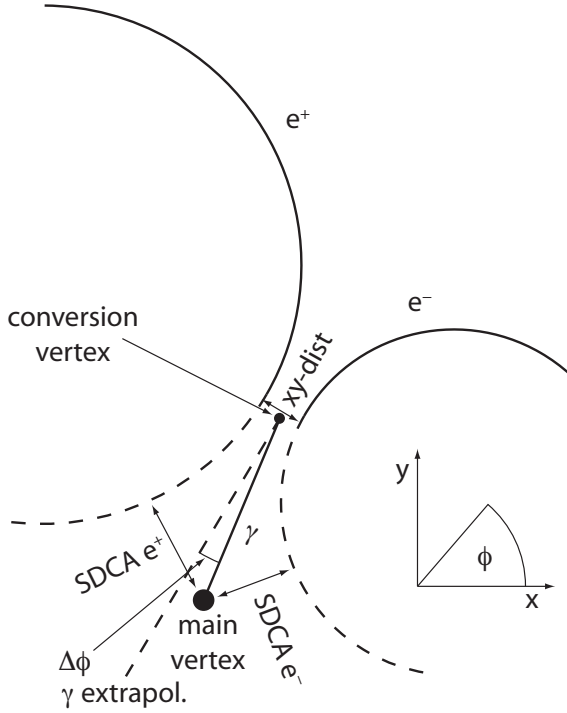


Figure 3.4: Schematic display of cut parameters in the xy-plane.

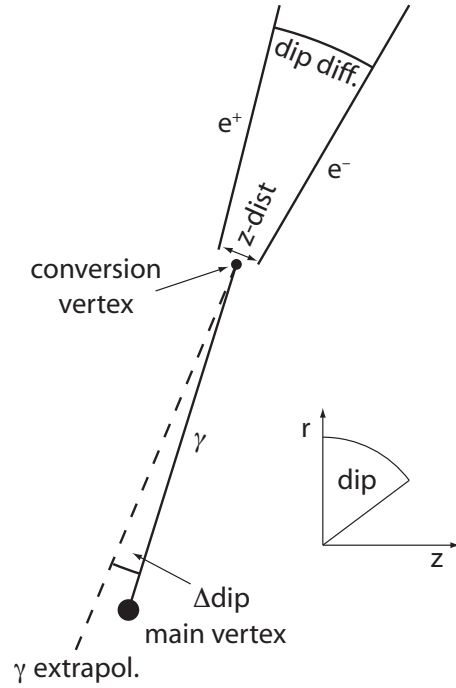


Figure 3.5: Schematic display of cut parameters in the rz-plane.

In the first step of the conversion finding electron- and positron-track candidates are selected which may have their origin in a photon conversion. As shown in figures 3.4 and 3.5 the daughter tracks of the conversion come from a secondary vertex and therefore do not point back to the main event vertex. Therefore the signed distance of closest approach (SDCA) is required to be positive. The SDCA is defined as the distance between the main event vertex and the center of the circle parameterising the projection of the helix into the xy-plane minus the radius of that circle. It is illustrated in figure 3.4, where both tracks have a positive SDCA. For tracks with a large transverse momentum, however, this cut is not useful, because the SDCA of the track becomes smaller than the pointing resolution of the detector. Therefore this cut is only applied for particles with a transverse momentum below $300 \text{ MeV}/c$. Figure 3.6 shows the SDCA distributions for tracks from reconstructed conversions below $300 \text{ MeV}/c$, for which the cut will be applied and for tracks in the transverse momentum region of $0.8 - 1 \text{ GeV}/c$. For particles originating from the main event vertex this distribution has to peak at zero.

Because photons convert to electron-positron-pairs, a dE/dx cut is used to select positrons and electrons. It requires the dE/dx value to be no more than 2 standard deviations below and 4 standard deviations above the mean specific energy loss of electrons and

positrons at the given momentum. The shape of the dE/dx distribution versus momentum of the track originating from a photon conversion is shown in figure 3.7.

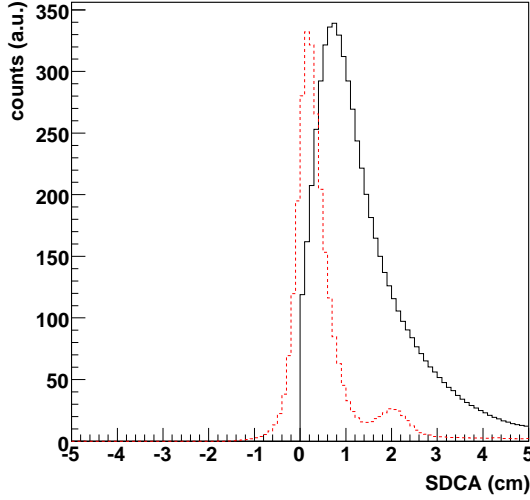


Figure 3.6: Distribution of the signed distance of closest approach to the main event vertex of tracks from conversions. The black solid line is the distribution for tracks below $300 \text{ MeV}/c$ transverse momentum, where the SDCA is required to be positive and the red dashed line is for tracks in the range $0.8\text{--}1 \text{ GeV}/c$. The second peak in the red dashed distribution at 2 is caused by the conversions in the inner field cage of the TPC.

There are more standard quality cuts applied, which require a minimum number of 12 hits in the TPC and a ratio of the found hits to the maximum possible hits for a track of more than 55% to avoid double counting of split tracks. The radius of the track curvature in the magnetic field is required to be at least 15 cm.

3.4.3 Selection of photon conversions

In the next step photon conversion candidates are found by selecting pairs of electron- and positron-track-candidates, which exhibit the topology of a photon conversion.

The conversion vertex is found by projecting both electron and positron tracks into the xy -plane, where they are circles. If the centers of the two circles are \vec{x}_a and \vec{x}_b and their radii r_a and r_b then the position of the conversion vertex \vec{x}_c is defined as $\vec{x}_c = (\vec{x}_a r_b + \vec{x}_b r_a) / (r_a + r_b)$. This is always on the line connecting the two centers. If the distance of the centers is larger than the sum of the radii, this is in between the circles and otherwise in their overlap zone. The z coordinate of the conversion point is found

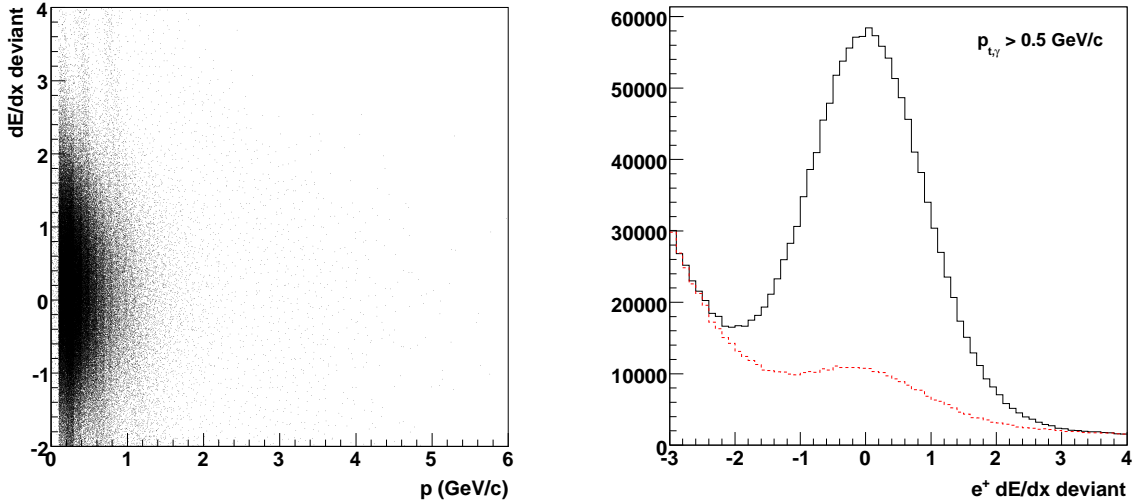


Figure 3.7: The distribution of the specific energy loss in the TPC gas of originating from reconstructed photon conversions normalized by the specific energy loss calculated using the Bethe-Bloch-parametrisation for electrons is shown on the left side. The vertical bands visible below 1 GeV/c momentum are the contamination of the sample by charged π^- , K -mesons and protons. On the right side a projection of the whole distribution on the y-axis is shown for electron candidates from photon candidates from data (black solid line) and electron candidates from photon candidates from mixed events (red dashed line).

by averaging the z coordinates of the two points on the tracks which are closest to the defined conversion point in the xy -plane.

The energy of the photon candidate is calculated by adding the energies of the two daughter tracks. The energies of the two tracks are calculated from their momenta assuming they are electrons and positrons. The dip-angle component of the reconstructed momentum vector is the average between the dip-angles of the two track helices. The azimuthal component is perpendicular to the line connecting the two helix centers in the xy -plane.

The selection criteria for photons are illustrated in figures 3.4 and 3.5 and the cut off values are summarized in table 3.4. The following cuts are applied to the photon conversion candidates:

The conversion vertex is required to be inside the cylindrical volume defined by the TPC outer field cage ($r < 200\text{cm}$) and the readout planes ($|z| < 200\text{cm}$). Because there is an uncertainty in the material in the SVT and SSD, conversions in the regions of the

	cut variable	good range
e^+/e^-	SDCA	> 0 or < -4 for $p_t < 0.3 \text{ GeV}/c$
	dE/dx deviant	> -2 and < 4
	number of hits	≥ 12
	hits / possible hits	≥ 0.55
	track radius	$> 15 \text{ cm}$
	flag	≥ 1
photon	abs(conversion position z)	$< 200 \text{ cm}$
	conversion position r	> 10 and $< 200 \text{ cm}$
	abs(xy-dist)	$< 1.5 \text{ cm}$
	abs(z-dist)	$< 1 \text{ cm}$
	$\Delta \text{ dip}$	$< 0.035 \text{ rad}$
	$\Delta\phi$	$< 0.05 \text{ rad}$
	dip difference	$< 0.03 \text{ rad}$
	invariant mass	$< 100 \text{ MeV}/c^2$
	with only dip component of opening angle	$< 12 \text{ MeV}/c^2$
	conversion position r	abs(conversion position z)
photon	$< 20 \text{ cm}$	$< 22 \text{ cm}$
	> 20 and $< 40 \text{ cm}$	$< 40 \text{ cm}$

Table 3.4: Cuts used to select photon conversions are given in the upper table. Δdip and $\Delta\phi$ are the angles between the momentum reconstructed from the topology and the vector pointing from the event vertex to the conversion vertex. For an explanation of the cut parameters also look at figures 3.4 and 3.5. The lower table lists the regions, where reconstructed photon conversions are rejected due to the uncertainty in the geometry description.

support structures of both detectors are cut out. The precise regions cut out are given in the lower part of table 3.4. A more detailed discussion on this issue is given in section 4.2.

To reduce the amount of combinatorial background, vertices in a cylindrical region around the beam line ($r < 10\text{cm}$) are rejected, where the track density is very high. At the conversion vertex the maximum distance of the two tracks in the xy-plane (xy-dist) is limited to 1.5 cm and to 1 cm in the z direction (z-dist). The distribution of both distances are shown in figure 3.8.

Because all photons of interest for this thesis come from the main event vertex, the photon candidate is required to point back to the main vertex. This is ensured by

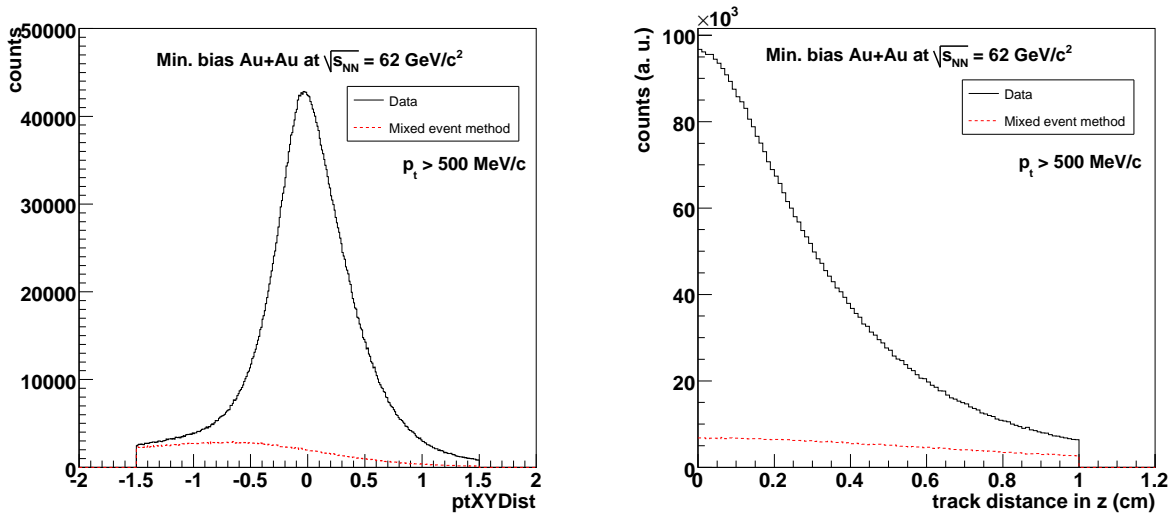


Figure 3.8: The distance of the two circles representing the e^+ - and e^- -tracks from a photon conversion candidate in the xy-plane are shown on the left side. If the distance is negative, both circles intersect. The distribution is asymmetric because most charged tracks in an event originate from the main vertex. If two of these tracks have a second point, where they approach close enough to be accepted, then the circles must have a negative distance in the xy-plane. On the right side the distance of the two tracks in z at the calculated conversion vertex is shown. On both plots the distributions for photon candidates from data as well as the combinatorial background determined by a mixed event method described in section 3.4.4 are shown.

applying two cuts on the angle between the momentum vector of the photon candidate and the vector pointing from the main vertex to the conversion vertex of the photon. The two cuts require the angle in the xy-plane, $\Delta\phi$, to be smaller than 0.05 rad and the angle in the rz-plane, Δdip , to be smaller than 0.035 rad. The distributions of both angles are shown in figure 3.9.

One of the characteristics of photon conversions is the small opening angle and invariant mass of the electron-positron-pair. Therefore a cut on the dip angle difference, dip diff. or α_{dip} , between the two daughter tracks to be smaller than 0.03 is applied. In addition the invariant mass $M_{inv,dip} = (E_1 + E_2)^2 - (p_1^2 + p_2^2 + 2p_1p_2 \cos(\alpha_{dip}))$ calculated from α_{dip} and the track momenta is required to be smaller than $12 \text{ MeV}/c^2$. If the two circles, representing the projections of the tracks into the xy-plane, intersect, there is also a well defined opening angle at the crossing point in the xy-plane, α_{xy} . In this case an additional cut on the invariant mass calculated using both opening angle components, $M_{inv} = (E_1 + E_2)^2 - (p_1^2 + p_2^2 + 2p_1p_2 \cos(\alpha_{dip}) \times \cos(\alpha_{xy}))$, is applied. It is a less restrictive cut, because the opening angle resolution in the xy-plane is much worse than for the dip

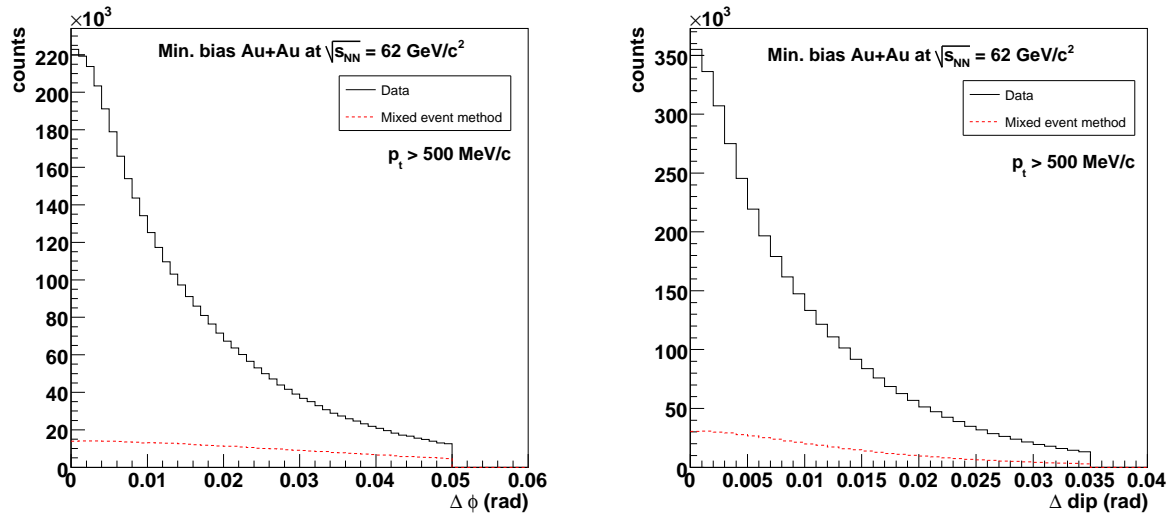


Figure 3.9: $\Delta\phi$ (left) and Δdip (right) are the two angles between the momentum of the photon candidate and the vector pointing from the reconstructed conversion vertex to the main event vertex in the xy -plane and the rz -plane respectively. On both plots the distributions for photon candidates from data as well as the combinatorial background determined by a mixed event method described in section 3.4.4 are shown.

angle difference. The distribution of the angle difference and the invariant masses are shown in figures 3.10 and 3.11.

3.4.4 Treatment of the combinatorial background

Due to the high particle multiplicities in heavy ion collisions, there is a significant probability that two random tracks satisfy all the cuts for the conversion reconstruction, although they do not originate from a photon conversion. To study the contribution to the photon spectra by this combinatorial background, a mixed event technique was used. After the photon reconstruction the azimuthal angle of all electron candidate tracks was rotated by π while the positron candidate tracks were left unchanged and the photon finding algorithm was run again. This way two tracks ending up close to each other were clearly separated in the original event and therefore cannot originate from the same photon conversion.

The mixed event spectra are reconstructed from the identical event sample that was used for the reconstruction of the photon spectra. The comparison of the invariant mass distribution of photon candidates in the combinatorial background from mixed events

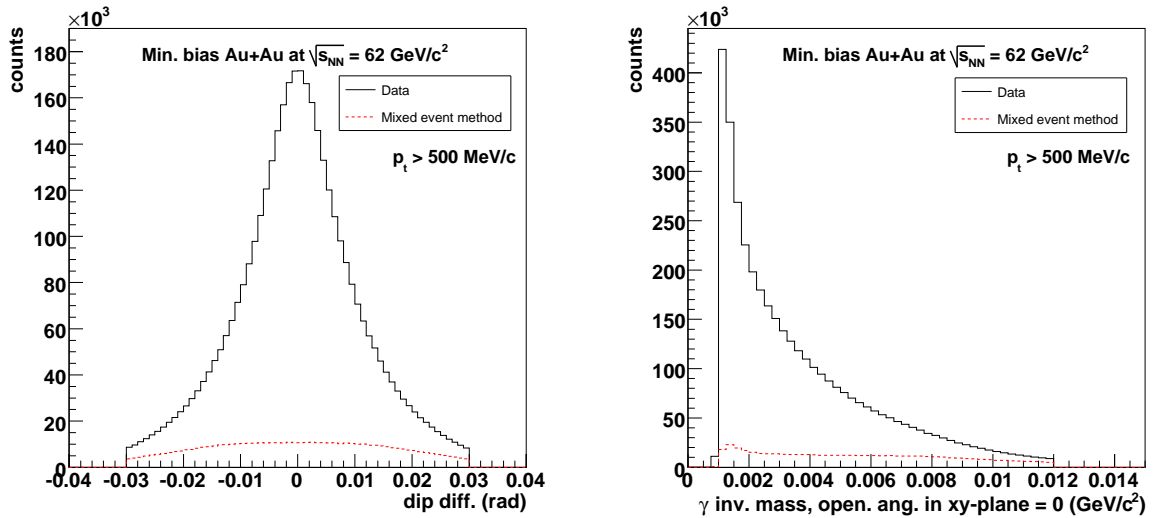


Figure 3.10: The distribution of the dip-angle difference of the two tracks originating from a conversion candidate is shown on the left side. On the right side the invariant mass of electron-positron-pairs from photon conversion candidates calculated using only this component of the opening angle and assuming that the opening angle in the xy -plane is zero is presented. On both plots the distributions for photon candidates from data as well as the combinatorial background determined by a mixed event method described in section 3.4.4 are shown.

(red dashed histogram) to the signal in real data (black solid histogram) is shown in figure 3.12 on the left side for minimum bias Au+Au-collisions. The enhancement of the data over the mixed events at low invariant mass is clearly visible, while at higher masses both of them are in good agreement. Therefore no additional scaling factor is applied to normalize the mixed event spectra to the data. The plot in figure 3.12 on the right side shows the ratio of the combinatorial background from mixed events to real data versus transverse momentum for four different centralities (for a definition of the centralities see section 5.1). In the most central bin, where the multiplicities of produced particles are the highest, the contamination of the combinatorial background reaches up to about 35% of the total reconstructed photon spectra at about 1.5 GeV/c transverse momentum. To remove the combinatorial background from the photon spectra, the mixed event spectra were subtracted.

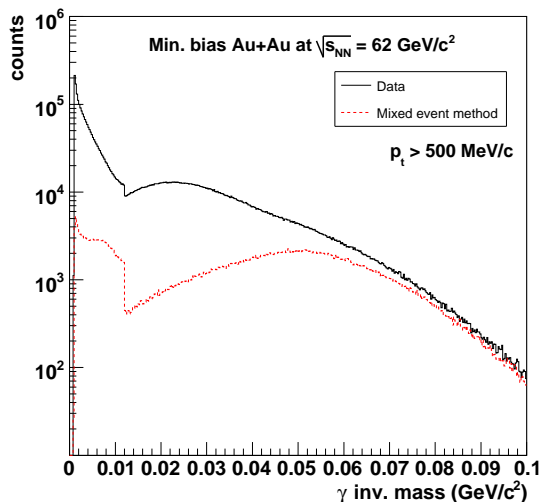


Figure 3.11: Invariant mass distribution of electron-positron-pairs from reconstructed photon conversion candidates. The distribution is composed of two parts. If the two tracks do not intersect in the xy -plane, the opening angle is solely given by the dip-angle difference of the tracks and the distribution looks like the one in figure 3.10 on the right side. If the tracks intersect in the xy -plane, the opening angle is larger and causes the part of the invariant mass distribution above $12 \text{ MeV}/c$.

3.4.5 Overall effect of the cuts on signal and background

All the cuts are applied to reduce the amount of combinatorial background without reducing the signal too much. The cuts can be divided in two classes: The first class are the cuts used to select tracks based on quality criteria and dE/dx , which are all track cuts listed in table 3.4 except for the SDCA cut. All photon cuts and the track SDCA cut form the second class of cuts, which specifically select the topological properties of a photon conversion.

To study the background suppression by the topological cuts, a set of 600 events is analyzed using the mixed event method described in section 3.4.4 with all topological cuts switched off. The accepted yield after the non-topological cuts is then compared to the yield after all cuts in the full data set using the same mixed event method. Both distributions are divided by the number of event used for each. The ratio of the distribution after all cuts to the one after only the non-topological cuts is shown in figure 3.13 on the left side for minimum bias Au+Au collisions at $\sqrt{s_{NN}} = 62 \text{ GeV}$. This plot shows that the background is suppressed by a factor of more than 10^4 for transverse momenta below $1 \text{ GeV}/c$ and up to 10^6 above $4 \text{ GeV}/c$.

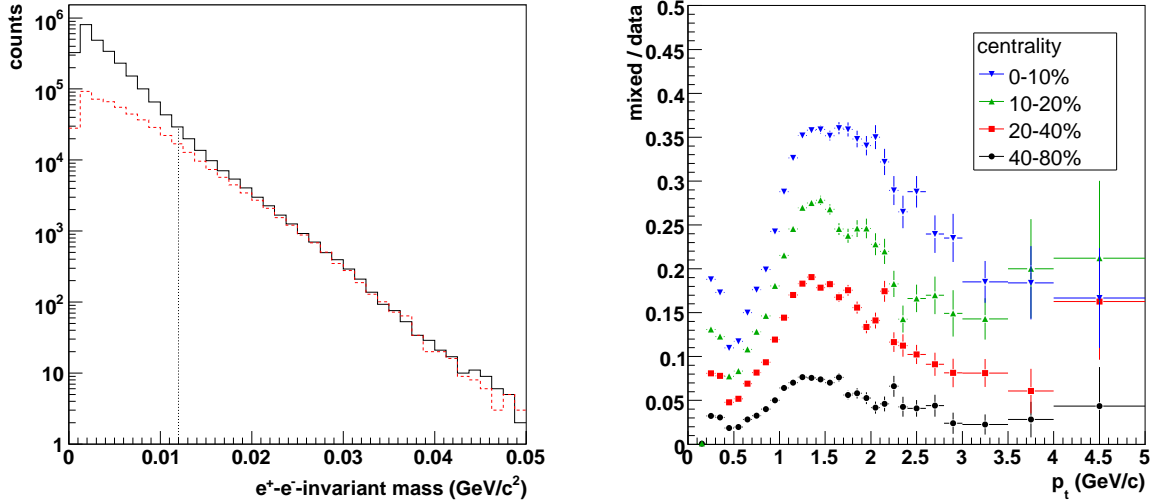


Figure 3.12: On the left side the invariant mass spectrum of e^+e^- -pairs assuming that the opening angle in the xy-plane is zero is shown. The black solid histogram is from normal data, the red dashed one from mixed events, in which all negative electron candidates have been rotated by π . The black dotted line illustrates the cut value on this invariant mass at 12 MeV/c². On the right is the ratio of the combinatorial background from the mixed event method to the signal from real data versus transverse momentum. This is shown for four different centralities (for definition see section 5.1).

The amount of real photons cut out is estimated using a set of simulated events using a Monte Carlo method. The method is described more in detail in chapter 4. This signal efficiency of the topological cuts versus transverse momentum is shown in figure 3.13. This is the ratio of the photons surviving all cuts to all photons surviving the non-topological cuts. Above 1 GeV/c half of the signal is cut away independently of the transverse momentum. Below 1 GeV/c a larger fraction of the signal is lost.

It should be mentioned that the simulated event set does not include a proper simulation of the dE/dx and therefore this cut is not applied on the simulated events. This issue is explained in more detail in chapter 4.5.

3.5 Reconstruction of the π^0 -meson yield

The main decay channel of the π^0 -meson is $\pi^0 \rightarrow 2\gamma$ (see figure 3.14) with a branching ratio of 98.798% and a mean life time of $\tau = 8.4 \pm 0.6 \cdot 10^{-17}$ s [H⁺02]. Because of this very

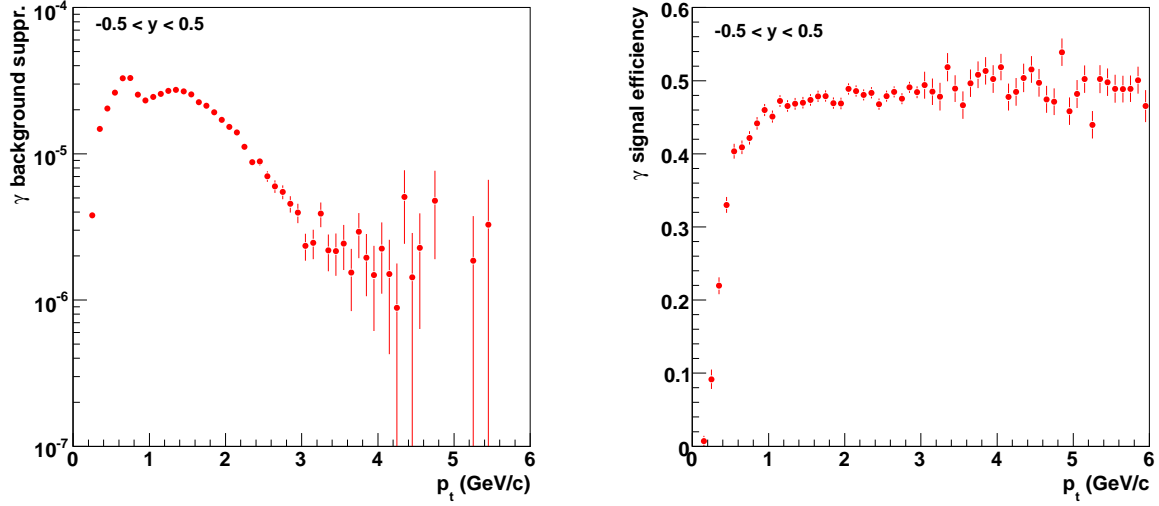


Figure 3.13: Background suppression (left) and signal efficiency (right) of the topological cuts versus transverse momentum in minimum bias Au+Au-collisions at $\sqrt{s_{\text{NN}}} = 62$ GeV.

short life time the π^0 -meson travels only a very short distance before decaying. Therefore the reconstruction of a secondary π^0 -vertex and thus a topological identification is not possible with the STAR experiment and the decay products can safely be assumed to come from the main event vertex. The photon measurement technique, as explained in the previous section, is designed to measure photons coming from the main event vertex. The π^0 -yield can then be extracted by plotting the invariant mass distribution of pairs of these photons, which is shown in figure 3.15. The peak at $135 \text{ MeV}/c^2$, the invariant mass of the π^0 , is clearly visible.

The contribution of the combinatorial background has been studied using a mixed event technique: In addition to the spectra of the two-photon invariant mass, the spectra of the invariant mass of the same two-photon-pairs have been created after one of the photons has been rotated by π in azimuth. The mixed event background is normalized in the invariant mass region from 200 to $700 \text{ MeV}/c^2$. In figure 3.15 on the left side the mixed event spectrum (black crosses) is compared to the spectrum from real data (red squares). Where the normal invariant mass spectra show the peak at the π^0 -mass, the mixed event spectra just show a smooth continuation of the shape of the combinatorial background from below to above the region of the peak. Figure 3.15 on the right side shows the invariant mass spectrum after subtraction of the mixed event background. Three methods were tested to extract the π^0 -yield in transverse momentum bins:

1. Integration of the invariant mass histograms

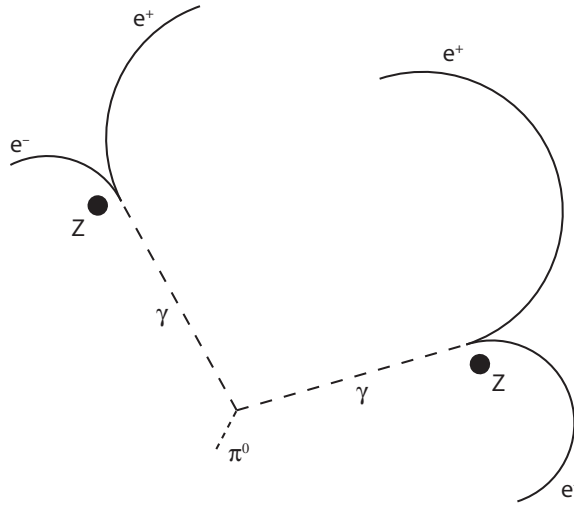


Figure 3.14: Schematic display of a π^0 -meson decaying into two photons, which both convert and thus produce a total of 4 charged particle tracks. In reality the path length of the π^0 -meson is much shorter than indicated here due to the very short life time.

2. Fit by a gaussian plus a polynomial
3. Fit by the peak shape from simulation plus a polynomial

For the first method the mixed event background is subtracted from the invariant mass spectra and the number of entries in the peak region of the histogram is counted. The signal is integrated from 100 to 170 MeV/c^2 . To take into account the finite amount of remaining combinatorial background, the subtracted spectra are also integrated from 65 to 100 MeV/c^2 and from 170 to 205 MeV/c^2 and the result of these two integrations is subtracted from the one in the peak region. This affects the measured π^0 -yield by up to 10%. The statistical uncertainty is calculated from the statistical errors of the bins in the invariant mass histogram.

For the second method the invariant mass spectra are fit with a gaussian for the peak plus a polynomial for the combinatorial background. The free parameters of the gaussian are the mean, the width and the integral. A second order polynomial is used for background fits up to 1.5 GeV/c transverse momentum, above that a linear fit. Above 2.6 GeV/c the peak position and width are fixed to 133 MeV/c^2 and 8 MeV/c^2 respectively. These restrictions at high transverse momenta are necessary because the limited statistics is not sufficient to constrain a fit with a large number of free parameters. For lower transverse momenta, the fitted values for mass and width are shown in figure 3.17. An example for a fit is shown in figure 3.16 for the transverse momentum range from 1.2 to 1.3 GeV/c . MINUIT, which is available in the TMinuit class in the ROOT analysis framework

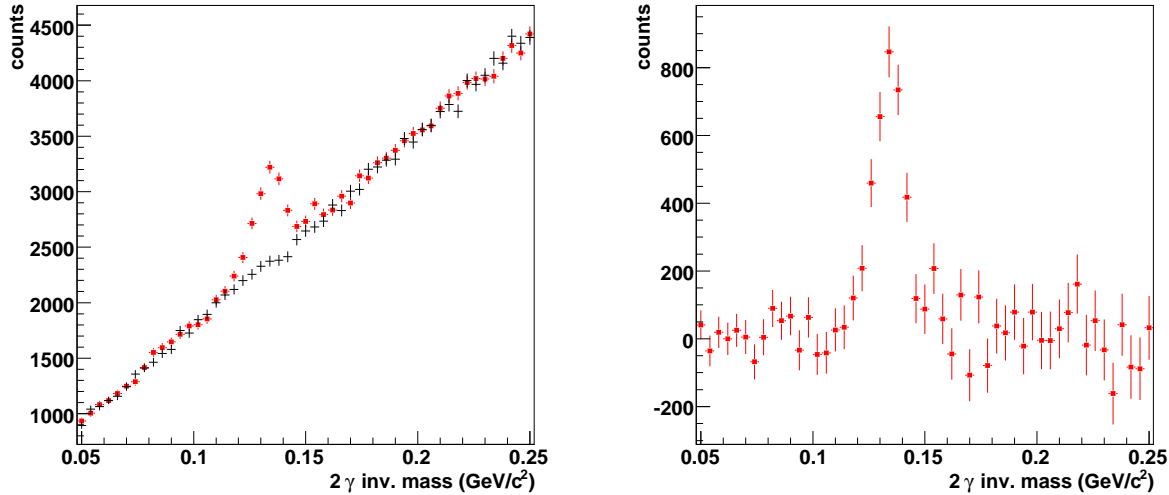


Figure 3.15: On the left side the invariant mass distribution of 2-photon-pairs in minimum bias Au+Au-collisions at $\sqrt{s_{NN}} = 62$ GeV is shown (red squares). A clear peak at the π^0 -mass of 135 MeV/c² is visible. The mixed event spectrum (black crosses) is shown for comparison and matches the distribution nicely outside the region of the peak. After subtraction of the mixed event spectrum, the invariant mass spectrum is flat in the region around the π^0 -peak (right side).

[ROO], was used as the fitting routine with the MIGRAD algorithm as minimizer and χ^2 minimization. The uncertainties on the fitted parameters reported by this fitting algorithm were used as statistical errors.

For the third method the shape of the peak is determined by the distribution of reconstructed π^0 -masses from simulated π^0 -mesons. The peak shape is determined separately for each transverse momentum bin. The invariant mass histogram is then fit by the peak taken from simulation times a factor as the free parameter plus a polynomial background of the same order as used in the second method. The statistical errors are taken from the fitting routine, which was the same as used for the second method. Figure 3.16 also shows a fit using this method.

The comparison of the yields versus transverse momentum extracted using the three methods is shown in figure 3.18. The results differ by up to 10%, which is an estimate of the systematic error on the π^0 -spectra due to the procedures used for the extraction of the π^0 -yield.

The statistical uncertainties for the second and third method are of similar size, while the errors of the first method are the largest. The second method needs a reduction

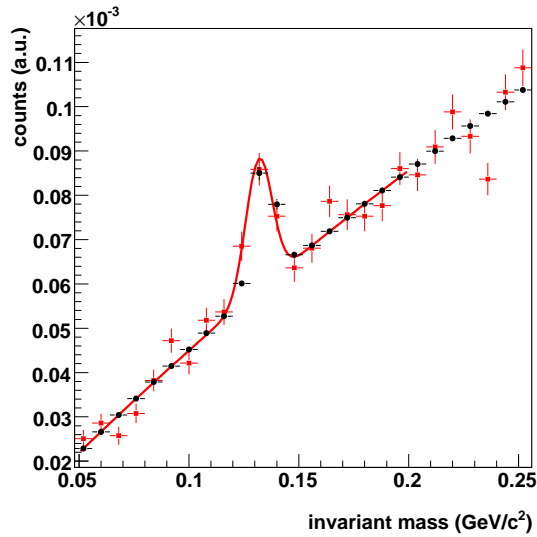


Figure 3.16: The invariant mass spectrum in minimum bias Au+Au-collisions at $\sqrt{s_{\text{NN}}} = 62$ GeV with a transverse momentum in the range of $1.2 - 1.3$ GeV/ c is shown (red squares). The line is a gaussian fit plus polynomial background. The black circles show the fit by the peak shape from simulation plus a polynomial background.

of free parameters at high transverse momenta, because of the limited statistics. The third method suffers from the low reconstruction efficiency of π^0 -mesons at low transverse momenta. This results in a larger uncertainty on the peak shape. Therefore the preferred method is the third one at high and the second at low transverse momenta. All π^0 -spectra in this thesis are a combination of spectra obtained using methods 2 and 3. Below 1.6 GeV/ c method 2 and above method 3 was used.

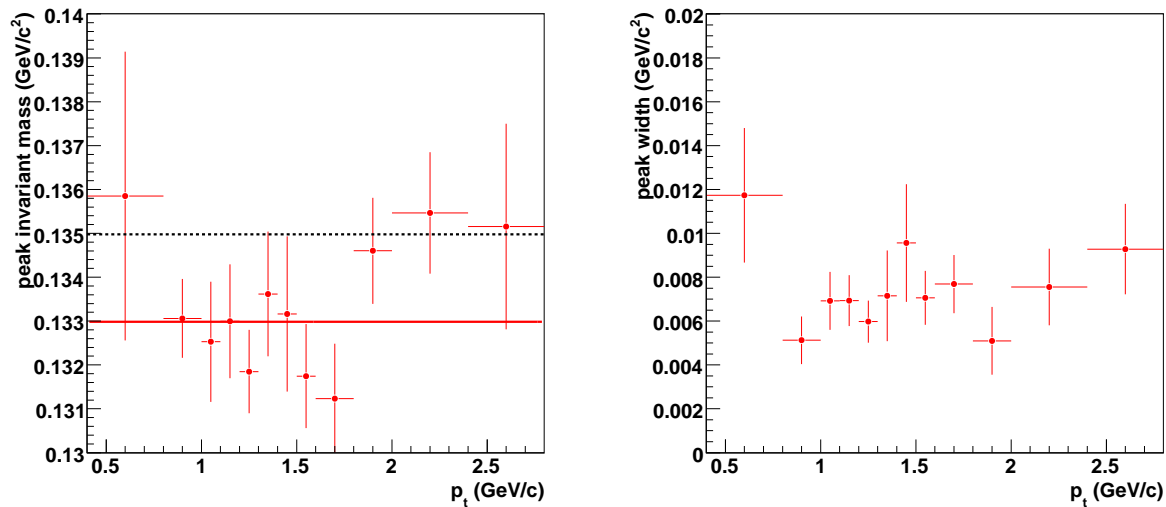


Figure 3.17: The fitted invariant mass of the π^0 -peak is shown on the left side. The red solid line is a constant fit to the masses over all transverse momentum bins and is $133 \text{ MeV}/c^2$. This is about $2 \text{ MeV}/c^2$ below the π^0 -mass, which is indicated by the black dashed line. The plot on the right side shows the width of the peak, when fitted by a gaussian. Both plots are for minimum bias Au+Au-collisions at $\sqrt{s_{\text{NN}}} = 62 \text{ GeV}$.

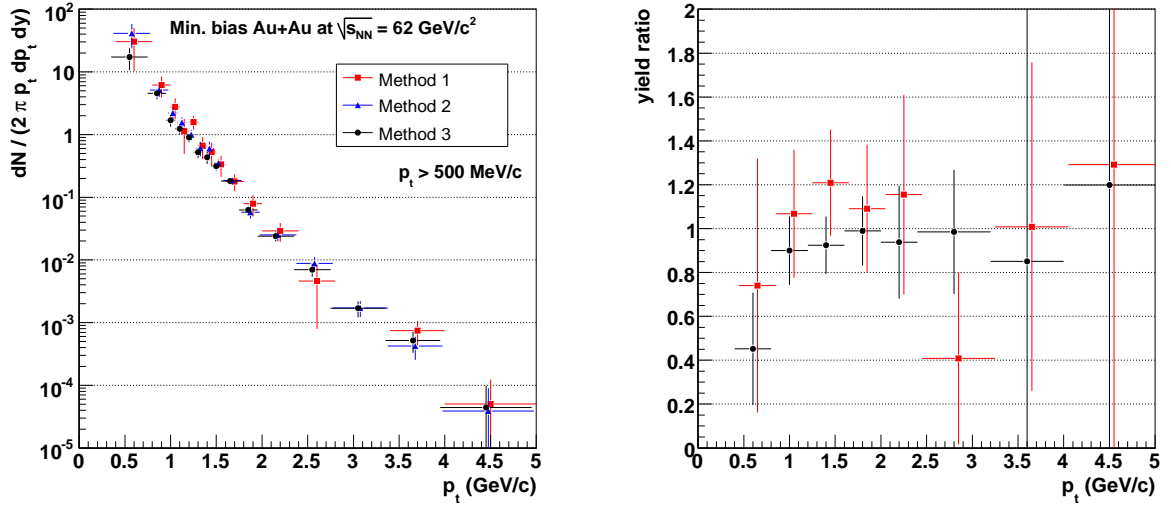


Figure 3.18: Results from the three different methods used to extract the yield from the invariant mass histograms are shown on the left side: Integrating the invariant mass histograms after background subtraction (red squares), fitting the histograms by a gaussian plus polynomial background (blue triangles) and fitting the histograms by a peak shape from simulation plus polynomial background (black circles). For better comparisons the first and the third method results are divided by the second method results and are shown on the right side (same color coding). Within statistical errors they are in agreement, but there appears to be a systematic difference of up to 10%. The plots show data from minimum bias Au+Au-collisions at $\sqrt{s_{NN}} = 62$ GeV.

4 Efficiency and acceptance correction

The analysis procedure described in chapter 3 provides distributions of photons and π^0 -mesons in phase space, which are subject to inefficiencies and acceptance losses. To deduce the true number of photons and π^0 -mesons produced, the corresponding losses have to be calculated. This is the subject of this chapter.

4.1 The photon- and π^0 -embedding process

Corrections for the limited acceptance and detection efficiency were determined using multi step Monte Carlo method: In the first step the main vertex position of a real data event is taken. At this position photons or π^0 -mesons and their decay products are created and tracked through the detector material using *STAF*, a *GEANT* based detector simulator for STAR [GST, GEA]. While a photon is tracked, its conversion probability in the traversed material is calculated and it can convert accordingly. The daughter particles are tracked as well including the possible effects of the detector material on them.

In a second step the effect of the tracked particles on the detectors is simulated. For the TPC the energy loss and ionization in the TPC gas along the trajectories of charged particles and the drift of the free electrons to the readout plane are simulated using a detector response simulator. The electronic signals produced in the readout planes are then added to the real event. The resulting composite event is reconstructed.

In this process coordinates, where the tracks ionized the gas, are stored. They are referred to as Monte Carlo hits.

The reconstructed tracks are matched to the Monte Carlo tracks using the *StAssociationMaker*. The matching algorithms are based on hits: Monte Carlo hits are created at the positions, where the Monte Carlo tracks ionize the TPC gas. From the electronic read out signals hits are reconstructed, which then correspond to a Monte Carlo hit or an ionization in real data. There are two different algorithms to match reconstructed hits to Monte Carlo hits: One is based on the spacial proximity of both hits, the other one uses labels. These labels indicate for each reconstructed hit, which Monte Carlo hit contributed to to the read out signals it was reconstructed from. To match a reconstructed track to a Monte Carlo track at least 75% of the hits on the reconstructed track are required to be common hits with the Monte Carlo track. A reconstructed photon conversion is matched to a Monte Carlo photon conversion if both reconstructed daughter tracks are matched to both Monte Carlo daughter tracks coming from the conversion. A π^0 -meson is matched if both daughter photons are matched.

The track and photon cuts used in the standard analysis are applied to all reconstructed photons, which are matched to simulated photons. An exception is the dE/dx -cut as explained in 4.5. The detection efficiency for a photon is then the number of reconstructed

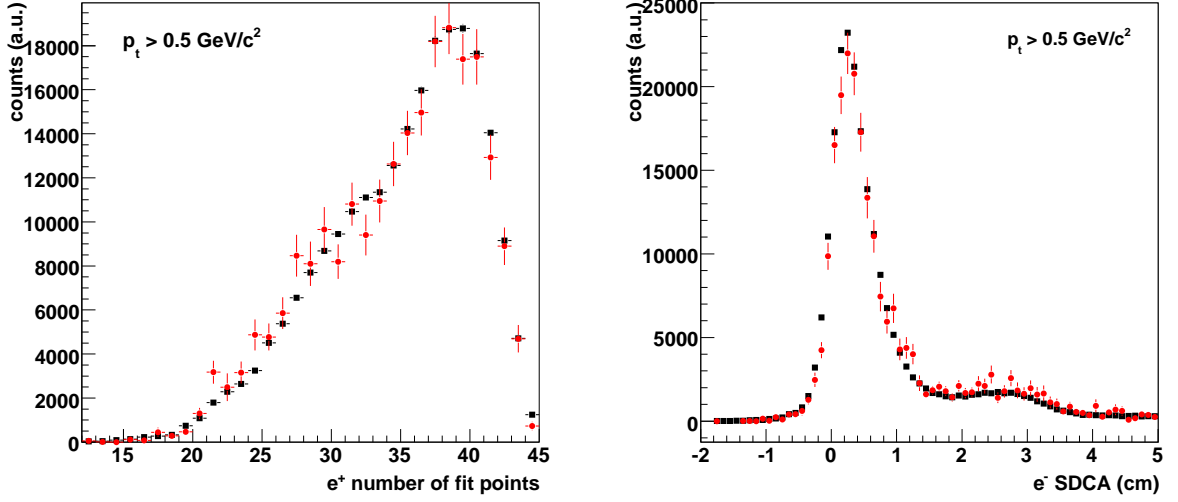


Figure 4.1: On the left side the distribution of the number of fit points on a track reconstructed as a positron daughter of a conversion in minimum bias Au+Au-collisions at $\sqrt{s_{NN}} = 62$ GeV is shown by the black squares. The red circles show the same distribution for reconstructed tracks, which were associated to a simulated positron daughter from a conversion. On the right side the comparison for the signed distance of closest approach to the main vertex for electrons from the same photons is shown.

photons, which are matched to simulated photons and satisfy the cuts, divided by the number of simulated photons:

$$\text{eff}_{\text{det}}(y, p_t) = \frac{n_{\text{det}}(y, p_t)}{n_{\text{mc}}(y, p_t)} \quad (4.1)$$

The conversion probability of a photon traversing the STAR detector before leaving the TPC is only of the order of 5 – 10%. This results in the probability of both photons coming from a π^0 -decay to convert to be of the order of 0.25 – 1%. Because a non-converted photon cannot be reconstructed, it is possible to factorize the photon detection efficiency into a conversion probability and a reconstruction efficiency. The same is true for the π^0 efficiency because as soon as one daughter photon does not convert, the reconstruction of the π^0 is impossible. While non-converted photons do not add to charged particle multiplicity in the TPC, π^0 -mesons with one converted daughter photon do so. Because they are about 20 – 40 times more abundant than the π^0 -mesons with both daughter photons converted, they result in 10 – 20 times more charged tracks. Because the reconstruction of an event takes much more computing resources than the simulation in STAF, simulated particles, which cannot be fully reconstructed, should

not be processed by the event reconstruction. This is accomplished by a filter applied on the STAF level, which passes only converted photons or π^0 -mesons with both daughter photons converted on to the event reconstruction. The filter also stops all tracking if the photon reaches the outer walls of the TPC. The phase space distributions of all particles simulated and all particles passing the filter are used to calculate the conversion probability of photons and π^0 -mesons as function of rapidity and transverse momentum. The reconstructed events, containing only information about particles passing the filter, are used to determine the reconstruction efficiency of converted photons and π^0 -mesons with both daughters converted.

4.1.1 Number and distribution of embedded particles

Because the reconstruction efficiency of a single track depends on the track multiplicity in the event, the number of embedded tracks per event should be limited. One simulated π^0 -meson was embedded in every real event plus one for each 80 tracks reconstructed in an event. The same was done for photons by embedding one photon plus one for each 40 tracks in the event. This way the contribution of charged Monte Carlo tracks to the event is kept below 10% for events with more than 80 tracks for π^0 embedding and 40 tracks for photon embedding. The shape of the embedded particle distributions were flat in transverse momentum and rapidity.

4.2 Missing material in the geometry description in simulations

The accurate simulation of the conversion probability depends on an accurate description of the material in the detectors up to the outer field cage of the TPC. As shown in equation 3.1, the radiation length of a material depends on the square of the nuclear charge. Therefore it is not sufficient to know about the position, mass and density of the material, but also which elements it is composed of. The geometry description of the TPC gas is very accurate because it is a large volume of a homogenous material. In contrast the SVT and SSD have a very complex geometry with their silicon ladders, support structure and readout electronics. Therefore the description in the simulation is necessarily less accurate.

The accuracy of the geometry description can be studied for the material in a given detector or detector component *det*. The number of conversions n_{det} in this material is divided by the number of conversions in the TPC gas n_{gas} in the radius range from 60 to 100 cm. Figure 4.2 shows the comparison of data and Monte Carlo after dividing each by the number of conversions in the TPC gas. A deficiency of conversions at the

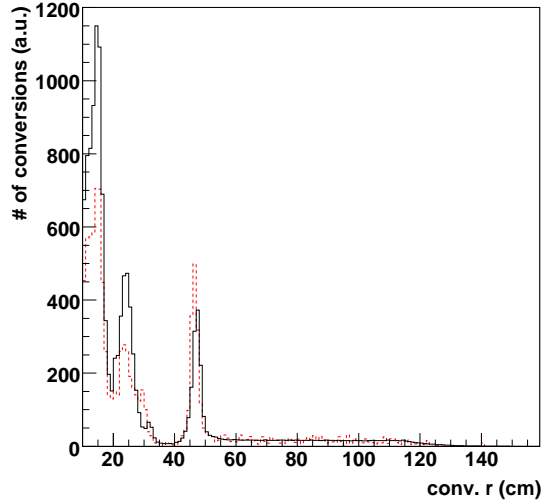


Figure 4.2: The number of conversions versus the radius is shown in central Au+Au collisions at $\sqrt{s_{\text{NN}}} = 62 \text{ GeV}$ (black solid line). This is compared to the number of conversions versus the radius from embedding in the same data set (red dotted line). Both distribution were divided by the number of conversion between 60 and 100 cm radius.

radii, where the SVT and SSD sit, in the simulation compared to data is clearly visible. There appear to be slightly more conversions in the inner field cage in simulation than in real data.

To see, where material is missing in the z direction, the ratio $n_{\text{det}}/n_{\text{gas}}$ was drawn versus z . It is shown for the SVT in figure 4.3 on the left side. Conversions in the SVT were selected by requiring the radius of the conversion to be $10 < r < 20 \text{ cm}$. To get a more detailed view on what is missing, the following double ratio is taken:

$$\text{geomacc}_{\text{det}} = \frac{\frac{n_{\text{det,mc}}}{n_{\text{gas,mc}}}}{\frac{n_{\text{det,data}}}{n_{\text{gas,data}}}} \quad (4.2)$$

The ratio for conversions in the SVT volume versus z is shown in figure 4.3 on the right side. This ratio clearly exhibits some missing material in the region of $12.5 < |z| < 30 \text{ cm}$ (labeled B and C) relative to the regions in between these holes (A and D). But even for the regions A and D the ratio is not equal to one indicating missing material in the simulation geometry description.

Comparisons as for the SVT were also made for the SSD ($20 < r < 40 \text{ cm}$) and the inner field cage of the TPC ($40 < r < 55 \text{ cm}$). The simulation differ from the data in

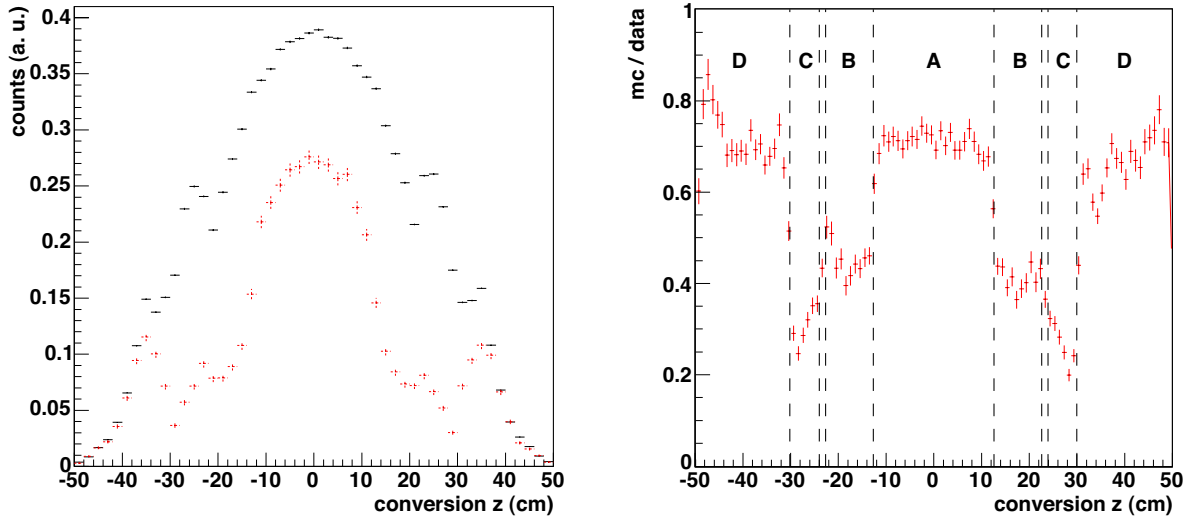


Figure 4.3: The comparison of the number of conversions in the SVT after dividing by the number of conversions in the radius range from 60 to 100 cm for data (black solid) and Monte Carlo simulations (red dashed) is shown on the left side. It is obvious that the number of conversions in the simulations is a lot smaller than the number of conversions in the data. At a distance of more than 38 cm from the center of the detector both distributions start to agree a lot better. On the right side is the ratio of the number of conversions in the SVT in Monte Carlo to data after normalization to the number of conversions in the TPC gas.

the inner field cage by about 11%. The discrepancies in the SSD are of similar size as for the SVT, but do not exhibit a pronounced z -dependence as shown for the SVT.

To reduce the size of the systematic error only conversions in the z -areas of the ladder volumes are used, where the amount of material is relatively well known and rather homogenous. This corresponds to conversions with $|z| < 22$ cm at the SVT radius range $10 < |z| < 20$ cm and to $|z| < 40$ cm at the SSD radius range $20 < |z| < 40$ cm. To correct for the discrepancies discussed above correction factors were applied: A reconstructed photon, which was associated to a simulated photon and converted in one of these volumes, is weighted with the factors given in table 4.1. The correction factors for the SVT holes visible in figure 4.3 on the right side in region B and C were derived by average over region B and C and dividing them by the the average over region A. The correction factor for region B was only applied for the π^0 -embedding because the missing material, too short read-out-boards, have been identified and corrected before the photon embedding was run. The global correction factors for the SVT, SSD and inner field cage are determined by averaging over the remaining z -independent offset, for the SVT and SSD restricted to the z -regions, $|z| < 30$ cm and $|z| < 45$ cm respectively.

Photon embedding			
detector	conv. radius	conv. z	corr. factor
SVT	10cm < r < 20cm	24cm < $ z $ < 30cm	2
		$ z $ < 30cm	1.41
SSD	20cm < r < 40cm	$ z $ < 45cm	1.33
Inner Field cage	40cm < r < 55cm	$ z $ < 200cm	1.11
π^0 embedding			
detector	conv. radius	conv. z	corr. factor
SVT	10cm < r < 20cm	12.5cm < $ z $ < 22.5cm	1.6
		24cm < $ z $ < 30cm	2
		$ z $ < 30cm	1.41
SSD	20cm < r < 40cm	$ z $ < 45cm	1.33
Inner Field cage	40cm < r < 55cm	$ z $ < 200cm	1.11

Table 4.1: If a conversion from simulation was reconstructed in one or more of these volumes, it was weighted by the product of the volumes weights. The first table is applied for photon- and the second for π^0 -embedding. Before the photon embedding was run, the missing material relating to this correction has been identified and added to the geometry description.

The average was done using the ratios versus transverse momentum.

To estimate the uncertainty on the correction, the ratios for all normalized volumes together versus transverse momentum are plotted for different centralities and rapidity ranges. The comparison is shown in figure 4.4. The observed ratios differ by up to 10%, when averaged over transverse momentum. This is taken as the systematic error.

4.3 Photon matching efficiency

To determine the efficiency of the algorithm matching a reconstructed photon to a Monte Carlo photon, a set of Monte Carlo events containing only simulated photons is used. All tracks in these events originate from photon conversions. The charged track multiplicity in this set of events is comparable to the one in 20 – 40% central $Au + Au$ -collisions at $\sqrt{s_{NN}} = 62$ GeV. The number of simulated photons, which have a reconstructed photon matched, is compared to the number of all reconstructed photons after mixed event background subtraction. The ratio giving the matching efficiency is shown in Figure 4.5. The matching efficiency is better than 90% above a photon transverse momentum of 0.5 GeV/ c . The measured ratio was used to correct the reconstruction efficiency.

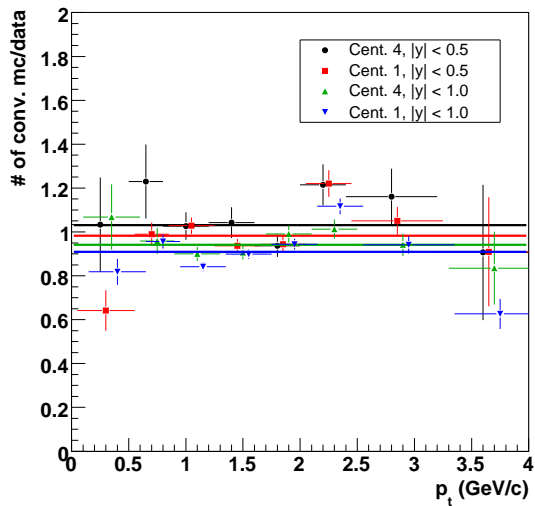


Figure 4.4: Ratio of the number of conversions in the radius range of $10 <r< 55$ cm after application of the geometry correction to the number of conversions in the TPC gas at $60 <r< 100$ cm. To estimate the systematic errors two different collisions centralities (for definition see section 5.1) and two different rapidity ranges were used. The largest average deviation from unity is below 10% when averaging over transverse momentum.

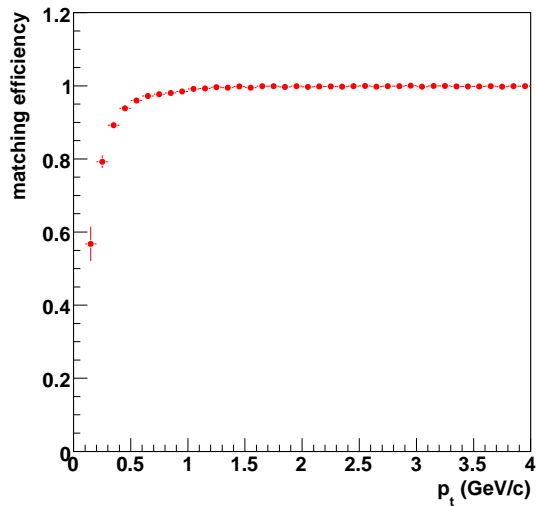


Figure 4.5: Efficiency of the photon matching algorithm.

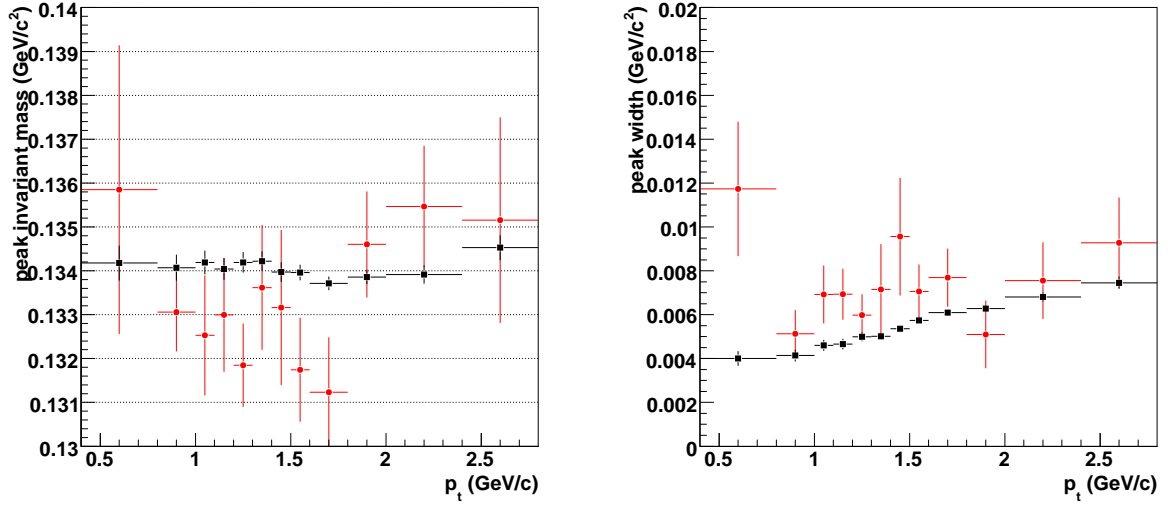


Figure 4.6: This plot shows the comparison of the position (left) and width (right) of the fit to the π^0 -peak in data (red circles) and simulation (black squares) for minimum bias Au+Au-collisions at $\sqrt{s_{\text{NN}}} = 62$ GeV.

4.4 Momentum resolution and energy loss correction

While the particles traverse the detectors, their momentum is changed by collisions with the material. This results in a systematic energy loss of the particles as well as a random change of direction. In addition to the uncertainty caused by scattering the resolution of the detectors is also limited. This increases the measured yield at a fixed transverse momentum in exponentially shaped spectra. The energy loss shifts the spectra to a lower transverse momentum. Both effects work in opposite direction, but do not cancel each other completely and therefore need to be taken into account.

In the Monte Carlo simulations both effects have been incorporated. To see whether they are reproduced correctly, the position and width of the π^0 -peak can be compared in data and simulation. Figure 4.6 shows the position and width of the peaks in data and simulation, which were both fitted by a gaussian. In simulation the peak position comes out about 1 MeV/c^2 below the π^0 -mass independent of transverse momentum. For data the observed mass is about 2 MeV/c^2 low. The transverse momentum dependence of the peak shape is similar for both of them, but on average the width in simulation is smaller than in data.

This can be explained by the missing material in the geometry description, because there is less material off which the particles scatter.

To correct for these effects to the extent they are accounted for in simulation, the efficiency is not simply calculated as the ratio of simulated particles with a matched reconstructed particle over all simulated particles. Rather the number of reconstructed particles in a phase space bin, which were associated to simulated particles, are divided by all simulated particles in that phase space bin. A reconstructed particle may then end up in a different phase space bin than the simulated particle it is associated to. Therefore the statistical errors are not binomial.

Because the overall effect of the momentum smearing depends on the shape of the spectrum, it is important to take into account the different spectral shapes in data and simulation. This is also important if the efficiency changes strongly over the range of a single phase space bin. The rapidity dependence of the spectra is flat in simulation and data near the center of mass where the data is taken. The transverse momentum dependence, however, in data is steeply falling in data and flat in simulation. To correct for this difference the spectra in simulation were re-weighted with a powerlaw fit to the corrected spectra from data. Because efficiency corrections are necessary to obtain corrected spectra this procedure is iterative. This re-weighting is also useful at low transverse momentum

4.5 dE/dx cut correction

The detector response simulator for the TPC calculates from the energy deposited by a Monte Carlo track traversing the TPC gas the signal, which is induced in the pads on the read out plane and read out by the electronics. While this is qualitatively done correctly the absolute normalization of the simulated signal is not reliable. Therefore the dE/dx cut used for data analysis is not applied to tracks, which were matched to Monte Carlo tracks. Leaving out this one cut results in a higher reconstruction efficiency in simulation than in data. The cut in the data is applied on the dE/dx deviant, which is the deviation of the dE/dx value from the Bethe-Bloch-Value for a certain momentum in units of sigma of the distribution. Therefore the shape of this distribution is largely independent of the momentum of the positron or electron. Figure 4.7 on the left side shows the distribution of the dE/dx deviant for data (black solid line) and mixed events (red dashed line). The mixed event distribution is similar to the overall dE/dx distribution in events, where the positron or electron peak is only a small bump on the tail of the charged π -meson peak sitting to the left of this histogram. To estimate the amount of photons lost in data due to that cut, the distribution of the dE/dx deviant has been plotted after all cuts have been applied and the mixed event background has been subtracted. It can be nicely fitted by a gaussian from -2. to 2 as shown in figure 4.7. This range was chosen to avoid the tails of the distribution, where the contamination by other charged particles is of similar size as the electron or positron signal. Assuming a gaussian shape for the whole distribution the fraction of photons surviving the cut is estimated to be 99% for single e^+ and e^- tracks. This means 98.01% for a photon and 96.06% for a π^0 -meson. The

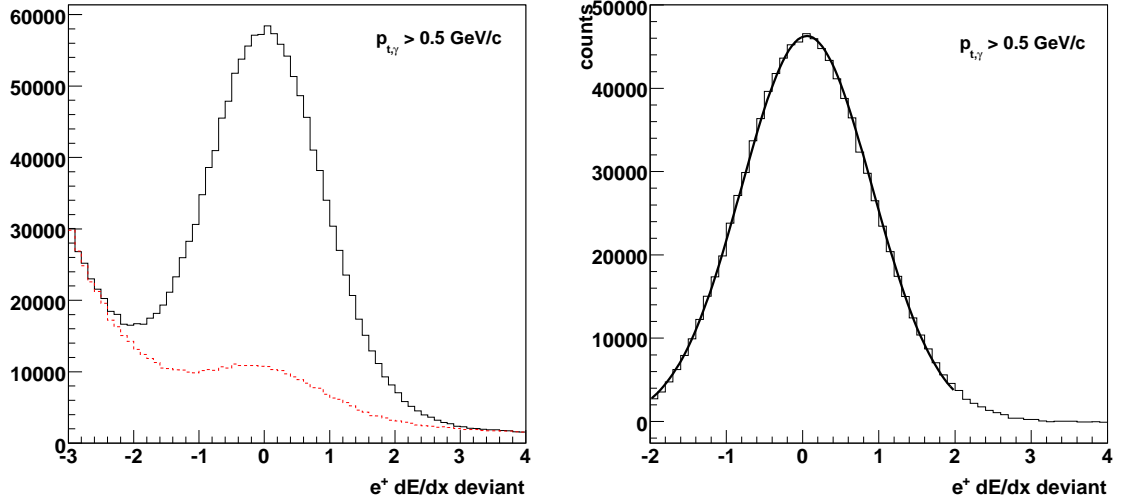


Figure 4.7: On the left the distribution of the dE/dx deviant is shown for positrons from reconstructed conversions in real data (black solid line) and mixed events (red dashed line). The left plot shows a gaussian fit to the peak in the distribution of the same positron dE/dx deviant after subtraction of the combinatorial background.

dependence of these factors on the photon transverse momentum was studied and found not to be statistically significant. Therefore the factors are multiplied to the efficiency correction independently of rapidity and transverse momentum.

4.6 Estimate of systematic uncertainties

Because the embedding procedure is never completely accurate, the systematic uncertainties due to differences between the simulation and real data have to be studied.

4.6.1 Uncertainty in the geometry correction

As it is shown in section 4.2 an apparent discrepancy of about 30% between the radiation length of the SVT and SSD in data and simulation is observed. While a correction has been applied by re-weighting the conversion in simulation in the SVT and SSD region, this correction is not perfect. Because most photon conversions happen in the material of these two detectors, the uncertainty in this correction affects the overall detection efficiency at the same order. The overall uncertainty on the photon efficiency is estimated

to be 10% and on the π^0 -efficiency 20%.

4.6.2 Other uncertainties in the embedding procedure

	cut variable	def. cut	var. 1	var. 2		#
e^+/e^-	number of hits	≥ 12	≥ 18	≥ 6		1
	hits / possible hits	≥ 0.55	≥ 0.65	≥ 0.45		2
photon	abs(xy-dist)	< 1.5	< 0.75	< 2	cm	3
	abs(z-dist)	< 1	< 0.7	< 1.5	cm	4
	Δ dip	< 0.035	< 0.02	< 0.1	rad	5
	$\Delta\phi$	< 0.05	< 0.03	< 0.07	rad	6
	dip difference with only dip component	< 0.03	< 0.02	< 0.04	rad	7
	of opening angle	< 12	< 6	< 50	MeV/c ²	8

Table 4.2: Default cuts and two variations used to study the systematic uncertainty of the embedding procedure. Each cut was varied independent of the others.

To estimate the accuracy of the reconstruction efficiency for a photon conversion, the dependence of the final photon- and π^0 -spectra on the variation of the cuts was studied. In addition a kinematic cut requiring each of the daughter particles to carry at most 75% of the photon energy was tested (cut variation #9). To study the sensitivity of the selected threshold requiring 75% of common points for a simulated and a reconstructed track to be matched, this was also varied to 50% and 90% (cut variation #10). The other cuts were varied as shown in table 4.2.

The final spectra are reconstructed for each of the cut sets and divided by the standard cut set to make the differences visible. The resulting ratios are shown in figure 4.8. The largest observed differences below 4 GeV/c transverse momentum are below 5%, when averaged over transverse momentum. This is taken as the systematic uncertainty of the photon reconstruction efficiency. For the systematic uncertainties in the π^0 -efficiencies there is one more cut tested, which restricts the same procedure was applied to the π^0 -embedding and resulted in a systematic uncertainty of about 10%. Those ratios are shown in 4.9.

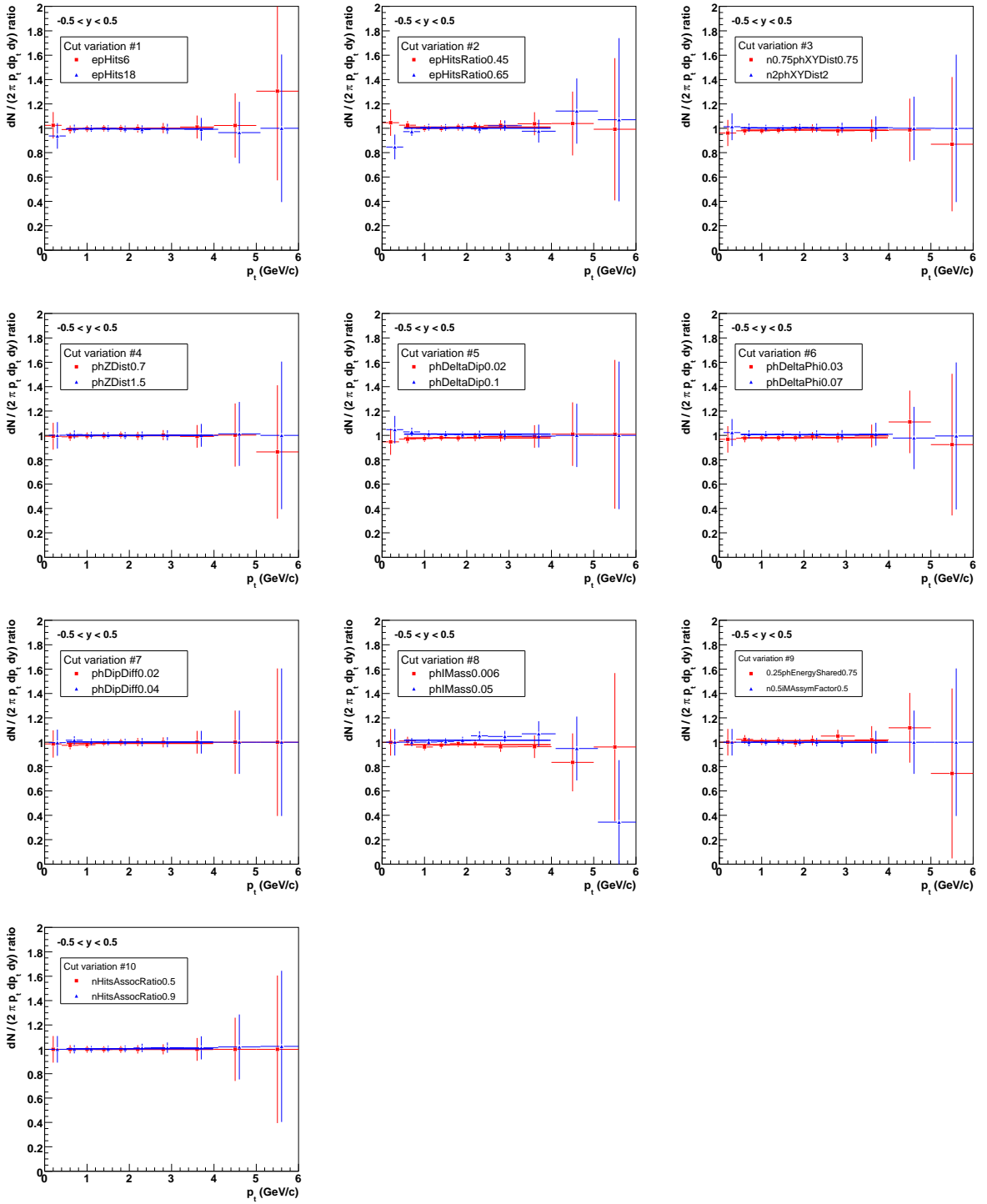


Figure 4.8: Variations of the cuts as given in table 4.2. The plots show the ratios of the photon spectra with the varied cuts to the photon spectra with the standard cuts. All plots are from minimum bias Au+Au-collisions at $\sqrt{s_{NN}} = 62$ GeV and a rapidity range $|y| < 0.5$.

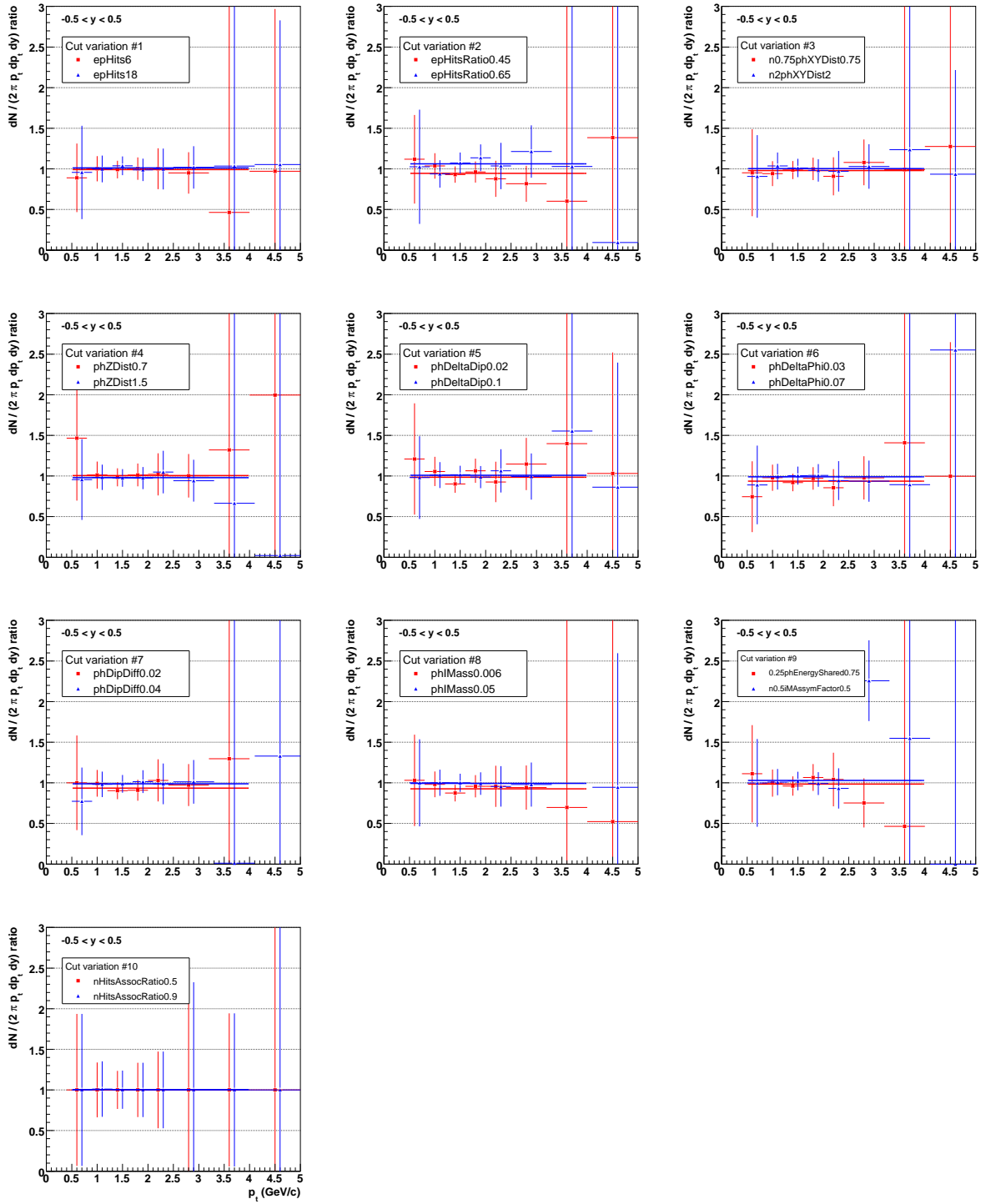


Figure 4.9: Variations of the cuts as given in table 4.2. The plots show the ratios of the π^0 -spectra with the varied cuts to the π^0 -spectra with the standard cuts. All plots are from minimum bias Au+Au-collisions at $\sqrt{s_{\text{NN}}} = 62$ GeV and a rapidity range $|y| < 0.5$.

5 Results

5.1 Data set

The data used for the analysis was taken in the RHIC run 4 at the energy of $\sqrt{s_{\text{NN}}} = 62 \text{ GeV}$. Two different triggers were used to select events. One of them was a minimum bias trigger requiring both ZDCs to be above threshold. This trigger selects a large fraction of the inelastic events, but is inefficient for very central collisions, where only very few spectator neutrons reach the ZDCs. Therefore an additional central trigger was applied to catch those central events lost by the minimum bias trigger. It required a coincidence of both BBCs and a vertex position in the range of $\pm 100 \text{ cm}$ from the the BBC timing difference. After run number 5086037 the trigger setup was modified. For the remainder of the data taking period the minimum bias trigger was extended with the requirement to have the CTB sum of at least 15 and the vertex position from the ZDC timing difference to be in the range of $\pm 50 \text{ cm}$. The central trigger then required in addition a CTB sum of at least 10000 and a BBC vertex in the range of $\pm 50 \text{ cm}$. Of the events satisfying at least one of these four triggers all those are selected for the analysis, which have a main event vertex reconstructed by extrapolating tracks in the TPC back to the beam line. The position of this vertex has to be at most 4 cm in the radius and $\pm 30 \text{ cm}$ in the z coordinate.

centrality	% of inel. cross section	reference multiplicity	number of events	number of binary collisions
1	40 – 80	9 – 101	3,174,862	50 $^{+11}_{-12}$
2	20 – 40	102 – 221	1,585,198	257 $^{+37}_{-35}$
3	10 – 20	222 – 312	780,195	512 $^{+55}_{-48}$
4	0 – 10	313 – ∞	793,977	809 $^{+65}_{-59}$
min. bias	0 – 80	9 – ∞	6,334,232	252 $^{+28}_{-27}$

Table 5.1: Centrality definition and the number of events available in each centrality bin in the data set. Also given are the number of binary nucleon-nucleon-collisions for each centrality bin in Au+Au-collisions at $\sqrt{s_{\text{NN}}} = 62 \text{ GeV}$ determined by Glauber calculations [Gon06, Mil03].

The data set is divided into four different centrality event classes based on the reference multiplicity, which is the number of primary tracks with at least 10 fit points in the TPC within $|\eta| < 0.5$. The multiplicity cut for the four centrality bins and minimum bias collisions are listed in table 5.1. The table also shows the number of binary nucleon-nucleon-collisions occurring in a heavy ion collision at the given centrality. These numbers were obtained from Glauber calculations [Gon06]. A more detailed explanation, how these calculations were done, is given in [Mil03], appendix E.

5.2 Inclusive photons

5.2.1 Photon detection efficiency

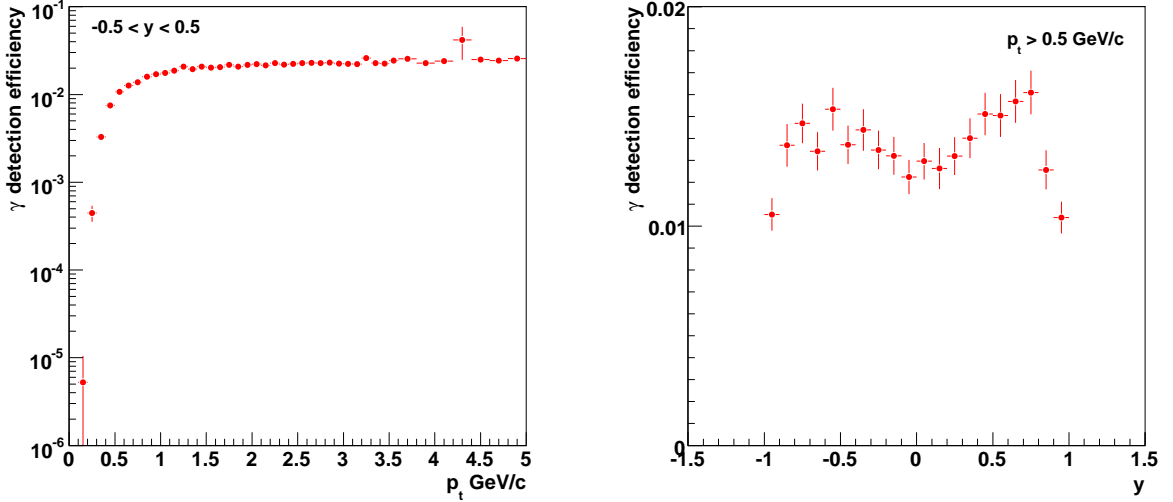


Figure 5.1: The photon detection efficiency versus transverse momentum (left) and rapidity (right) of the photon is shown in minimum bias Au+Au-collisions at $\sqrt{s_{\text{NN}}} = 62$ GeV. The errors on both plots are statistical only.

The photon detection efficiency is determined using the embedding method and all corrections described in chapter 4. The probability for a photon to convert before reaching the sensitive gas volume of the TPC is on average below 10%. While this probability only slightly depends on the energy of the photon, the tracking efficiency of the daughters depends strongly on their transverse momentum. This results in a rapid decrease in reconstruction efficiency of a converted photon towards low transverse momenta. The overall shape of the photon detection efficiency versus transverse momentum is shown in figure 5.1 on the left side.

The conversion probability of a photon in STAR is mainly dependent on the dip-angle as defined in section 2.2.1. The amount of material traversed before reaching the sensitive gas of the TPC is roughly proportional to the path length, which is proportional to the tangent of the dip-angle. Tracks with $|\text{dip}| > .7$ rad can hit the end-cap of the TPC barrel and therefore no longer traverse the full diameter of the TPC. This results in less than the maximum number of possible TPC points on these tracks and thus a reduced reconstruction efficiency. Because for mass-less particles the dip-angle is directly correlated with the rapidity, the photon detection efficiency can then be plotted versus rapidity as shown in figure 5.1 on the right side.

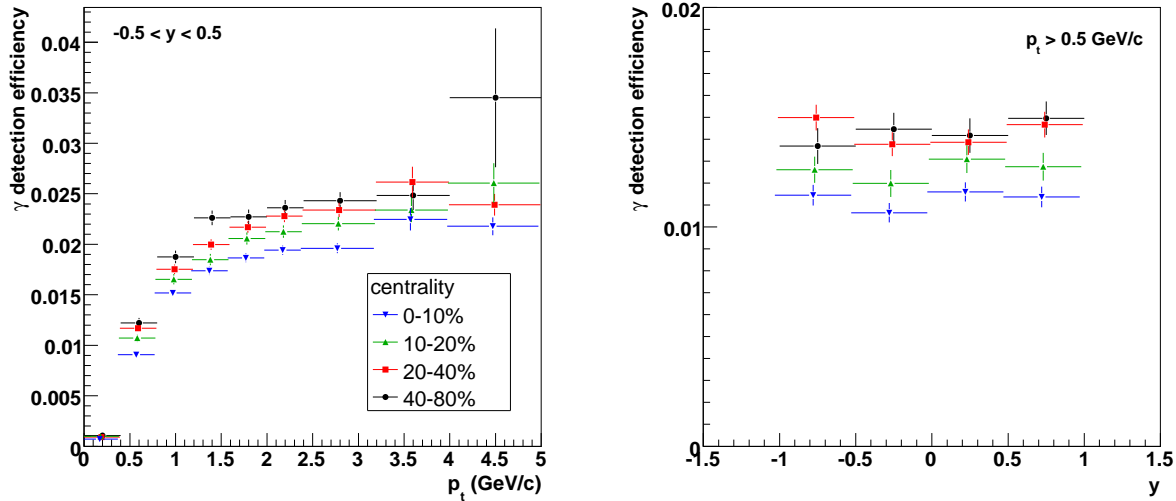


Figure 5.2: Photon detection efficiency versus transverse momentum (left) and rapidity (right) of the photon for Au+Au-collisions at $\sqrt{s_{\text{NN}}} = 62$ GeV at four different centralities. The errors are statistical only.

Figure 5.2 shows the transverse momentum and rapidity dependence of the photon detection efficiency for the four centrality selections used in this analysis. For the most central selection the efficiency is about 20% lower than for the most peripheral one. This is attributed to the higher track density in the TPC in central collisions. Therefore the track-finding efficiency is reduced and thus the photon detection efficiency. This also shows that it is important to calculate the efficiency centrality dependent.

5.2.2 Inclusive photon spectra

The inclusive photon spectrum versus transverse momentum after all corrections is shown for minimum bias collisions in figure 5.3 on the left side. The spectra start at 200 MeV/c and extend to about 5 GeV/c. The shape of the spectrum can be fitted by a power law function. In addition to the shown statistical errors there is a systematic uncertainty of 10% due to uncertainty in the geometry description and 5% due to the embedding procedure.

The rapidity dependence of inclusive photon spectra in minimum bias collisions is shown in figure 5.3 on the right side. A cut for transverse momenta below 0.5 GeV/c is made to avoid the phase space region, where the photon reconstruction efficiency is very small and strongly dependent on rapidity. The resulting photon spectrum shows no systematic variation with rapidity. The shape also seems to stay constant when looking at the

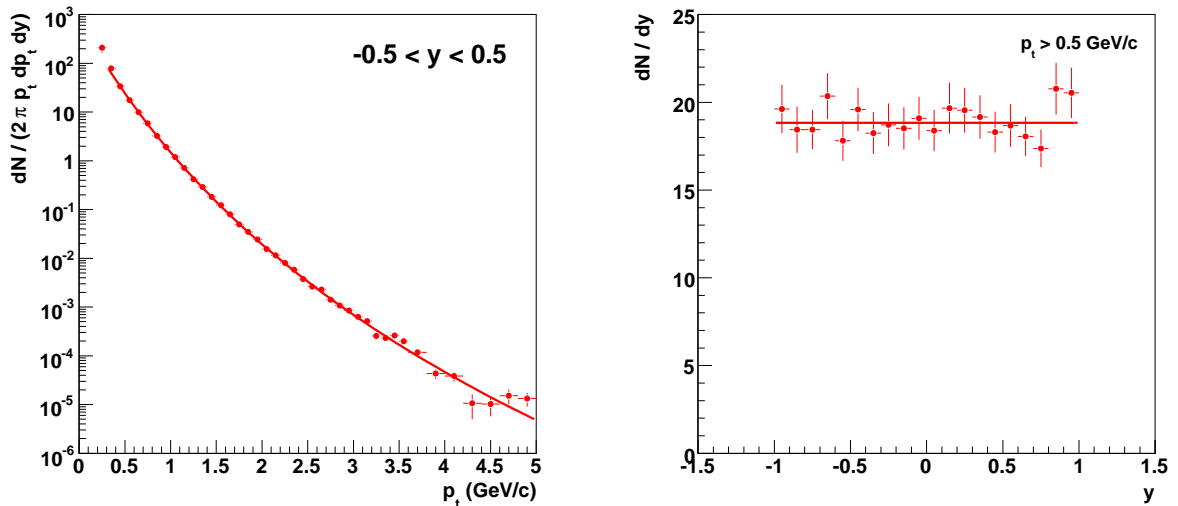


Figure 5.3: Inclusive photon spectra in minimum bias Au+Au-collisions at $\sqrt{s_{\text{NN}}} = 62 \text{ GeV}$ versus transverse momentum (left) and rapidity (right). The lines are a powerlaw fit to the transverse momentum spectra and a constant fit to the rapidity spectra. The errors are statistical only. The systematic uncertainties are summarized in section 5.6.

rapidity spectra for different centralities in figure 5.4 on the right side.

In figure 5.4 photon spectra for four different centrality selections are shown versus transverse momentum and rapidity. To get a better comparison of the spectra at the different centralities, R_{CP} is used, which is basically the particle yield produced in a heavy ion collision at a given centrality relative to the particle yield in peripheral collisions. It is defined as

$$R_{\text{CP}} = \frac{n_{\text{bin,peripheral}}}{n_{\text{bin,central}}} \times \frac{dN_{\text{central}}^2 / dp_t dy}{dN_{\text{peripheral}}^2 / dp_t dy} \quad (5.1)$$

$n_{\text{bin,cent}}$ and $n_{\text{bin,peripheral}}$ are the number of binary nucleon-nucleon-collisions in a nucleus-nucleus-collision at the centrality and in peripheral collisions respectively. They are listed in table 5.1. This normalization is done to take into account the purely geometrical effects due to the different system sizes at different centralities. Because hard scattering processes are expected to scale with the number of binary collisions, this scaling is mainly used for the analysis of particle production at high transverse momentum. At low transverse momentum particle production in heavy ion collisions is dominated by the medium. Therefore different scaling methods like the number of nucleons participating in the collisions are commonly used there. For this analysis binary collision scaling is

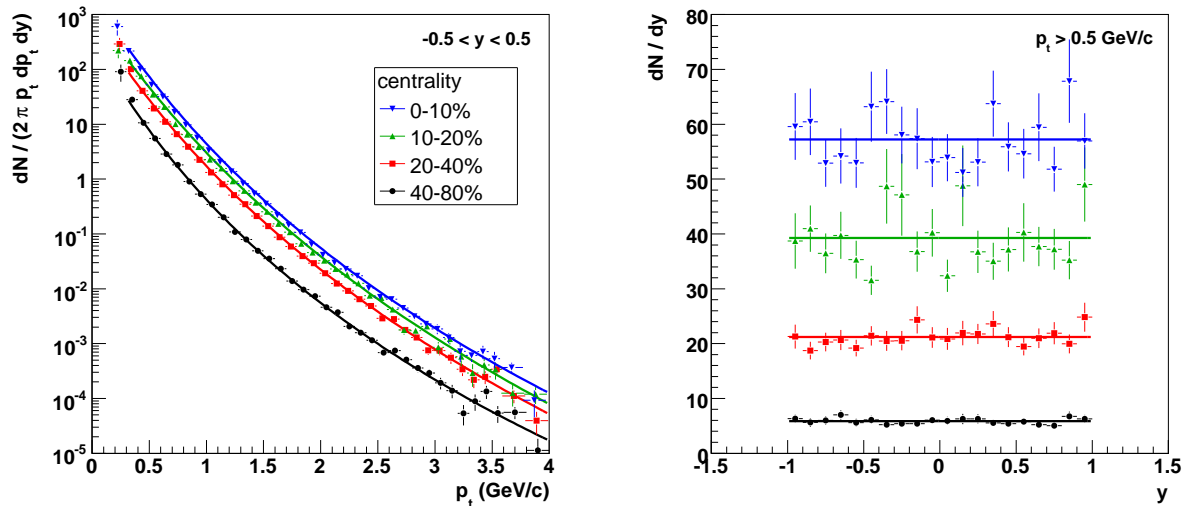


Figure 5.4: Inclusive photon spectra for 4 different centrality selections versus transverse momentum (left) and rapidity (right). The lines are powerlaw fits to the transverse momentum spectra and constants to the rapidity spectra. The errors are statistical only. The systematic uncertainties are summarized in section 5.6.

used, because the spectra extend up to $4 \text{ GeV}/c$, where the application of this scaling is common.

Technically the ratio is calculated by fitting a power law function

$$f(p_t) = 2\pi a \left(1 + \frac{p_t}{b}\right)^{-1c} \quad (5.2)$$

to the spectrum in the peripheral bin. The parameters of the power law function are $a = 72 \pm 1.3$, $b = 1.3 \pm 0.16$, $c = 11.7 \pm 0.51$. The spectra in all four centrality selections are divided by this fit and then scaled by the number of binary collisions as in equation 5.1. The resulting ratios are shown in figure 5.5 on the left side.

The plot shows the suppression getting gradually stronger for the collisions getting more central. For the most central bin the suppression factor is between 0.5 and 0.7. As most of the photons come from π^0 -decays this factor should roughly reflect the R_{CP} for π^0 -mesons.

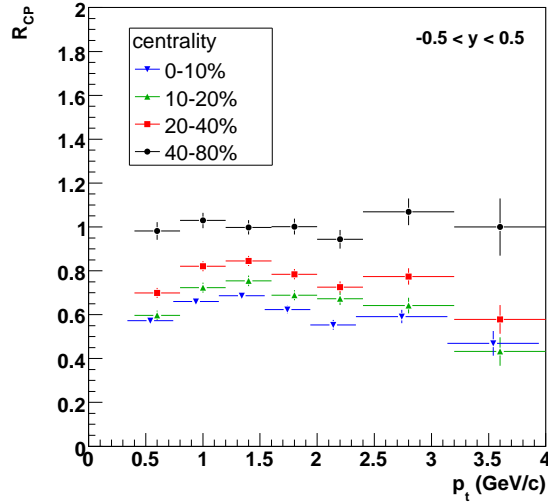


Figure 5.5: The central to peripheral ratio, R_{CP} of inclusive photon spectra is shown. The ratio has been obtained by fitting the most peripheral bin with a power law fit and dividing the spectra in all centrality bins by that fit. The ratio for the most peripheral bin is also shown to give an illustration of the uncertainty.

5.3 π^0 -mesons

5.3.1 π^0 detection efficiency

Figure 5.6 on the left side shows the π^0 -detection efficiency for minimum bias Au+Au-collisions at $\sqrt{s_{NN}} = 62$ GeV. It is to first order given by the square of the photon efficiency and thus exhibits qualitatively the same shape: It is very low for low transverse momenta and rises with increasing transverse momentum of the π^0 -meson. The rise is slower than for the photon efficiency because the π^0 momentum is split up on the two daughter photons. Because the two daughter photons usually split the π^0 -momentum asymmetrically and fly in different directions, the π^0 detection efficiency is not exactly the square of the photon detection efficiency.

Because of the strong transverse momentum dependence of the π^0 -detection efficiency a lot of statistics in simulation is necessary to determine the efficiency for low transverse momenta.

On the right side on figure 5.6 the π^0 -detection efficiency is shown for four different centrality selections. The centrality dependence of the π^0 -detection efficiency is much stronger for low than for high transverse momenta.

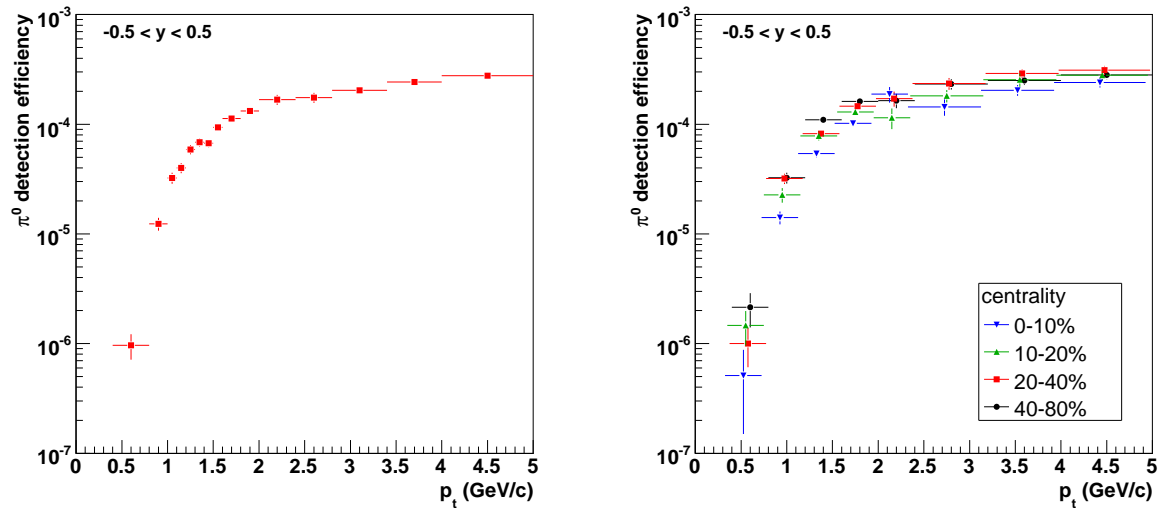


Figure 5.6: Detection efficiency for π^0 -mesons with $|y| < 0.5$ versus transverse momentum. On the left side the efficiency is shown for minimum bias Au+Au collisions at $\sqrt{s_{\text{NN}}} = 62$ GeV, while on the right side four different centralities are selected. The errors are statistical only.

5.3.2 π^0 -spectra

The fully corrected π^0 -spectrum versus transverse momentum for minimum bias Au+Au collisions is shown in figure 5.7 on the left side. The reconstructed spectrum starts at 0.5 GeV/c transverse momentum and reaches up to 5 GeV/c. To the high end of the spectrum the measurement is limited by the available statistics in the data set.

The transverse momentum spectra of π^0 -mesons for four different centrality selections are shown in figure 5.7 on the right side. The reduced coverage in transverse momentum compared to the minimum bias spectra is due to the lower statistics available, when dividing the data set into different centrality bins. To study the centrality dependence in more detail the π^0 -R_{CP} as defined in equation 5.1 is shown in figure 5.8. Even though scaling by the number of binary collisions is not really meaningful at this low transverse momentum range, the figure shows that the spectra at different centralities are in agreement within the statistical errors after scaling. This shows that the statistical errors are too large to make a statement on the centrality dependence of the π^0 -spectra.

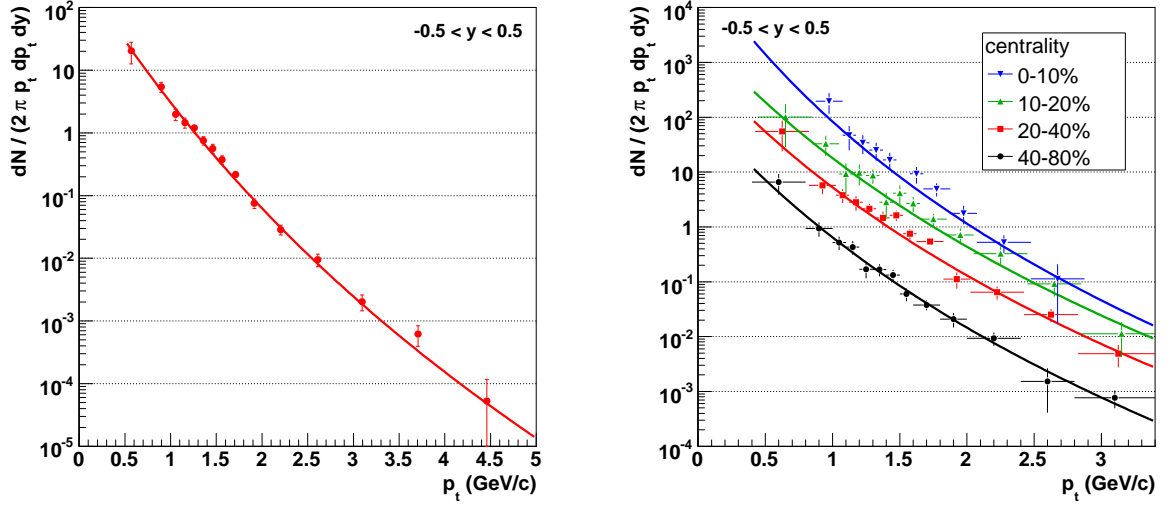


Figure 5.7: On the left side the π^0 -spectrum versus transverse momentum in minimum bias Au+Au-collisions at $\sqrt{s_{\text{NN}}} = 62$ GeV is shown. On the right side are the spectra for four different centralities. The errors are statistical only. The systematic errors on both spectra are $\pm 20\%$ due to the geometry correction, $\pm 10\%$ due to the embedding procedure and $\pm 10\%$ due to the yield extraction from the invariant mass histograms.

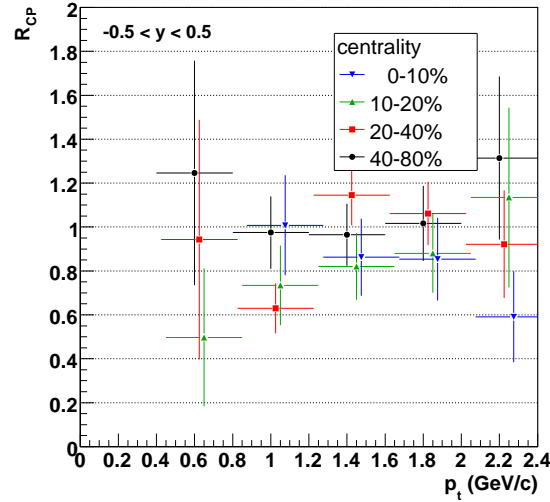


Figure 5.8: R_{CP} for π^0 -mesons in Au+Au-collisions at $\sqrt{s_{\text{NN}}} = 62$ GeV.

5.4 Comparison to other measurements

5.4.1 π^0 -mesons from PHENIX at $\sqrt{s_{\text{NN}}} = 62 \text{ GeV}$

π^0 -spectra were measured by PHENIX in Au+Au-collisions at $\sqrt{s_{\text{NN}}} = 62 \text{ GeV}$ and a preliminary version was presented [Bat]. The spectra in central collisions are compared to the STAR measurement in figure 5.9. For both experiments the π^0 -spectra for the 10% most central collisions are shown. In the region of overlap between $1 \text{ GeV}/c$ and $2.5 \text{ GeV}/c$ transverse momentum both spectra are in agreement within the systematic errors of the STAR- π^0 -spectra of 20% plus 10% plus 10%. While the STAR measurement runs out of statistics at about $2.5 \text{ GeV}/c$ transverse momentum the calorimetric measurement of PHENIX extends up to $7 \text{ GeV}/c$. PHENIX also measured for different centrality selections. Because their choice of centrality binning is different, the spectra are not compared here.

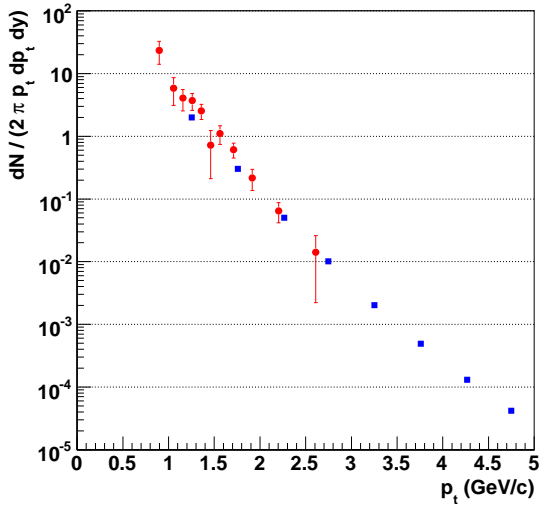


Figure 5.9: Comparison of the π^0 -spectra measured by STAR (red circles) and PHENIX (blue squares) in the 10% most central Au+Au-collisions at $\sqrt{s_{\text{NN}}} = 62 \text{ GeV}$ [Bat].

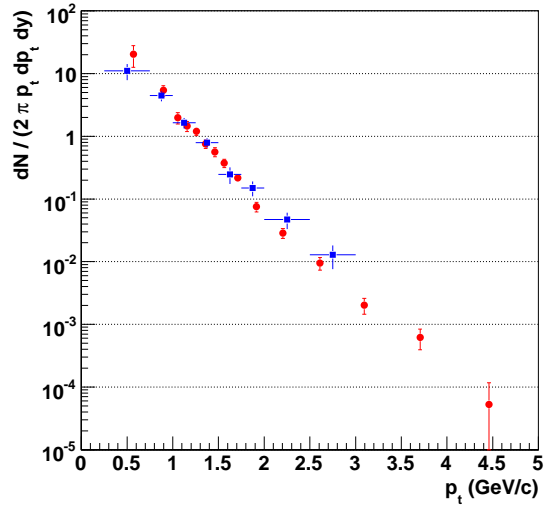


Figure 5.10: Comparison of the π^0 -spectra measured by STAR in minimum bias Au+Au-collisions at $\sqrt{s_{\text{NN}}} = 62 \text{ GeV}$ (red circles) and $\sqrt{s_{\text{NN}}} = 130 \text{ GeV}$ (blue squares).

5.4.2 π^0 -mesons from the STAR TPC at $\sqrt{s_{NN}} = 130$ GeV

There has been a previous measurement of photons and π^0 -mesons using photon conversions in the TPC at a collision energy of $\sqrt{s_{NN}} = 130$ GeV [A⁺04, Joh03]. The data set available for this analysis was much smaller than for the analysis at $\sqrt{s_{NN}} = 62$ GeV. The comparison of π^0 transverse momentum spectra in minimum bias collisions at both energies is shown in figure 5.10. While the minimum bias centrality for $\sqrt{s_{NN}} = 62$ GeV is 0 – 80% it is 0 – 85% for $\sqrt{s_{NN}} = 130$ GeV. Both spectra are very close at low transverse momentum, but the spectrum at $\sqrt{s_{NN}} = 130$ GeV is less steep, resulting in a higher yield at higher transverse momenta.

5.4.3 $\pi^+ - \pi^-$ -spectra from STAR at $\sqrt{s_{NN}} = 62$ GeV

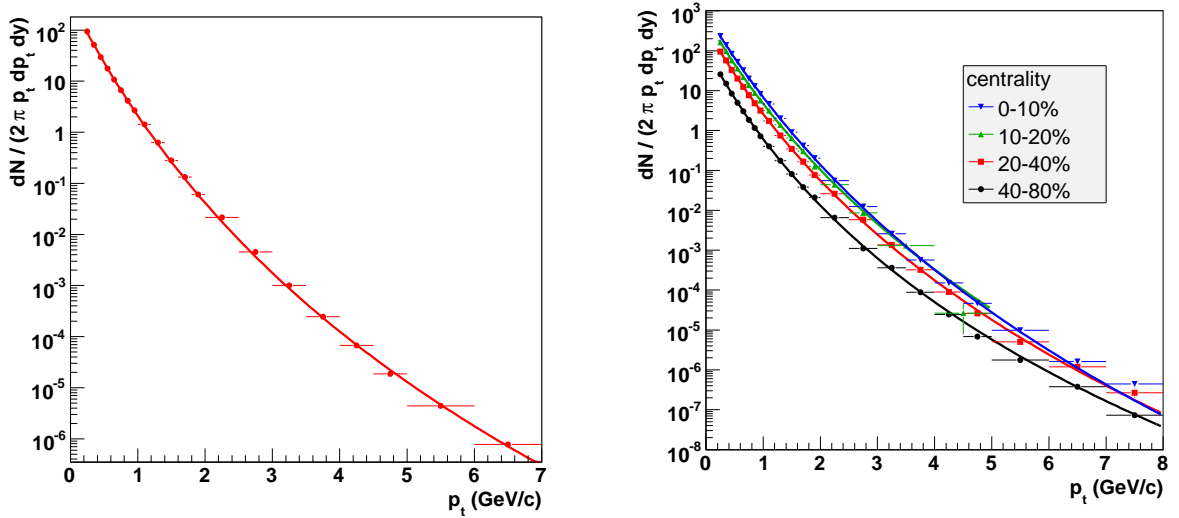


Figure 5.11: $\pi^+ - \pi^-$ -spectra in Au+Au-collisions minimum bias collision (left) and at four different centralities (right) from time of flight and dE/dx measurements are shown. The lines are powerlaw fits to the data.

Besides the π^0 -mesons STAR measures the spectra of $\pi^+ - \pi^-$ -mesons. Because they are charged, they can be measured directly in the TPC unlike π^0 -mesons, which decay into two photons, each of which has to convert into two charged particles to be measurable in the TPC. Due to the resulting detection efficiency, which for charged π -meson spectra is about 1000 times higher than π^0 -mesons, $\pi^+ - \pi^-$ -spectra can be obtained with much smaller statistical errors.

Charged π -meson spectra from two different measurements by STAR in Au+Au-collision at $\sqrt{s_{NN}} = 62$ GeV are used for this comparison: Using the time of flight detector π^+ -

π^- -spectra have been measured in the same four centrality bins, which are used for this π^0 -analysis. They are reaching up to 5 GeV/c transverse momentum [Sha06]. A second measurement uses the TPC for particle identification in the relativistic rise region of the Bethe-Bloch-function provides charged π -meson spectra for 2.5 – 12 GeV/c transverse momentum [Moh06]. These results however are only available for the two peripheral and the most central centrality selection as well as for minimum bias collisions.

To get a good coverage of a large transverse momentum range the spectra are combined by using the ToF data below 3.5 GeV/c and the relativistic dE/dx data above 3.5 GeV/c transverse momentum. For the centrality bin without dE/dx data, only the ToF data is used. For iso-spin symmetry reasons the π^0 -spectra are equal to half of the sum of the π^+ - and π^- -spectra. Therefore the average of both charges is fit by a power law functions (see equation 5.2) for each centrality. The spectra with the power law fits are shown in figure 5.11.

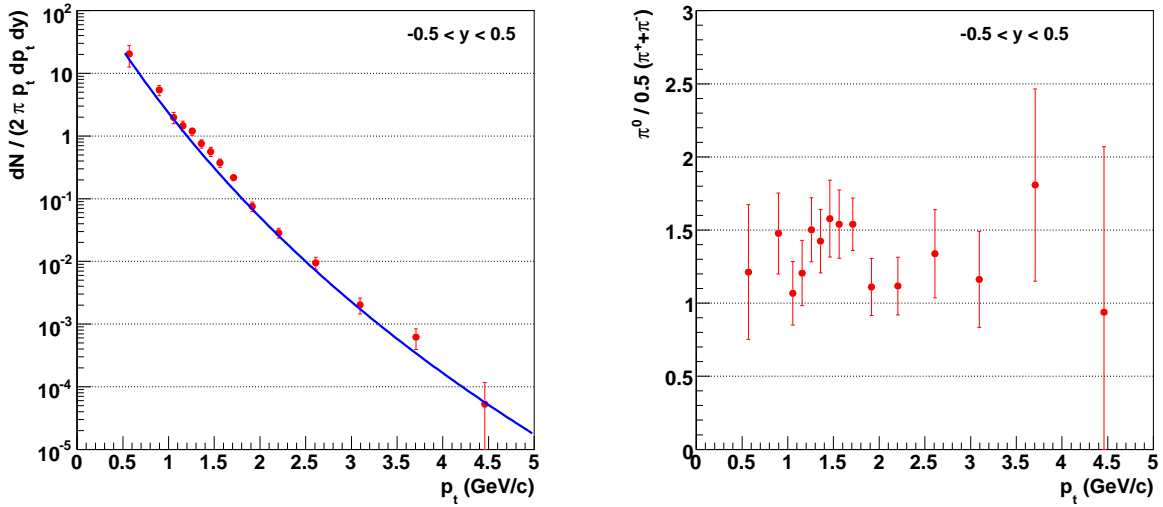


Figure 5.12: The red circles on the left plot show the π^0 -spectrum versus transverse momentum for $|y| < 0.5$. The blue line is a power law fit to the π^+/π^- -spectra for $|y| < 0.5$. On the right side the ratio of the π^0 -spectrum to the power law fit is shown.

The π^+/π^- -spectra coming from the time of flight analysis have an estimated systematic uncertainty of 8% plus 10% normalization uncertainty below 1.6 GeV/c transverse momentum and 5 – 10% in addition for higher transverse momenta.

In figure 5.12 on the left side the minimum bias π^0 -spectra are shown. The blue line on the same plot is a power law function fit to the π^+/π^- -spectra for the same phase space region. For a better comparison the ratio of the π^0 -spectra over the fit is shown in figure 5.12 on the right side. While the π^0 -measurement shows clearly higher yields

than the $\pi^+\pi^-$ -spectra, they are still in agreement due to the large systematic errors on both spectra.

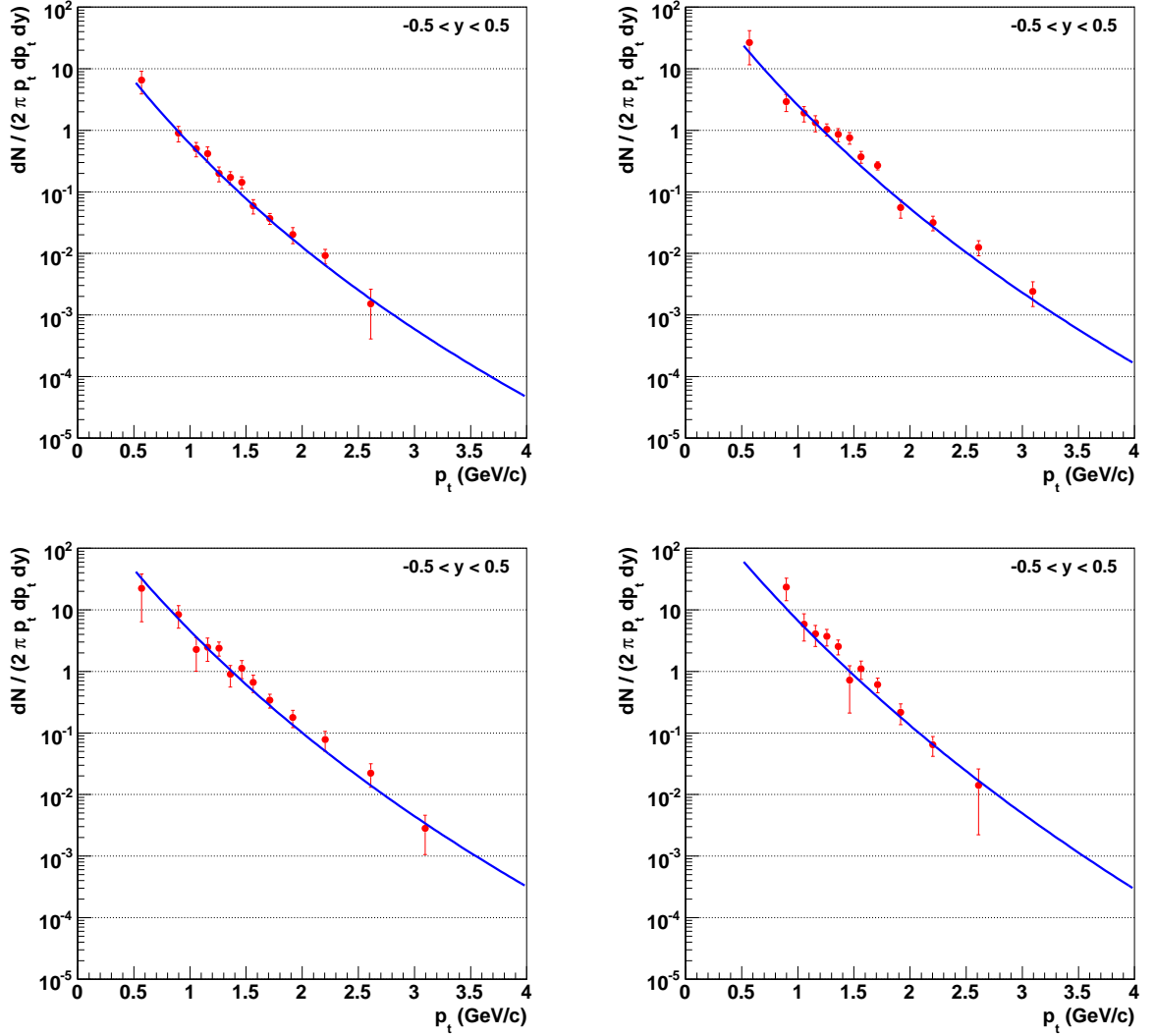


Figure 5.13: The red circles show the π^0 -spectrum versus transverse momentum for $|y| < 0.5$. For the four different centralities (top left: 1, top right: 2, bottom left: 3, bottom right: 4). The blue lines are powerlaw fits to the $\pi^+\pi^-$ -spectra for $|y| < 0.5$ at the different centralities.

Figure 5.13 shows the π^0 -spectra for the four different centralities together with the fits to the $\pi^+\pi^-$ -spectra. The corresponding ratios are shown in figure 5.14. For all four centrality bins the π^0 -spectra are higher than the $\pi^+\pi^-$ -spectra on average by about 20 – 30%, but given the size of the systematic errors both measurements (see section 5.6 for summary) are consistent for all centrality bins.

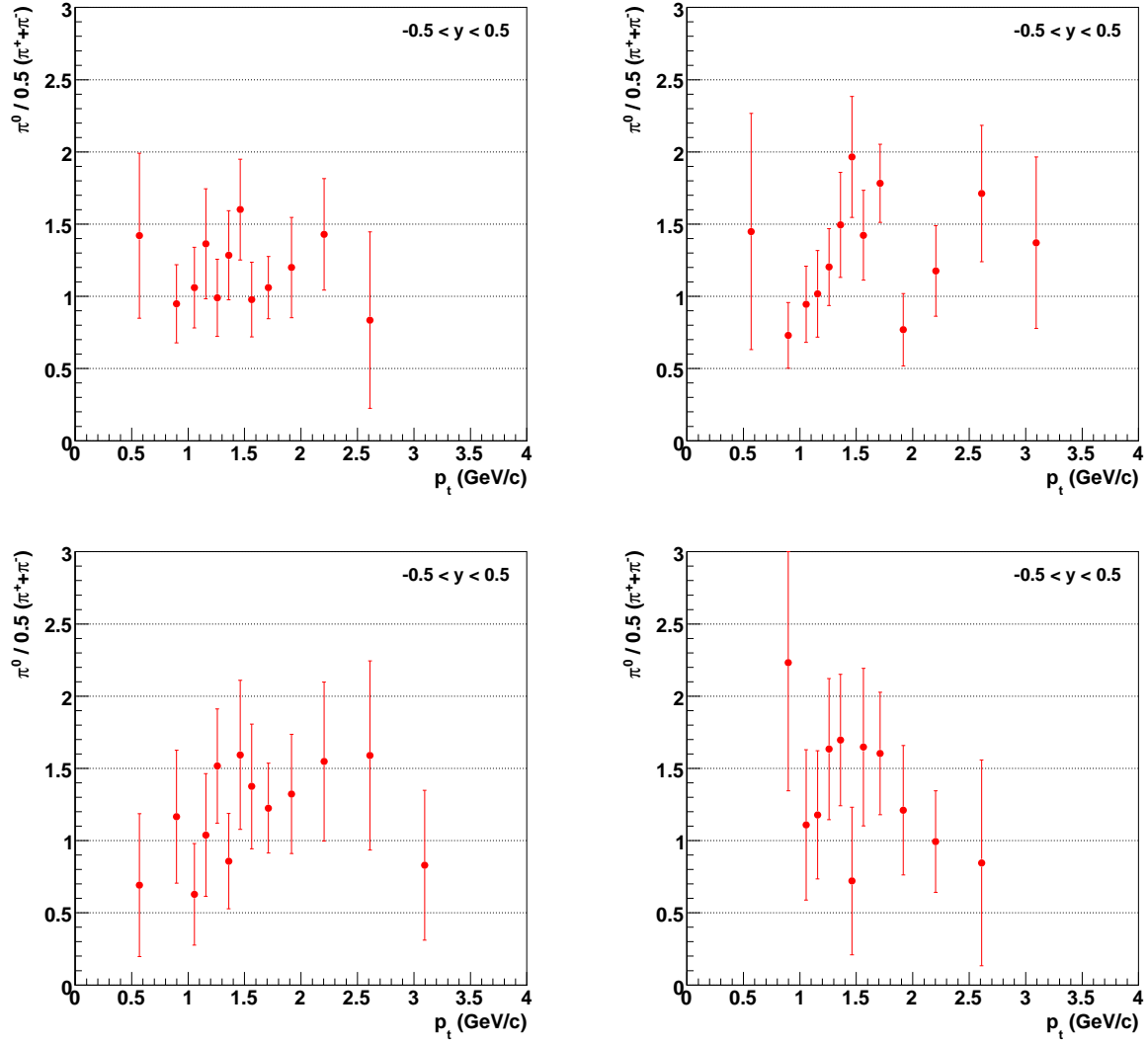


Figure 5.14: The π^0 -spectra shown in figure 5.13 are divided by the fits to the π^+/π^- -spectra for four different centralities (top left: 1, top right: 2, bottom left: 3, bottom right: 4).

5.4.4 Comparison of photons to $\pi^+ - \pi^-$ -spectra from STAR

Most photons in hadronic interactions come from π^0 -decays. Therefore the centrality dependence of the photon spectra should be closely related to the one of the π^0 -spectra. π^0 -spectra are the same as half of the sum of the $\pi^+ - \pi^-$ -spectra. Thus photon spectra from π^0 -decays can be simulated by using the spectral functions $\pi^+ - \pi^-$ -spectra as input to a GEANT simulation of the decays. The resulting spectra can then be compared to the measured inclusive photon spectra.

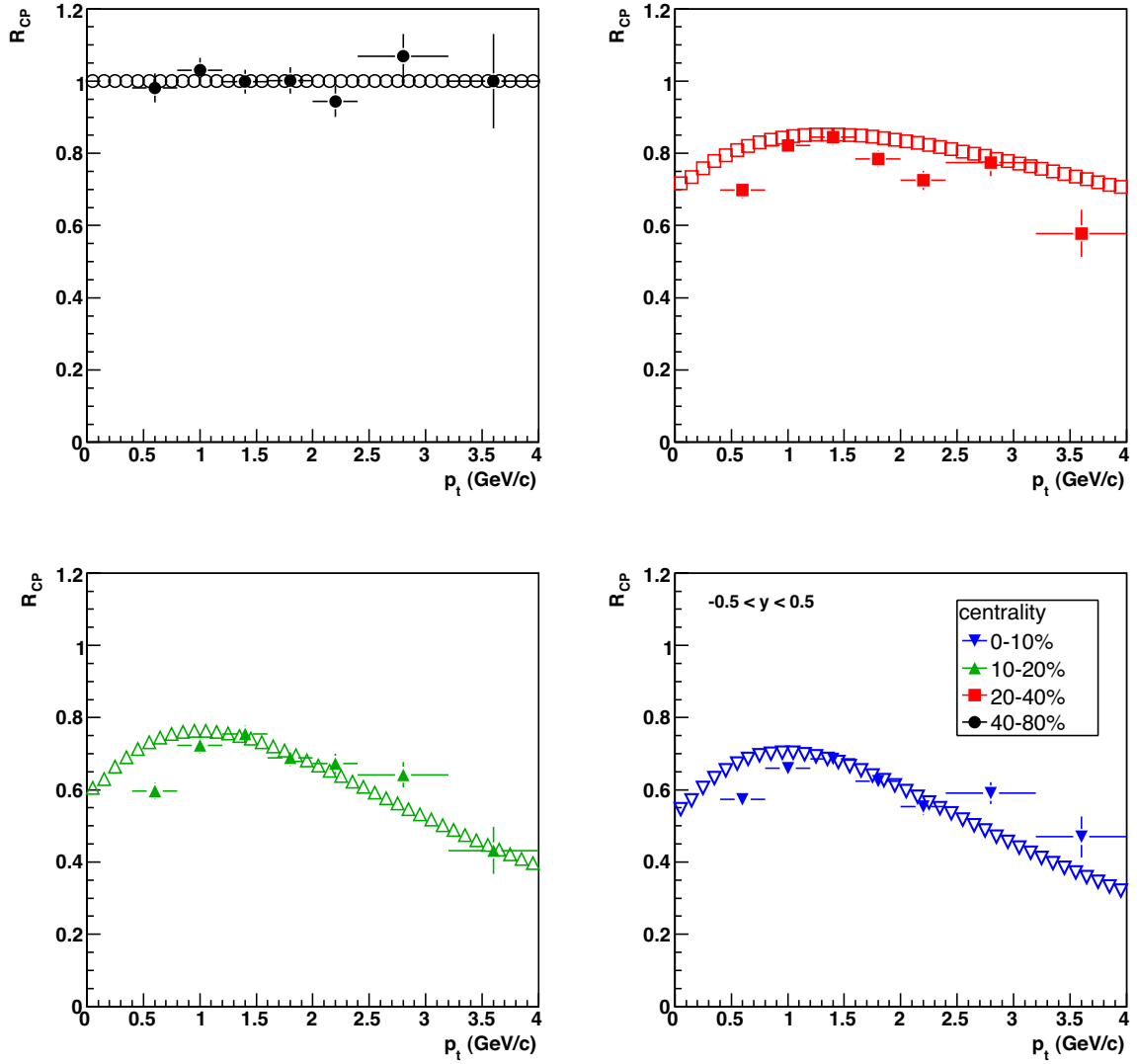


Figure 5.15: The comparison of the measured inclusive photon R_{CP} to the R_{CP} of photons from simulated π^0 -spectra are shown for four different centrality selections in minimum bias Au+Au-collisions at $\sqrt{s_{NN}} = 62$ GeV. The solid markers are the measured spectra and the open markers the ones from simulation.

In figure 5.5 the R_{CP} of inclusive photons is shown. The same quantity can be calculated for the simulated decay photon spectra from π^0 -mesons using the $\pi^+ - \pi^-$ -spectra as input. The resulting R_{CP} is shown shown for four centralities in figure 5.15. In contrast to the determination of the inclusive photon R_{CP} no fit of the peripheral bin was used for the simulated spectra. Rather the histograms for the four centralities were divided by the histogram in the most peripheral bin. Therefore the simulated R_{CP} in the peripheral

bin is by definition equal to one. A big advantage of this comparison is that some of the systematic uncertainties in each of the two measurements cancel by taking the ratio of central to peripheral spectra. Therefore this comparison is more accurate than the comparison of the spectra.

The plots for the two most central bins show that the magnitude of the suppression in the area above $0.8 \text{ GeV}/c$ transverse momentum is in agreement. In the $20 - 40\%$ centrality bin the measured photon spectra appear to be systematically lower than the simulated ones. Below $0.8 \text{ GeV}/c$ R_{CP} in the three central bins is systematically below the expected value from the simulation.

Above a transverse momentum $4 \text{ GeV}/c$ the contribution of direct photons relative to the decay photons is expected to increase. The suppression of the inclusive photon yield then should no longer be dominated by the meson suppression, but the not suppressed photons from initial hard scattering. Therefore the R_{CP} for the three central bins is expected to come gradually closer to one with rising transverse momentum starting at $4 \text{ GeV}/c$. However the statistical errors in figure 5.15 are too large to see any significant systematic deviations of the data from the simulation.

5.5 Photons from electro-magnetic hadron decays

The main contribution to the inclusive photon spectra in hadronic interactions comes from electro-magnetic decays of hadrons in the final state. The two main sources are the π^0 - and η -mesons. Contributions from other decays are below 4% as discussed in section 1.3.4. They are left out of this comparison, because this is much less than the systematic error on the inclusive photon spectra measured in this analysis. To get their contribution to the photon spectra, the decay of π^0 - and η -spectra, was simulated using GEANT. For the π^0 input distribution a power law fit to the STAR spectra of the charged π -mesons as discussed in section 5.4.3 was used. Because the statistical uncertainties on the $\pi^+\pi^-$ -spectra are much smaller than on the π^0 -spectra the fits are much better constrained. As there is no measurement of the η -spectra by STAR, the $\pi^+\pi^-$ -spectra were scaled using transverse-mass-scaling with an additional factor of 0.45. This has been motivated by a previous measurement of the η -spectra by the PHENIX-collaboration, which used the same scaling factor to determine the η -background in the photon spectra in Au+Au-collisions at $\sqrt{s_{\text{NN}}} = 200 \text{ GeV}$ [A⁺05].

The spectra of photons in minimum bias Au+Au collisions at $\sqrt{s_{\text{NN}}} = 62 \text{ GeV}$ are shown in figure 5.16 on the left side. The photons coming from π^0 - and η -decays are obtained from simulation (blue squares and green triangles). The measured inclusive photon spectrum is shown for comparison (red circles). The shape of the measured spectrum and the spectra from π^0 - and η -mesons look similar. To get a better comparison between the spectra one can plot the ratio of the measured photon spectra to the sum of the photon

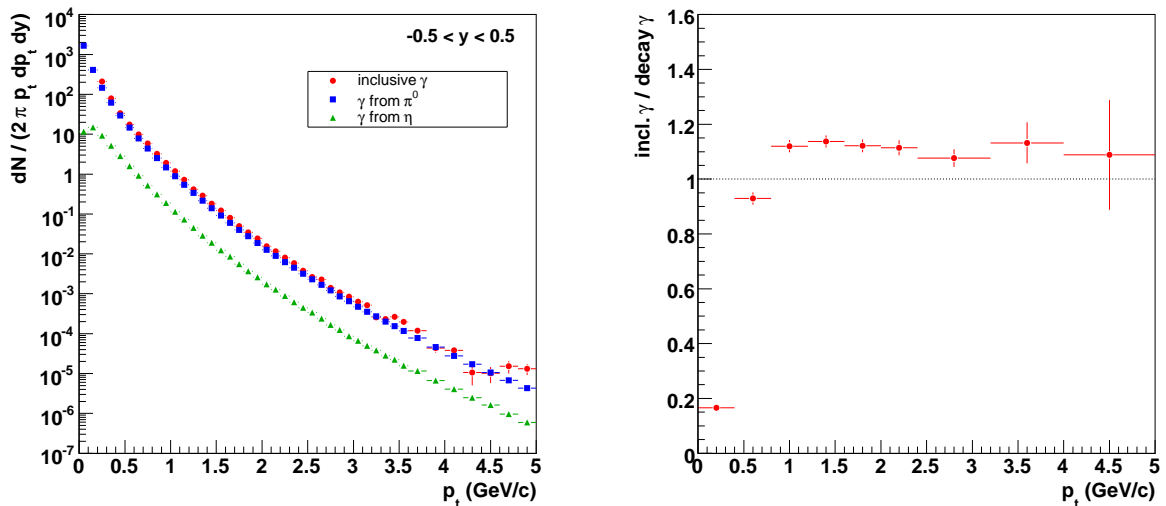


Figure 5.16: On the left the inclusive photon spectrum in minimum bias Au+Au-collisions at $\sqrt{s_{\text{NN}}} = 62 \text{ GeV}$ is compared to the expected contribution from π^0 - and η -decays. On the right the ratio of the same photons over the expected photon contribution from π^0 - and η -decays is shown. All errors are statistical only.

spectra from π^0 - and η -decays, which is shown in figure 5.16 on the right side. This ratio is between 1.1 and 1.2 and does not significantly depend on the transverse momentum above 1 GeV/c . The same ratio is shown for four different centralities in figure 5.17. None of them show a strong transverse momentum dependence above 1 GeV/c and all are on average close to 1.2.

5.5.1 Direct photons

The direct photon spectra are determined by subtracting the decay photon spectra from the inclusive photon spectra. In figures 5.16 and 5.17 the ratios of the inclusive to the decay photon spectra are shown. This ratio is up to about 1.2 at all centralities.

The size of the systematic errors discussed in section 4.6 is about 10% on the inclusive photon spectra due to the geometry correction and another 5% due to the embedding procedure. In addition uncertainties come from the $\pi^+\pi^-$ -spectra used as reference for the photonic contribution from π^0 - and η -decays, which themselves have an estimated uncertainty of similar size. They are explained in detail in section 5.4.3. The determination of the η -spectra however is even more difficult, because the relative ratio was assumed to be the same as in the Phenix measurement at $\sqrt{s_{\text{NN}}} = 200 \text{ GeV}$. So assum-

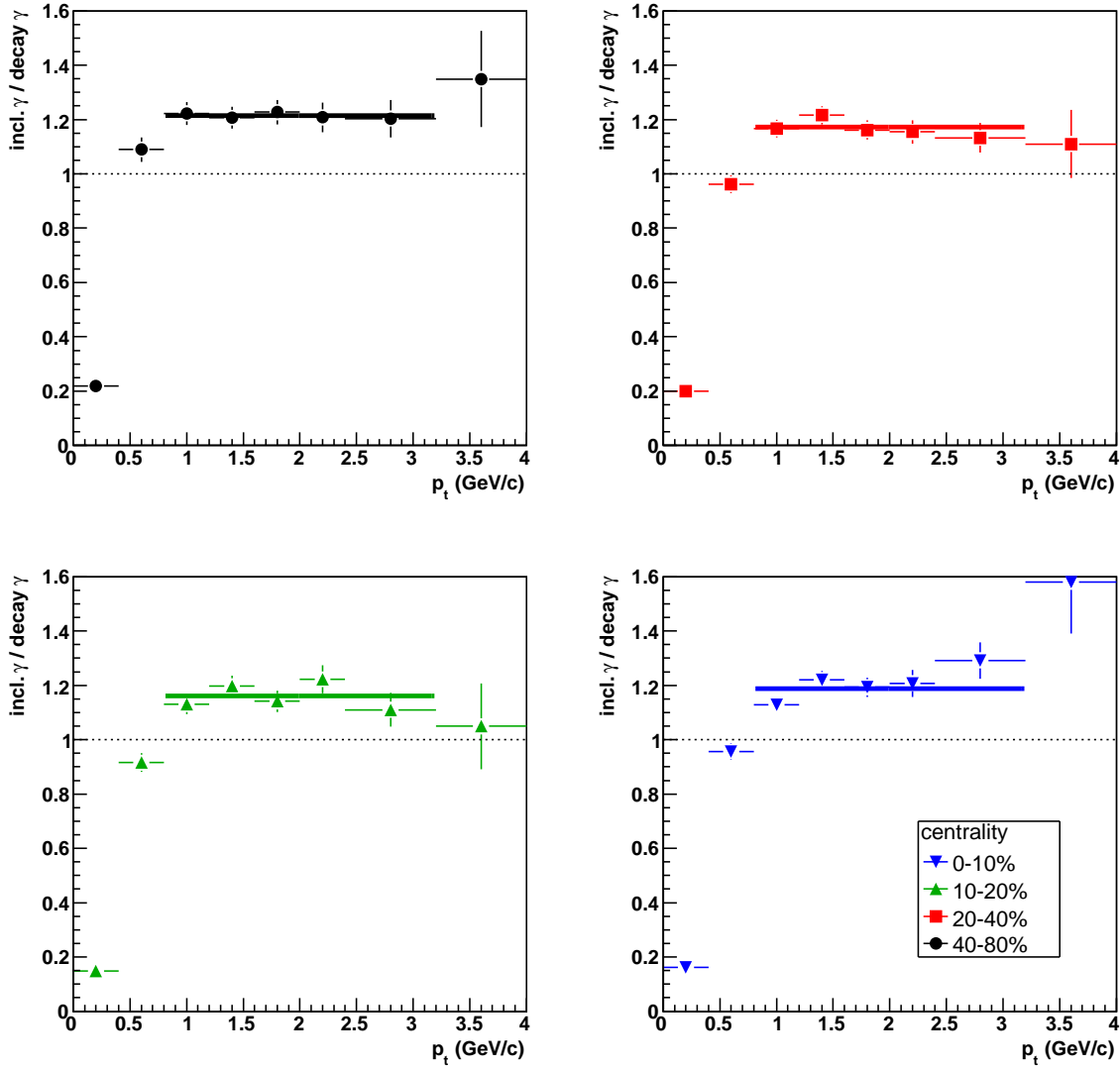


Figure 5.17: Ratio of the inclusive photon spectra to the photon contribution expected from π^0 - and η -decays for four different centralities. All errors are statistical only.

ing a 20% error on those spectra relative to the $\pi^+\pi^-$ -spectra results in an additional error of about 2% in the estimated photon spectra from π^0 and η .

Taking into account these errors, the observed ratio is not significantly different from 1, which corresponds to the observation of no direct photons. Also the missing clear centrality dependence suggests that the ratio does not necessarily point to direct photons. Because of the importance of the systematic uncertainties of all spectra they are

summarized in the next section.

5.6 Summary of all systematic uncertainties

photons		
	geometry description	10%
	embedding procedure from cut studies	5%
π^0 -mesons		
	geometry description	20%
	embedding procedure from cut studies	10%
	yield extraction from inv. mass histograms	10%
additional for direct photon determination		
π^+/π^- -reference		
	below $p_t = 1.6 \text{ GeV}/c$	8%
	normalization	10%
	above $p_t = 1.6 \text{ GeV}/c$ additional	5 – 10%
conversion of π^+/π^- - to photon spectra		
	if m_t scaling uncert. 20%	2%

Table 5.2: Estimated systematic uncertainties for photons and π^0 -mesons. Also given are the uncertainties concerning the determination of the direct photons.

The photon- and π^0 -spectra presented in this chapter are subject to different systematic uncertainties. The largest single contribution comes from the uncertainty of the geometry description, which is discussed in section 4.2. A second source is the remaining uncertainty in the embedding procedure, which was studied by varying the cuts as shown in section 4.6. For the π^0 -spectra there is an additional uncertainty coming from the way the π^0 -yield is extracted from the invariant mass histograms. This is explained in 3.5.

For photon- and π^0 -spectra the systematic uncertainties arising from the uncertainty in the geometry description have been discussed in detail in section 4.2 and for the other uncertainties due to the embedding procedure in section 4.6. They are listed in table 5.2. Because the $\pi^+\pi^-$ -spectra are used to estimate the direct photon yield, their errors, which are discussed in section 5.4.3 are included in the table as well.

6 Conclusion

In this chapter the results of this thesis will be summarized, including the implications for future photon measurements at STAR using photon conversions. This includes a few suggestions on how to improve the capabilities to measure direct photon spectra.

6.1 Inclusive photons and π^0 -mesons

The inclusive photon spectra in Au+Au-collisions at an energy of $\sqrt{s_{\text{NN}}} = 62 \text{ GeV}$ have been measured for four different centralities. The estimated systematic uncertainty of the results is 10% due to the geometry correction and below $4 \text{ GeV}/c$ transverse momentum additional 5% due to the embedding procedure. The rapidity dependence was measured above $0.3 \text{ GeV}/c$ transverse momentum and appears to be flat within one unit of rapidity around mid-rapidity.

The centrality dependence as measured in the central-to-peripheral-ratio R_{CP} has been compared to what would be expected from the R_{CP} of π^0 -mesons and is in agreement within the errors at low transverse momentum, where the photon spectra are dominated by decay photons from π^0 -mesons.

π^0 -spectra have been determined by using two-photon invariant mass spectra for four different centrality bins. The systematic errors are estimated to be 20% due to the geometry correction, in addition 10% due to the embedding procedure and 10% due to the yield extraction from the invariant mass histograms. The measurement is mainly limited by statistical errors due to the low photon detection efficiency using photon conversions in the detector material. The spectra have been compared to preliminary $\pi^+\pi^-$ -spectra measured in the same data set using the STAR time projection chamber and time of flight detectors and are in good agreement within systematic errors.

6.2 Direct photons

In an attempt to determine the contribution of direct photon to the inclusive photon spectra the latter was compared to the spectra expected from π^0 - and η -decays. Due to the large uncertainties on the π^0 -spectra the charged π -meson spectra were used instead of the π^0 -spectra as input to the simulation. The η -spectra were assumed to be consistent with m_t -scaling the π -spectra.

The ratio of the inclusive photon spectra to the expected background from meson decays is about 1.2 for all four centralities for transverse momenta between 1 and $3 \text{ GeV}/c$. The systematic uncertainties on the inclusive photon spectra are 10% plus 5% and there are additional uncertainties on determining the background from meson decays. Therefore the measured ratio is consistent with 1 and it is not possible to extract direct photon

spectra.

The result of this thesis is the basis for a proposal how to measure direct photons with STAR in the transverse momentum range between 1 and 3 GeV/ c . The next section discusses how the limitations due to systematic and statistical errors could be avoided.

6.3 Outlook

The measurements of inclusive photon spectra presented in this thesis have systematic errors, which are larger than the expected excess of the inclusive photons over the decay photon background. When looking at the direct photon measurements at full RHIC energy and top SPS energies the direct photon contribution at $\sqrt{s_{NN}} = 62$ GeV is expected to be between 10 and 20%. In addition to the systematic uncertainty on the photon spectra of 10% plus 5% the estimate of the background from π^0 - and η -decays has a systematic error of similar size. To observe direct photon yields, both systematic uncertainties have to be significantly reduced.

The largest contribution to the systematic errors comes from the inaccuracy of the geometry description used in Monte Carlo simulations to estimate the conversion probability of photons traversing the detector. About 30% of the real radiation length are missing in the simulation geometry, which has been corrected for, but a detailed description of which material is missing in exactly which places would do a better job and result in smaller uncertainties.

The second big problem for the direct photon spectra is the contribution by photons from π^0 - and η -decays. The main limiting factor in this analysis is next to the geometry description the statistical limitation in the π^0 -measurement. For this analysis $\pi^+\pi^-$ -spectra were used in their place. These, however, have different systematic uncertainties.

A data set of Au+Au-collisions at an energy of $\sqrt{s_{NN}} = 200$ GeV was taken before the data set at $\sqrt{s_{NN}} = 62$ GeV. Because RHIC run 4 has been mainly focused on this data set, it has a significantly larger statistics than the data set at the lower energy. Opposed to the data set at $\sqrt{s_{NN}} = 62$ GeV, for which mainly minimum bias events were triggered on, a more versatile trigger setup was used for the full energy data, to take enriched samples of central heavy ion collisions and events satisfying more elaborate trigger conditions. In addition the transverse momentum dependence of π^0 -spectra is flatter at the higher energy, which increases the number of π^0 -mesons at high transverse momenta. However, due to the higher multiplicity at higher energies, the combinatorial background increases and so do the errors.

Figure 6.1 illustrates the gain possible with this data set: For both data sets raw π^0 -spectra without efficiency corrections have been extracted. Shown is the size of the

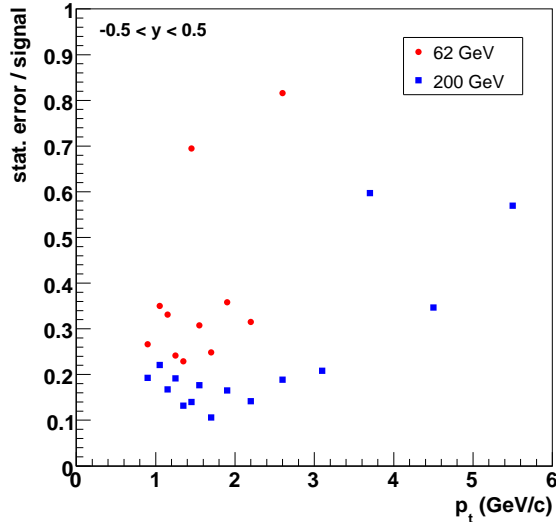


Figure 6.1: The size of the statistical error divided by the signal size is shown after extraction of the uncorrected π^0 -spectra from the central data set at $\sqrt{s_{NN}} = 62 \text{ GeV}$ (red circles) and $\sqrt{s_{NN}} = 200 \text{ GeV}$ (blue squares).

statistical errors given by the fits to the invariant mass peak divided by the size of the signal. For the data at $\sqrt{s_{NN}} = 62 \text{ GeV}$ (red circles) the centrality bin containing the 10% most central 793,977 events after cuts were used. At full energy 4,614,947 events after cuts were taken from the central triggered data set. The centrality in both data set is slightly different, because the centrality bin definition uses the reference multiplicity in the TPC, a number only calculated in the offline event reconstruction, while the central trigger uses the signal in the CTB. However this is a negligible effect for this comparison. It should also be noted, that for the central data set at full energy over 27 million events were recorded. For this comparison only a fraction of them were included. With the present statistics the errors decrease compared to the $\sqrt{s_{NN}} = 62 \text{ GeV}$ data set by up to a factor of 2 below $2.6 \text{ GeV}/c$ transverse momentum. Above, the statistical error for the low energy data set gets larger than the signal, while for the full energy data set the error is finite up to the highest transverse momentum bin.

While the data set at full energy will help to reduce the statistical errors significantly, additional efforts are necessary to reduce the size of the systematic errors on the measurements of photons and π^0 -mesons. Without substantial improvements it won't be possible to measure the photon spectra with an accuracy much better than 10%, which would be necessary to get a useful measurement of direct photon spectra, which are expected to be only about 10% of the inclusive photons.

Another way to tackle the uncertainties in the radiation length of the detector material

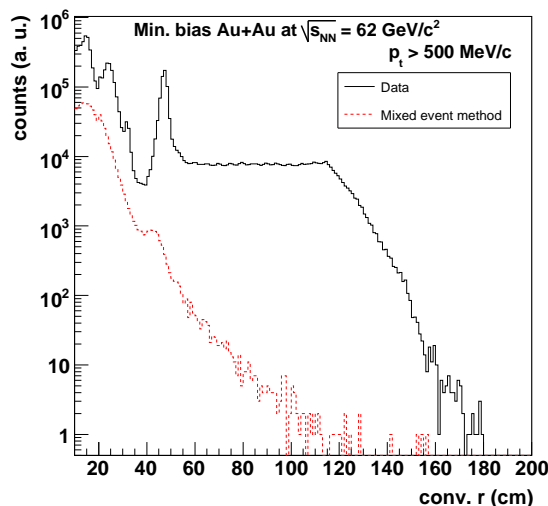


Figure 6.2: Number of conversions versus the radius for real data (black solid line) and mixed events (red dotted line) in minimum bias Au+Au-collisions at $\sqrt{s_{\text{NN}}} = 62 \text{ GeV}$.

on the trajectories of the particles is to add a dedicated converter to the experimental setup. Because a solid piece of material has a much simpler geometry than detectors like the SVT and SSD, an accurate description in the simulation is much more simple. Such a converter should have a radiation length of about 10%, cover the full azimuth and ± 1 units of pseudo-rapidity to get a similar number of conversions as in the SVT and SSD combined.

Looking at figure 6.2 showing the number of conversions versus the radial coordinate r , it is obvious that at the radius below 35 cm the combinatorial background contributes significantly to signal as well as the conversions from the not perfectly known SVT and SSD. If the converter is placed at or above 40 cm radius and still inside the inner field cage, photon conversion could be reconstructed with very little combinatorial background. The origin of conversions could be nicely resolved between SVT and SSD and the converter. Conversions from the inner field cage would not be distinguishable, but its geometry is better known than for the SVT and SSD and the overall radiation length is much smaller than 10%. This results in a much lower uncertainty due to material.

In addition a converter with 10% of a radiation length made from a heavy metal like lead or tungsten could be less than 1 mm thick. This essentially constrains the majority of conversions to a fixed radius, thus eliminating the dependence of the acceptance on the radius of the conversion point. Also, for a track originating from a conversion radius close to the inner field cage, the acceptance reaches to lower transverse momentum than it does for a track originating from the SVT or SSD.

A data set of Au+Au-collisions as taken at the energy of $\sqrt{s_{\text{NN}}} = 62 \text{ GeV}$ would yield similar statistical errors as shown on the photon and π^0 spectra in this thesis but would allow to significantly reduce the systematic uncertainties. If a thicker converter is chosen, the number of detected photons increases roughly linear with the thickness and the number of π^0 -mesons with the square. However this is paid for with a decreasing momentum resolution. Because a high momentum resolution is important for many analyses performed on STAR data, a dedicated run would be necessary to use the converter.

With significant improvement on the systematic uncertainties in the photon and π^0 -measurement, it will be possible to measure direct photon spectra with STAR in the transverse momentum range up to $3 \text{ GeV}/c$, where the photon spectra at RHIC presumably are dominated by thermal production. If the data set is large enough π^0 -spectra from the same method can be used as a basis to calculate the decay photon spectra. Otherwise a separate source of input like the $\pi^+\pi^-$ -spectra has to be used in their place. However, the current accuracy of these spectra is not sufficient for this task.

Bibliography

- [A⁺00] M. M. Aggarwal et al. Direct photon production in 158-A-GeV Pb-208 + Pb-208 collisions. 2000.
- [A⁺02] K. Adcox et al. Suppression of hadrons with large transverse momentum in central Au + Au collisions at $\sqrt{s_{NN}} = 130$ GeV. *Phys. Rev. Lett.*, 88:022301, 2002.
- [A⁺03a] K. H. Ackermann et al. The forward time projection chamber (FTPC) in STAR. *Nucl. Instrum. Meth.*, A499:713–719, 2003.
- [A⁺03b] K. H. Ackermann et al. STAR detector overview. *Nucl. Instrum. Meth.*, A499:624–632, 2003.
- [A⁺03c] M. Adamczyk et al. The BRAHMS experiment at RHIC. *Nucl. Instrum. Meth.*, A499:437–468, 2003.
- [A⁺03d] J. Adams et al. Evidence from d + Au measurements for final-state suppression of high p_T hadrons in au + au collisions at rhic. *Phys. Rev. Lett.*, 91:072304, 2003.
- [A⁺03e] J. Adams et al. Transverse momentum and collision energy dependence of high p(t) hadron suppression in Au + Au collisions at ultrarelativistic energies. *Phys. Rev. Lett.*, 91:172302, 2003.
- [A⁺03f] K. Adcox et al. PHENIX detector overview. *Nucl. Instrum. Meth.*, A499:469–479, 2003.
- [A⁺03g] C. Adler et al. Azimuthal anisotropy and correlations in the hard scattering regime at RHIC. *Phys. Rev. Lett.*, 90:032301, 2003.
- [A⁺03h] S. S. Adler et al. Absence of suppression in particle production at large transverse momentum in $\sqrt{s_{NN}} = 200$ -GeV d + Au collisions. *Phys. Rev. Lett.*, 91:072303, 2003.
- [A⁺03i] M. M. Aggarwal et al. The STAR photon multiplicity detector. *Nucl. Instrum. Meth.*, A499:751–761, 2003.
- [A⁺03j] C. E. Allgower et al. The STAR endcap electromagnetic calorimeter. *Nucl. Instrum. Meth.*, A499:740–750, 2003.

- [A⁺03k] M. Anderson et al. The STAR time projection chamber: A unique tool for studying high multiplicity events at RHIC. *Nucl. Instrum. Meth.*, A499:659–678, 2003.
- [A⁺03l] L. Arnold et al. The STAR silicon strip detector (SSD). *Nucl. Instrum. Meth.*, A499:652–658, 2003.
- [A⁺04] J. Adams et al. Photon and neutral pion production in au + au collisions at $\sqrt{s_{NN}} = 130$ GeV. 2004.
- [A⁺05] S. S. Adler et al. Centrality dependence of direct photon production in $\sqrt{s_{NN}} = 200$ GeV Au + Au collisions. *Phys. Rev. Lett.*, 94:232301, 2005.
- [AMY01] Peter Arnold, Guy D. Moore, and Laurence G. Yaffe. Photon emission from quark gluon plasma: Complete leading order results. *JHEP*, 12:009, 2001.
- [ARW98] Mark G. Alford, Krishna Rajagopal, and Frank Wilczek. Qcd at finite baryon density: Nucleon droplets and color superconductivity. *Phys. Lett.*, B422:247–256, 1998.
- [B⁺03a] B. B. Back et al. The PHOBOS detector at RHIC. *Nucl. Instrum. Meth.*, A499:603–623, 2003.
- [B⁺03b] M. Beddo et al. The STAR barrel electromagnetic calorimeter. *Nucl. Instrum. Meth.*, A499:725–739, 2003.
- [B⁺03c] R. Bellwied et al. The STAR silicon vertex tracker: A large area silicon drift detector. *Nucl. Instrum. Meth.*, A499:640–651, 2003.
- [B⁺03d] F. Bergsma et al. The STAR detector magnet subsystem. *Nucl. Instrum. Meth.*, A499:633–639, 2003.
- [B⁺03e] F. S. Bieser et al. The STAR trigger. *Nucl. Instrum. Meth.*, A499:766–777, 2003.
- [Bat] Stefan Bathe. Centrality dependence of π^0 production in Au+Au collisions at $\sqrt{s_{NN}} = 62.4$ GeV. Talk given at the DNP Fall Meeting 2004 in Chicago.
- [Bat05] Stefan Bathe. Direct photons in 200-GeV p + p, d + Au, and Au + Au from PHENIX. 2005.
- [BSZ00] R. Baier, D. Schiff, and B. G. Zakharov. Energy loss in perturbative qcd. *Ann. Rev. Nucl. Part. Sci.*, 50:37–69, 2000.
- [CP75] N. Cabibbo and G. Parisi. Exponential hadronic spectrum and quark liberation. *Phys. Lett.*, B59:67, 1975.
- [FK02] Z. Fodor and S. D. Katz. Lattice determination of the critical point of qcd at finite t and mu. *JHEP*, 03:014, 2002.

- [FM04] R. J. Fries and B. Muller. Heavy ions at LHC: Theoretical issues. *Eur. Phys. J.*, C34:s279–s285, 2004.
- [FMS03] Rainer J. Fries, Berndt Muller, and Dinesh K. Srivastava. High energy photons from passage of jets through quark gluon plasma. *Phys. Rev. Lett.*, 90:132301, 2003.
- [GEA] *GEANT: Detector description and simulation tool*. <http://wwwasd.web.cern.ch/wwwasd/geant/>.
- [Gon06] Johan Gonzalez. Glauber calculations. private communication, 2006.
- [GST] *GSTAR: STAR detector simulation tool*. <http://www.star.bnl.gov/STAR/comp/simu/gstar/gstar.html>.
- [H⁺02] K. Hagiwara et al. Review of particle physics. *Phys. Rev.*, D66:010001, 2002.
- [H⁺03] H. Hahn et al. The RHIC design overview. *Nucl. Instrum. Meth.*, A499:245–263, 2003.
- [Hag04] Kevin Lee Haglin. Rate of photon production from hot hadronic matter. *J. Phys.*, G30:L27–L33, 2004.
- [HK85] R. C. Hwa and K. Kajantie. Diagnosing quark matter by measuring the total entropy and the photon or dilepton emission rates. *Phys. Rev.*, D32:1109, 1985.
- [HLO03] M. Harrison, T. Ludlam, and S. Ozaki. RHIC project overview. *Nucl. Instrum. Meth.*, A499:235–244, 2003.
- [Joh03] I. J. Johnson. Measurements of photon and π^0 production in heavy ion collisions at RHIC. *Nucl. Phys.*, A715:691–694, 2003.
- [KLP⁺] F. Karsch, E. Laermann, P. Petreczky, S. Stickan, and I. Wetzorke. QCD thermodynamics: The numerical study of strongly interacting matter under extreme conditions. Prepared for NIC Symposium 2001, Julich, Germany, 5-6 Dec 2001.
- [KLS91] Joseph I. Kapusta, P. Lichard, and D. Seibert. High-energy photons from quark - gluon plasma versus hot hadronic gas. *Phys. Rev.*, D44:2774–2788, 1991.
- [M⁺03] H. S. Matis et al. Integration and conventional systems at STAR. *Nucl. Instrum. Meth.*, A499:802–813, 2003.
- [Mil03] Michael L. Miller. *Measurement of jets and jet quenching at RHIC*. PhD thesis, Yale University, 2003. UMI-31-25263.

- [Moh06] Bedanga Mohanty. π^+ - and π^- -spectra from relativistic de/dx. private communication, 2006.
- [Owe87] J. F. Owens. Large momentum transfer production of direct photons, jets, and particles. *Rev. Mod. Phys.*, 59:465, 1987.
- [ROO] *ROOT: An object oriented data analysis framework*. <http://root.cern.ch>.
- [S+01] Torbjorn Sjostrand et al. High-energy-physics event generation with pythia 6.1. *Comput. Phys. Commun.*, 135:238–259, 2001.
- [Sat03] Helmut Satz. Limits of confinement: The first 15 years of ultra- relativistic heavy ion studies. *Nucl. Phys.*, A715:3–19, 2003.
- [Sha06] Ming Shao. π^+ - and π^- -spectra from time of flight. private communication, 2006.
- [SLM01] Torbjorn Sjostrand, Leif Lonnblad, and Stephen Mrenna. Pythia 6.2: Physics and manual. 2001.
- [TRG04] Simon Turbide, Ralf Rapp, and Charles Gale. Hadronic production of thermal photons. *Phys. Rev.*, C69:014903, 2004.
- [WHS96] Xin-Nian Wang, Zheng Huang, and Ina Sarcevic. Jet quenching in the opposite direction of a tagged photon in high-energy heavy-ion collisions. *Phys. Rev. Lett.*, 77:231–234, 1996.

Acknowledgments

Thanks to Herbert Ströbele who accepted me as a student for my research in heavy ion physics in his group in Frankfurt and supported my decision to go to Berkeley and STAR for doing my doctorate research.

I also want to thank Reinhardt Stock who encouraged me to go to Berkeley and join STAR and who made it possible by initiating the support from the Frankfurt group for those activities. I thank Hans-Georg Ritter for inviting me to join the Relativistic Nuclear Collisions group in Berkeley. He also generously helped out with any organizational difficulties encountered during my time at Lawrence Berkeley Lab.

Thanks to Peter Jacobs, who accepted me as his student to work on the measurements presented in this thesis. In our discussions he always encouraged me to go on with the analysis despite the problems encountered.

I also have to thank Jeniffer Klay and Kirill Filimonov for supervising my analysis for some time and providing useful advice. For the same reasons I have to thank Marco van Leeuwen, who also was always willing to help with questions of fundamental physics, analysis and computing problems. Besides work all of them proved to be good friends and we had a great time together.

Thanks to Art Poskanzer, who brought me in contact with the Nuclear Relativistic Collisions group at Lawrence Berkeley National Lab during the time when he supervised the analysis for my diploma thesis. But even afterwards during my analysis for this thesis I had many interesting conversations and learned a lot from him.

I would like to thank Ian Johnson, who used the same analysis technique for photon conversions in STAR as I uses for this thesis before and provided me with his code and an introduction to the analysis.

Thanks to Markus Oldenburg, Sarah Blyth, Katarzyna Kowalik, Mark Horner, Joern Putschke, Paul Sorensen, Kai Schweda, Fabrice Retiere, Johan Gonzalez, Javier Castillo, Lara Pierpoint, Heather Gray, Lijuan Ruan, Andrew Rose, Tom Gutierrez, Leo Greiner, Jim Thomas and all the other young members of the Berkeley RNC Group I forgot to mention, for the vivid discussions during the coffee breakes at 2 pm sharp. All of them turned out to be great friends and I had a very good time with them at work and at the many activities outside of physics, which made my time in Berkeley unforgettable.

Thanks also to all other members of the STAR collaboration. Without the fundamental work and infrastructure provided by all of them the analysis presented in this thesis would not have been possible.

Thanks to all members of the Frankfurt experimental heavy ion physics group, who were

available for the exchange of scientific ideas and provided a good working environment before and after I was in Berkeley.

Hannah Petersen and Marcus Bleicher are to be thanked for some insight into the secrets of the vast world of theoretical physics. We also spent a few great evenings together and had very interesting discussions on other topics besides physics.

Last but not least I want to thank my parents, my sister Antonia and my brothers Philipp and Claudius and other members of my family, whose continuous emotional support kept me going, when I was struggling with the analysis. Also they distracted me from time to time, when problems clouded my view.

Lebenslauf



Alexander Wetzler

Friedrich-Ebert-Straße 14
61462 Königstein im Taunus
geboren am 18. Dezember 1976 in Frankfurt am Main

Schulbildung

1983 – 1987 Grundschule
1987 – 1996 Gymnasium: Bischof-Neumann-Schule in Königstein im Taunus

Wehrdienst

1996 – 1997 Wehrdienst

Studium

seit 1997 Studium der Physik an der Johann Wolfgang Goethe-Universität
in Frankfurt am Main

5. 2001 – 4. 2002 Diplomarbeit bei Herrn Prof. Dr. Herbert Ströbele
am Experiment NA49 (CERN), mit dem Titel: Gerichteter
und elliptischer Fluss in Blei-Blei Sten bei einer Strahlenergie
von 40 GeV pro Nukleon

9. 2002 Diplom in Physik (Note: sehr gut)

10. 2002 Beginn des Promotionsstudiums
bei Herrn Prof. Dr. Herbert Ströbele

5. 2003 – 4. 2006 Forschungsaufenthalt am Lawrence Berkeley National
Laboratory, Berkeley, CA